Fabrication and Characterization of Nanostructured Magnetic Particles for Applications in Data Storage

by

Maya S. Farhoud

B.S. Electrical Engineering, University of Texas at Arlingtion (1995)
SM Electrical Engineering and Computer Science, MIT (1997)

Submitted to the Department of Electrical Engineering and Computer Science in partial fulfillment of the requirements for the degree of

PhD

at the

MASSACHUSETTS INSTITUTE OF TECHNOLOGY

June 2001

Signature of Author. . . . . .
Department of Electrical Engineering and Computer Science
December, 2000

Certified by . . . . . .
Henry I. Smith and Caroline A. Ross
Thesis Supervisors

Accepted by . . . . . .
Arthur C. Smith
Chair, Department Committee on Graduate Students

Acknowledgments

With great pleasure and enthusiasm, I take this opportunity to thank the folks who, either directly or indirectly, have enabled this Ph.D. thesis. First, I thank my advisors Prof. Hank Smith and Prof. Caroline Ross. I am grateful for the opportunity to work under your tutelage on this fascinating topic. Also, I thank you for believing in me and for giving me the freedom (and the support) to pursue my interests.

Second, I thank the very gifted staff of the Nanostructures Laboratory. Jimmy Daley, Jim Carter, Eddy Murphy, and Mark Mondol. I learned innumerable things from you guys. I'm also appreciative of the way in which you take care of us students.

Behind the scenes, I was often mentored by James Goodberlet, Juan Ferrera, and Tom Murphy. In addition to proof-reading several of my manuscripts and presentations, James, Juan, and Tom have been perpetual sources of inspiration and support for me. From them I have learned many a technical thing, as well as things about patience, kindness and perseverance.

During the course of my Ph.D., I've had the privilege of working closely with the students and staff in Prof. Ross' group. Mike Walsh, Doug Twisselmann, Minha Hwang, Yaowu Hao, Joy Cheng, Mutsuhiro Shima, and Fernando Castano. I want to thank you all so much for your friendship. It has meant a lot to me. I also thank you for sharing your knowledge and talent. You made learning about interference lithography and magnetism that much more enjoyable.

My interaction with the students at the Nanostructures Laboratory has been very valuable to my education as well. In recent years, I've engaged in useful conversation with Rajesh Menon, Todd Hastings, Mark Finlayson and David Carter. I wish you all much success in your future endeavors. Special thanks to Euclid Moon who has been a kind friend since the beginning. I'd like to recognize the efforts of Cindy Lewis at keeping our group organized.

A third MIT laboratory that has played an important part in enabling the work of this thesis is the Space Nanostructures Laboratory (SNL). I'd like the thank Mark Schattenburg, Bob Fleming, and Jane Prentiss for teaching me a lot, and allowing me to be a friend of the SNL.

Outside my research groups, I've had the pleasure of interacting with and learning from Tony Lochtefeld, Farhan Rana, Mathew Abraham, and Dave Pflug. Jim Fiorenza and Samuel Mertens taught me a great deal about silicon devices.

I was an IBM Fellowship recipient for two years of my doctoral work. At IBM, I thank in particular my sponsors Manfred Schabes and Hal Rosen for this great honor as well as for hosting my visit to the Almaden Research Center in Sept. 1999.

I thank the members of my committee Prof. Ross and Smith as well Prof. Markus Zahn and Dr. Bob O'handley for all of their useful comments regarding this thesis and my work in general.

In the department of electrical engineering, I'm grateful to Marilyn Pierce, as well as Profs. Al Drake and Terry Orlando for their guidance.

On a personal level, I'd like to thank my friends and roommates for their encouraging words and for supplementing my academic education. I thank Markus Peuker for reading this thesis and providing useful comments.

Finally, I'm thankful for being a member of a very loving clan: my mom and dad, my two sisters, my aunts and uncles and grandparents and my husband-to-be.

Fabrication and Characterization of Nanostructured Magnetic Particles for Applications in Data Storage

by

Maya Farhoud

Submitted to the Department of Electrical Engineering and Computer Science
on December 12, 2000, in partial fulfillment of the
requirements for the degree of
Doctor of Philosophy

Abstract

Arrays of nanostructured magnetic particles ('nanomagnets') have potential applications in ultra-high-density data storage devices and dynamic magnetic memories, and are model systems for the study of magnetic phenomena at deep sub-micron length scales. We use interference lithography to pattern 200 nm-period arrays of nickel and cobalt nanomagnets. The nickel and cobalt are deposited via electroplating or evaporation/lift-off processes. Magnetometry techniques are used to characterize the bulk magnetic behavior of the arrays. Magnetic force microscopy is used to image the stray magnetic fields of individual nanomagnets as well as to measure particle switching fields. We compare our experimental results to predictions based on micromagnetic models and models of magnetostatic interactions. In particular, the influence of shape, size, inter-particle spacing and material properties on the remanence state of nanomagnets is evaluated. Finally, we examine the suitability of the fabricated nanomagnet arrays for applications in magnetic data storage.

TABLE OF CONTENTS

CHAPTER 1: INTRODUCTION

1.1 Background: Storage Gluttons

The information age has driven an apparently insatiable need for higher density, lower cost data storage devices. The onslaught of portable electronics (cell phones, personal digital assistants, digital music players, digital cameras, camcorders) is witness to the individual's growing need to store more data. The internet's move to center stage in today’s economy makes data storage and manipulation of vital importance to almost all business sectors [1].

The hard disk which stores information in magnetic patterns remains the cheapest and most versatile data storage technology. Today, we can purchase a Megabyte in a hard disk for less than $0.07. Hard disk storage costs ten times less than flash memory, a competing technology in the sector of portable electronics [2]. The price of hard disks has been decreasing at a rate of 40% per year, encouraged by the fluidity of the storage market. Each 1% decrease in price is accompanied by a 4% increase in demand [1].

Improvements in data density of hard disks has been the key enabler of the decline in hard disk prices. Today's state-of-the-art data density, however, can no longer be improved without bound. The areal density, or number of bits per unit area, of hard disk is limited by thermal noise, or the "superparamagnetic limit" on the size of data bits. As expected, this limit has been cause for great concern in the data storage community. Many research groups, both in industry and academia, have dedicated themselves to forestalling the advent of superparamagnetism [2-6].

The investigation reported in this thesis is inspired in part by superparamagnetism. In particular, this thesis explores opportunities for nanofabrication and nanostructures in magnetic data storage. Nanostructured magnetic elements ('nanomagnets') may extend the lifetime of areal density beyond the projected limit [2]. Furthermore, nanomagnets are also building blocks for on-chip type storage elements such as magnetic random access memory (MRAM) [7].

In this thesis, we discuss the characteristics of a nanostructured, patterned medium suitable for magnetic data storage. We fabricate and characterize arrays of nanomagnets for applications in data storage.

1.1.1 History of the Hard Disk

It is quite wonderful to ponder the existence and impact of magnetic storage in our daily lives. Everywhere, there are hidden magnets that store data: videotapes, audiotapes, credit and ATM cards, key cards, hard disks, floppy disks and removable media such as Zip®, Jaz® etc.

The first known demonstration of magnetic data storage is the invention of the telegraphone by Danish engineer Valdemar Poulsen in 1898 [8]. The first hard disk, the RAMAC, was built by IBM in 1956. It boasted an areal density of 2000 bits/in^2 and a total capacity of 5 Mbytes stored on 50, 24" platters. The highest areal density drive available on the market today can store 17 Gbits/in^2, representing an 8.5 million times increase in 44 years.

Since 1991, the areal density of hard disks has increased at a rate of 60% per year and since 1997, has doubled every year. This trend is the by-product of more sensitive read heads based on magneto-resistance phenomena [2]. Researchers at IBM, the leader in hard disk manufacturing, predict the superparamagnetic limit will halt the growth of areal density at about 100 Gbits/in^2. To understand the origin of this limit, we examine the storage medium in a conventional hard disk.

1.2 Motivation: Storage in Trouble

1.2.1 How do Hard Disks Store Data?

Hard disks consist of a non-magnetic, spinning substrate coated with a thin (10-20 nm) layer of sputtered magnetic alloy (Fig. 1.1). The alloy grains have an average size of 10-15 nm with in-plane easy axes (i.e. $\overline{M}$ lies in plane). Data is recorded by magnetizing small, adjacent patches of grains. Read-back is achieved by sensing the fringing field between two oppositely magnetized, neighboring patches of grains. In such a scheme, the signal-to-noise ratio (S/N) is proportional to the square root of the number of grains in each patch. A patch of 1000 grains (S/N=32) is considered compatible with state-of-the-art read heads. Thus, increasing disk areal density requires decreasing grain size while maintaining the number of grains per bit.

Researchers at IBM and other hard disk manufacturers have been able to squeeze more bits into a unit area by decreasing the size of grains comprising the bits. The superparamagnetic limit on grain size is the much feared potential show-stopper to this evolutionary growth in areal density. Each grain is a magnetically bi-stable single domain. The energy barrier between a grain's two stable states is given by KV, where K is the magnetic anisotropy energy density of the grain and V is the grain volume (Figure 1.2). As grain size decreases, thermal energy, k_BT, becomes a significant fraction of the energy barrier between a grain's two stable

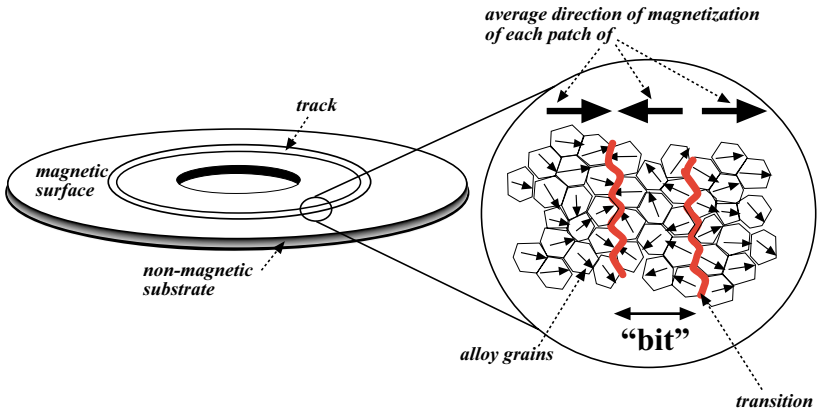

Figure 1.1 Schematic of a hard disk inside a computer hard drive. A non-magnetic substrate with a hole in the center is coated with a thin layer of sputtered Co-Cr-Pt alloy. As the disk spins at high speed, a read/write head (not shown) magnetizes patches of film grains along concentric tracks of the disk. Data is encoded by the presence or absence of transitions in the direction of magnetization (inset).

states. The superparamagnetic effect is the random, thermally-activated switching experienced by small grains.

A grain's average magnetic reversal time (in seconds) is given by:

$$\tau^{-1} = f_0 e^{\frac{-KV}{k_B T}} \tag{1.1}$$

where f_0 is a frequency factor equal to 10^9 s^{-1}. Random, thermally-induced fluctuation of magnetization is evidence of paramagnetic behavior. Paramagnetism is observed in single-domain, ferromagnetic grains whenever the energy barrier between their two stable states is approximately $25 \cdot k_B T$ [9]. The term superparamagnetic is used to distinguish this size induced effect from a true paramagnet in which such behavior is observed at any volume. For thermal stability in hard disk media, $KV/k_B T$ should exceed 60 since the demagnetization field in the vicinity of stored transitions (Fig. 1.1) hastens the onset of superparamagnetism [9]. Since the current grain diameters leave little opportunity to decrease grain volume, the anisotropy constant K must be increased. Very large values of K, however, render the data more difficult to write [10]. The maximum field that a writing head can produce is about 5000 Oe (400 kA/m) [9].

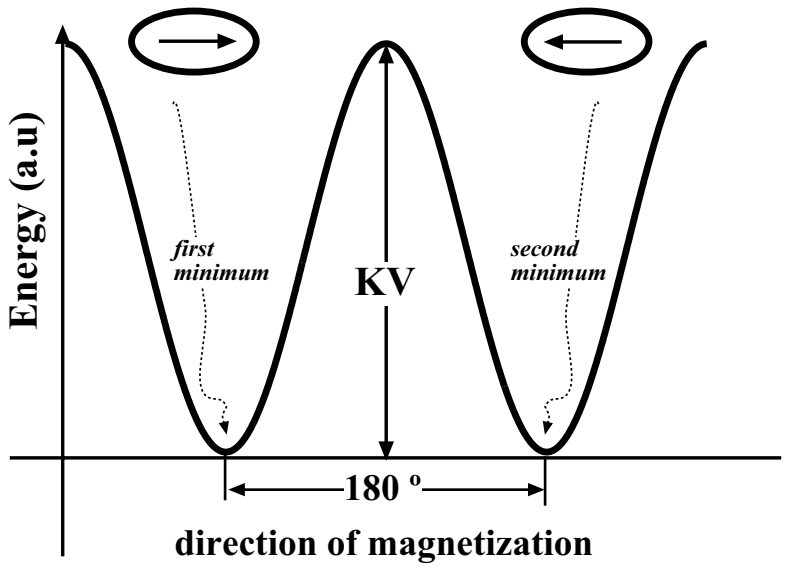

Figure 1.2 The energy barrier, in zero applied-field, between the two stable states of a single-domain particle. The arrow inside the ellipsoid represents the magnetization inside an ellipsoidal particle, where the long direction is the easy axis of magnetization.

1.3 Goals: What Nanostructures can do for Magnetic Data Storage

1.3.1 Cheating the Superparamagnetic Limit

In 1994, researchers at Stanford and the University of Minnesota suggested replacing thin films in hard disks with lithographically patterned media, consisting of physically discrete, single-domain, nanostructured magnetic particles (nanomagnets) [11,12]. Data storage based on patterned media is illustrated schematically in Fig. 1.3. Ideally, in a patterned data storage medium, media noise is non-existent since the boundaries of a bit are well defined, thus the strict requirement on the number of grains per bit is relaxed [13]. Potentially, each particle could be as small as a single grain, provided: a) the grain is large enough to be thermally stable; b) particle signal is strong enough to detect; and c) the space between neighboring particles results in weak magnetostatic interactions. By designing discrete media such that the easy axis of the particles is perpendicular to the substrate, we can increase areal density further [2].

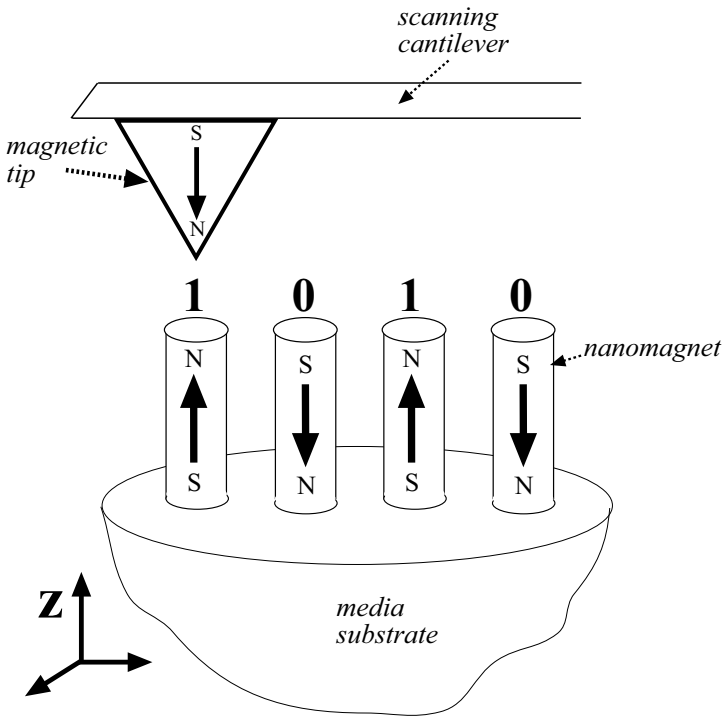

Figure 1.3 Example of data storage in an array of perpendicular, single-domain nanomagnets. A nanomagnet oriented into the substrate could represent a binary “0” while a nanomagnet pointing out of the substrate could represent a binary “1”, or vice-versa. A scanning probe with a magnetic tip may be used to read and write this media.

1.3.2 Our Contribution

Producing patterned media poses a fabrication challenge since it requires generating sub-100 nm magnetic structures of controlled geometry and spatially-coherent arrangement over large areas of a substrate. In addition, the magnetic properties and behavior of nanosized magnetic particles remain a partially explored area of science [14,15]. Research groups investigating lithographically-patterned media have focused either on developing practical fabrication schemes [16], or on the characterization of structures that have very specific characteristics and manufactured via prohibitively slow and expensive means [5,17-19]. Furthermore, the literature is rich with theoretical studies of highly idealized nanomagnets [20-29] with little comparison to experimental data from real structures.

The goal of this work is to perform a comprehensive study of arrays of nanomagnets. In particular:

(1) We identify a versatile nanolithography technology that enables the practical manufacture of these arrays over large areas. Also, we explore a variety of fabrication processes that yield nanomagnets of different sizes, shapes, and material compositions.

(2) We perform detailed studies of the influence of the physical parameters of particles and arrays on magnetic behavior. We measure the bulk properties, or collective behavior, of the arrays using magnetometry, as well as the individual behavior of each nanomagnet in the array using magnetic-force microscopy (MFM).

(3) We relate the experimentally observed behavior to micromagnetic models, and models of magnetostatic interactions between particles in an array. As part of this effort, our research group, in collaboration with a group at Boston University, has developed micromagnetic models that simulate the remanent states of individual particles [30]. Since fabrication and modeling are carried out in parallel, we gain fundamental knowledge of the following characteristics of nanomagnets:

a. the magnetization configuration in the absence of an applied field (remanent state) of the particles, as well as of magnetization easy axis.

b. anisotropy and switching fields

c. magnetostatic interactions of the particles in an array

d. superparamagnetic behavior of individual particles

e. uniformity within an array

(4) We assess the suitability of the various fabrication approaches to specific applications such as patterned media and MRAMs. In this thesis, we focus on patterned media in particular. The investigation of MRAMs is an on-going effort in our group [7,31].

1.3.3 Characteristics of Patterned Media

We have identified the following criteria for an array of nanomagnets to be suitable for data storage. In this thesis, we examine all fabricated arrays in light of these criteria.

Individually, the nanomagnets must be small enough such that the formation of domain walls within a particle is energetically unfavorable in the absence of an applied field. However, their size must not decrease below the superparamagnetic limit. In addition, the nanomagnets must have a uniaxial magnetic anisotropy perpendicular to the substrate. The major contributors to a nanomagnet's total anisotropy K are its shape anisotropy, K_s, and its magnetocrystalline anisotropy, K_m. K_s tends to align the magnetic moment of a particle with a long axis. K_m aligns the particle's moment with one or more of the crystalline axes that favor easy magnetization. In addition, the field required to reverse the magnetization of a single particle, H_{sw}, must be controllable. Similarly, a particle's magnetization, M, must be strong enough to detect with a magnetic sensor. Collectively, the particles should exhibit weak magnetostatic interactions. In particular, the field experienced by any one particle due to all the other particles in the array, H_{int_total}, may not exceed the switching field of the particle in question; otherwise, the particles can be switched by the magnetostatic field from their neighbors which would make the array unsuitable for storage.

1.4 Contents

Chapter 2 of this thesis presents all magnetic theory pertaining to the design and understanding of nanostructured magnetic particles. Nanomagnets are classified according to their magnetic configuration into three regimes: multiple-domains, particles with no domain walls but with $\nabla\cdot\overline{M}\neq 0$, and single-domain particles with $\nabla\cdot\overline{M}=0$. All energy terms within a nanomagnet are presented along with models for magnetization reversal. In Chapter 3, we identify interference lithography (IL) as a versatile candidate for the manufacture of large-area arrays of nanomagnets. IL has the necessary resolution and can generate patterns in fast exposure times. We also develop several fabrication techniques; each is suitable for producing nanomagnets with specific physical characteristics. In particular, nanomagnets are fabricated via additive processes such as evaporation and electroplating, and subtractive processes such as etching of magnetic thin films. Chapter 4 is divided into two parts. In the first part, we perform bulk magnetic characterization of the samples we have fabricated. This entails generating a hysteresis loop for the samples in two directions, parallel and perpendicular to the substrate. Also, we perform experiments that image the stray field of individual nanomagnets. These experiments are done via magnetic force microscopy (MFM), a relatively new form of scanning-probe microscopy. Most published MFM work on nanostructured magnetic particles is qualitative in nature [32-34]. Dipole like fields are observed whenever a single-domain particle is imaged [32]. We develop techniques that yield more quantitative information, such as an upper and lower bound on the switching fields of the nanomagnets. Finally, we assess the suitability of all samples for data storage by measuring their performance against the criteria listed in section 1.3.3.

1.5 Units

Though fascinating in all other respects, the study of practical magnetism proves an enigma of sorts concerning the use of units. It is a fact that the recording industry deals primarily in cgs units. Likewise, this unit system is pervasive throughout the literature. Furthermore, laboratory instruments that measure magnetic fields often report only cgs units. The continued

use of this unit system is justifiable in light of the large and cumbersome numbers produced when measuring magnetic fields in MKS.

In this thesis, I report all equations in MKS units. However, for consistency with our publications (Appendix A), data is presented as it was acquired, in cgs units. Table 1.1 contains conversion factors between cgs and MKS to aid the reader, in case there is ambiguity.

Units and Conversions		
Quantity	**MKS**	**cgs**
Energy (E)	1 J	10^7 ergs
Flux (ϕ)	1 weber	10^8 maxwells
Magnetic flux density (B)	1 T	10^4 gauss
Magnetic field (H)	1 A/m	$4\pi/10^3$ Oe
Magnetic moment (m)	1 Am^2	1000 emu
Permeability of free space (μ_0)	$4\pi \cdot 10^{-7}$ H/m	1

Table 1: Units and conversions (MKS and cgs)

CHAPTER 2: NANOMAGNETS

2.1 Introduction

Even though the origin of magnetism is quantum mechanical, almost all manifestations of magnetism may be described using classical physics. In fact, many often-cited authors treat magnetism classically [35,36]. This chapter presents magnetism in the framework of the macroscopic Maxwell's equations by postulating magnetic media as an assembly of elementary magnetic moments [36].

The goal of the chapter is to generate a framework for thought, breed insight into magnetic phenomena, and aid in the interpretation of experimental observations. Most topics presented here are relevant to the design of an array of nanostructured magnets that can serve as a high density data storage medium.

2.2 Magnetic Materials

The quasi-classical approach we pursue treats all magnetism as though it were due to charge in motion [35,36]. Atomic current loops give rise to atomic magnetic moments. Orbiting electrons, as well as the spin of electrons and atomic nuclei contribute to the moment of these microscopic currents. Materials may be viewed as made up of these atomic moments throughout their volume. Magnetic classification of materials depends on the tendency of their

atomic moments for alignment, as well as the nature of the atomic moments' response to an applied magnetic field.

2.2.1 Atomic Dipole Moments

Figure 2.1 illustrates an idealized atomic dipole, due to an infinitesimal current loop. The magnetic vector potential of the atomic dipole at point r >> r' is approximated by:

$$\overline{A} = \frac{\mu_0 \overline{m} \times \overline{a}_r}{4\pi r^2} \tag{2.1}$$

where μ_0 is the permeability of free space and $\overline{m}$ is given by:

$$\overline{m} = IdS\overline{a}_z \tag{2.2}$$

Here, r is the distance from the center of the loop to the point where $\overline{A}$ is calculated, $\overline{a}_r$ is the unit vector in the direction of r, and $\overline{a}_z$ is the unit vector in the z direction. The direction of $\overline{m}$ is given by the thumb if the fingers of the right hand curl in the direction of the loop's current.

In most material, the moments are not aligned but assume a random orientation. To magnetize a material is to align these moments with or against an applied magnetic field. A

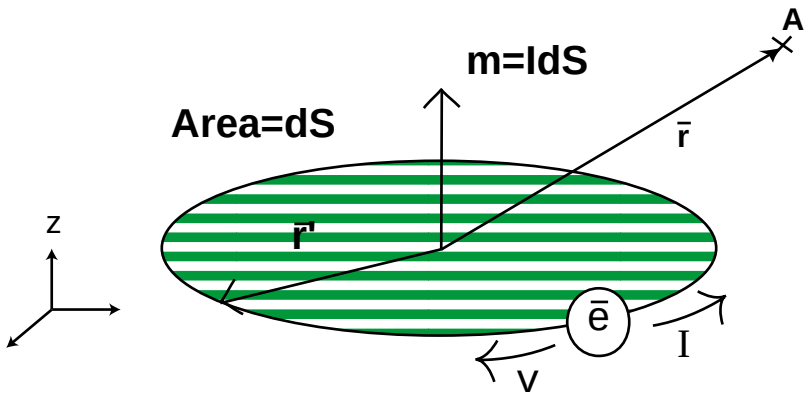

Figure 2.1 Illustration of an idealized atomic dipole due to a circulating charge. The magnetic moment of the moving charge (i.e., a current) is given by the product of the current and the area of the circle enclosed by the current path.

material's magnetization is described by a polarization vector $\overline{M}$, also referred to as the magnetic moment density. $\overline{M}$ is given by the following:

$$\overline{M} = \frac{\sum_i \overline{m}_i}{V} \tag{2.3}$$

where V is the total volume of a body consisting of i moments $\overline{m}$.

2.2.2 Ferromagnetism

A special class of materials exhibits long range alignment of their magnetic moments even in the absence of an applied field. Ferromagnets are a particular subset of these materials. Ferromagnets possess properties suitable for the fabrication of permanent magnets. A ferromagnet's response to an applied magnetic field is highly non-linear and a function of particle shape and material properties. A hysteresis loop (Fig. 2.2) is a plot of a particle's magnetization $\overline{M}$ as a function of the applied field $\overline{H}$. $\overline{M}$ is a hysteretic function of $\overline{H}$ since the processes that align the magnetic moments parallel to the applied field are often non-reversible. As a result, ferromagnetic particles may remain magnetized either partially or in full in the direction of the applied field long after the field is removed. The value of $\overline{M}$ in zero applied-field is known as the remanence, M_r. The maximum magnetization that a magnetic object can achieve

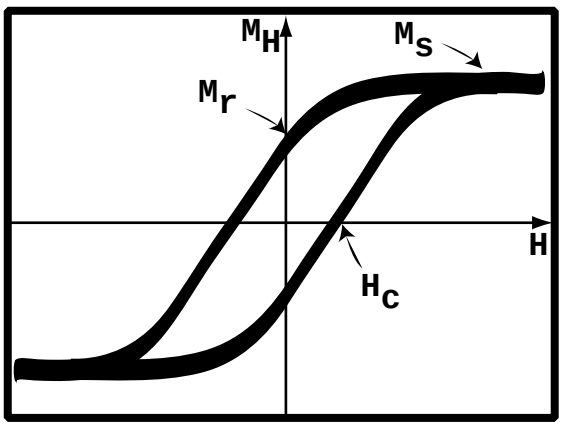

Figure 2.2 This figure illustrates a hysteresis loop which is a plot of the response of the magnetization of a particle to an applied magnetic field. Typically, the magnetization which is plotted on the y-axis is measured in the direction of the applied field, which is plotted on the x-axis. The intersection of the hysteresis loop with the y-axis is the remanence of the particle, while the x-axis intersection of the loop is given by the coercivity field.

is the saturation magnetization, M_S. M_S is a function of temperature. The "squareness" of the magnetic sample is the ratio of the remanence to the saturated moment, M_r/M_S. The coercivity, H_C, of a ferromagnetic particle or ensemble of particles is the field that reduces the magnetization (measured parallel to the applied field) to zero. In a hysteresis loop, the coercivity field is given by the intersection of the loop with the x-axis. The ability of ferromagnets to 'remember' their history renders them suitable for the fabrication of devices for data storage. The three most common examples of ferromagnetic elements are Fe, Ni and Co.

Bulk ferromagnetic materials, as in the door of a refrigerator or a wrench, may exhibit a net magnetization of zero in the absence of an applied field. This is indicative of the presence of domains inside the bulk material. Domains are regions within a material that have a uniform magnetization equal to the saturation magnetization M_S. The total magnetization of a bulk material is equal to the average magnetization over all domains [35]. An illustration of a particle divided into domains such that the net magnetization within the particle is equal to zero is shown in Fig. 2.3a. A particle breaks up into domains in order to reduce its magnetostatic energy by decreasing the spatial extent of its external field [14]. The nanomagnets we

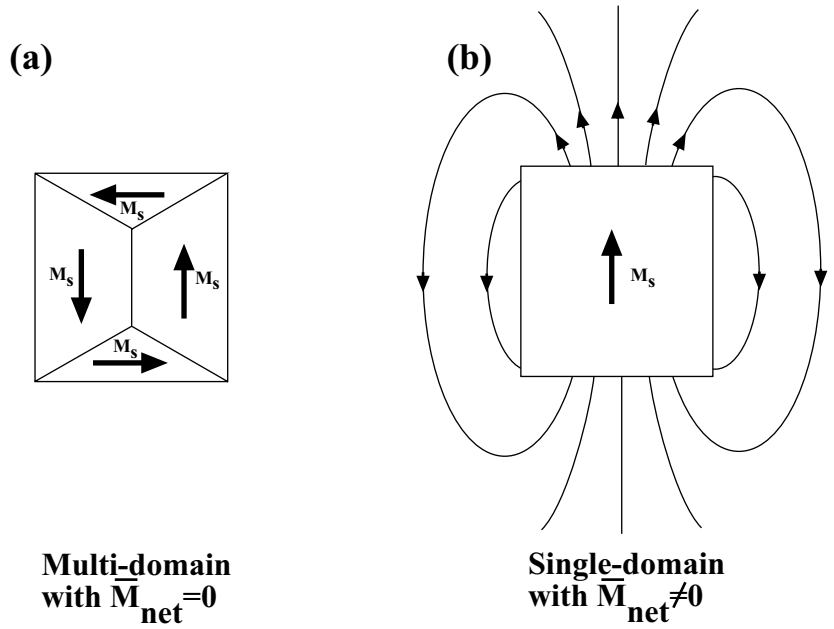

Figure 2.3 (a) A magnetic particle with four closure domains. The vector sum of the magnetization of all domains is zero. (b) A single-domain particle. The net non-zero magnetization of this particle gives rise to an internal magnetic field (not shown) and an external magnetic field.

propose to fabricate must produce an appreciable external field. Since the net magnetization of a body gives rise to its external magnetic field, particles that are single-domains are more suitable for our application (Fig. 2.3b).

2.2.3 Size-Dependent Behavior

Shrinking the size of a particle beyond a critical dimension discourages the formation of multiple domains within the particle. This critical dimension depends on exchange length, λ_{ex}, as well as on particle shape and anisotropy. Exchange forces are short range interactions that keep magnetic dipole moments aligned. The exchange length, λ_{ex}, is of the order of $(A_{ex}/2K)^{-1/2}$, where A_{ex} is a phenomenological constant known as the exchange constant with values in the ~10^{-11} J/m (10^{-6} erg/cm) range. A_{ex} is a function of the spin magnitude, lattice symmetry, lattice constant, and nearest neighbor exchange integral [36]. λ_{ex} of Ni and Co is 20 nm and 7 nm respectively [30]. A particle's magnetization configuration, or direction of dipole moments, results from a complex energy balance within the particle. Shape, material composition, crystal structure, strain, and surface condition contribute magnetic anisotropy energy. Figure 2.4 illustrates example magnetization configurations and corresponding hysteresis loops as a function of a particle's dimensions. Particles much larger than λ_{ex} (Fig. 2.4a) will break up into domains to reduce their magnetostatic energy. The remanence of multi-domain particles is often negligibly small. As the particle's dimensions are decreased to a few λ_{ex}, the formation of domain walls becomes energetically expensive. Domain walls are regions in which the magnetization changes direction to separate domains. In this case, the particle will not form distinct domains (Fig. 2.4b). The magnetization of the particle is in general non-uniform; for instance it can be uniform in the center of the particle and diverge only slightly at the edges of the particle in a flower-like pattern [21], or form a closed vortex structure within the particle [37]. The particles presented in this thesis fall into this size regime. Their measured hysteresis loops will be discussed in the next chapter. As the dimensions of a particle become comparable to a single λ_{ex}, exchange forces will keep the magnetization uniform. If the particle happens to be magnetically uniaxial, its hysteresis loop along the easy axis will be perfectly square. Finally, the magnetization of very small particles may be switched at random due to thermal fluctuations (Fig. 2.4d). Their hysteresis loops demonstrate that a minimal

amount of energy is required to switch their magnetization back and forth, between two opposite directions; such superparamagnetism generates zero coercivity and remanence.

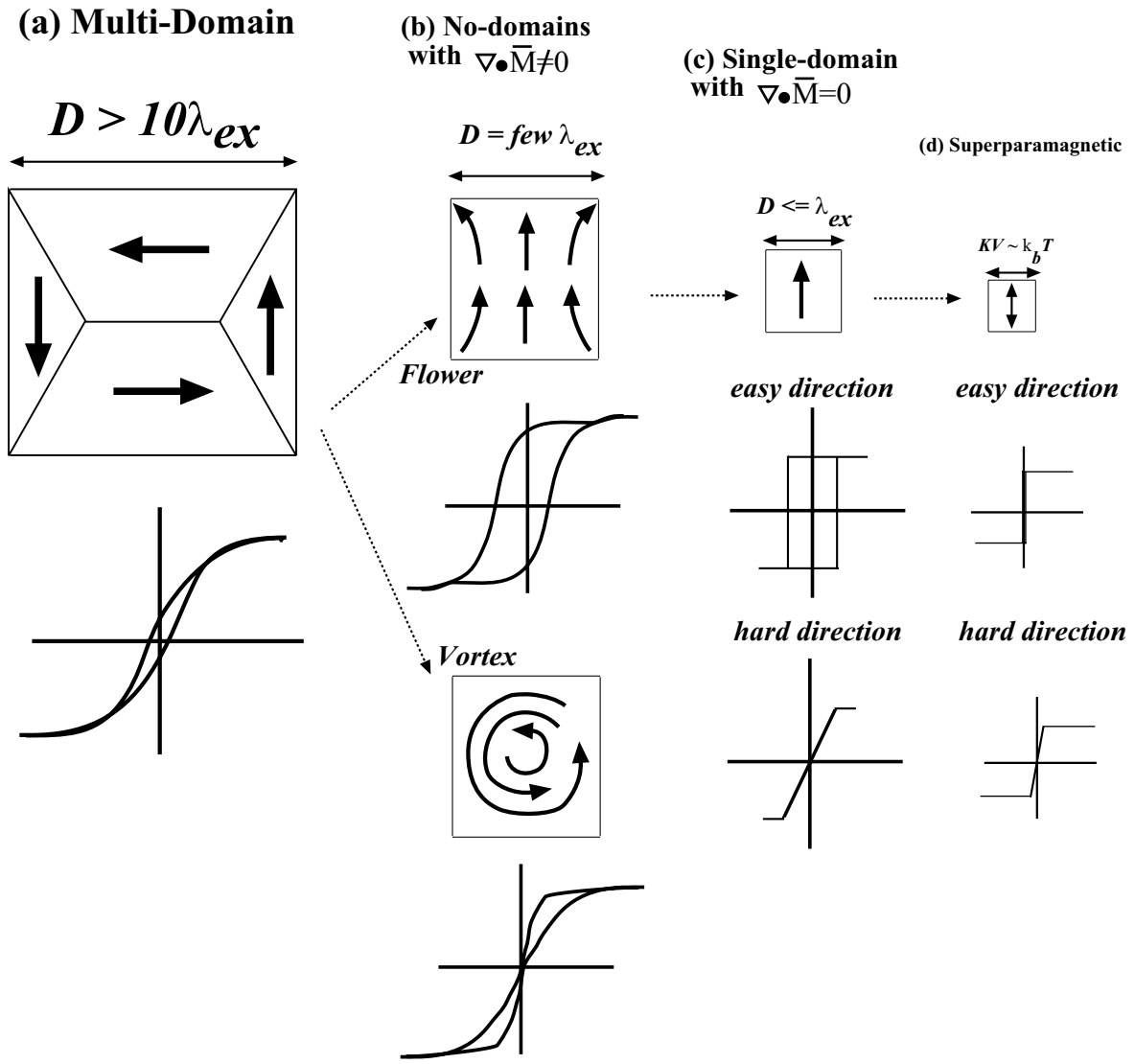

Figure 2.4 Hypothetical scenario of the magnetization configuration of a ferromagnetic particle as a function of the dimensions of the particle compared to the exchange length of the material. (a) For particles that are larger than $10\lambda_{ex}$, the magnetization will form closure domains in order to reduce magnetostatic energy. (b) Particles with dimensions that are a few λ_{ex} will not support domain walls. However, the magnetization will remain non-uniform. (c) In the case where the dimensions of the particle are less than or equal to a single λ_{ex}, the magnetization will be perfectly uniform everywhere inside the particle. (d) Very small particles will have energy barriers that are comparable to thermal energy. Such particles are thermally unstable, or superparamagnetic.

It is worth noting again that the illustrations of Figure 2.4 are hypothetical scenarios of the possible magnetization configuration within a particle as a function of λ_{ex}. The configurations may or may not be achieved depending on all energy contributions within a particle. For example, the presence of strong uniaxial anisotropy may promote the single-domain state at larger dimensions. Furthermore, the particle may become superparamagnetic before it is ever small enough to support uniform magnetization. In reference [38], we report on arrays of Ni particles that behave superparamagnetically at room temperature, even though their magnetization reversal mechanism does not correspond to that of an ideal single-domain particle.

The rest of this chapter will examine in some detail the energy terms that explain the hysteresis behavior of small particles. In particular, we focus on energy terms relevant to the fabrication of single-domain-like nanomagnets with uniaxial anisotropy.

2.3 Magnetostatics

In this section we examine the magnetic fields inside and outside a magnetic particle.

2.3.1 Maxwell's Equations

Equation 2.1 gives the vector potential due to a single dipole at a distance r from the center of the dipole. Given a magnetic body of volume V and magnetization $\overline{M}$, the vector potential of the body is given by:

$$\overline{A} = \frac{\mu_0}{4\pi} \int_{Volume} \frac{\overline{\nabla} \times \overline{M}}{r} dV + \frac{\mu_0}{4\pi} \oint_{Surface} \frac{\overline{M} \times \overline{n}}{r} dS \tag{2.4}$$

where r is the distance from each infinitesimal unit volume within the body to the point where $\overline{A}$ is determined, and $\overline{n}$ is a unit vector perpendicular to the surface of the body [36]. The first term of the right side of equation 2.4 has the form of the potential due to a volume current density J_b,where J_b is defined as:

$$\overline{J}_b = \overline{\nabla} \times \overline{M} \tag{2.5}$$

and the second is similar to the potential of a surface current density $\overline{K}_b$ if:

$$\overline{K}_b = \overline{M} \times \overline{n} \tag{2.6}$$

Therefore, according to our magnetostatic model, the effect of the magnetization $\overline{M}$ on the particle is equivalent to the bound currents $\overline{J}_b$ and $\overline{K}_b$.

To determine the magnetic flux density $\overline{B}$ inside the magnetic body, we apply the differential form of Ampere's Law:

$$\overline{\nabla} \times \overline{B} = \mu_0 \overline{J} \tag{2.7}$$

where J is the total current due to both bound and free currents. $\overline{J}$ is given by:

$$\overline{J} = \overline{J}_f + \overline{J}_b \tag{2.8}$$

The curl of the magnetic field $\overline{H}$ inside the body is equal to the free current $\overline{J}_f$ within the body:

$$\overline{\nabla} \times \overline{H} = \overline{J}_f \tag{2.9}$$

Substituting eq. 2.9 and 2.5 into eq. 2.7 allows us to define the magnetic flux density anywhere in space:

$$\overline{B} = \mu_0 (\overline{H} + \overline{M}) \tag{2.10}$$

The often quoted Maxwell's Equation describes the magnetic flux density $\overline{B}$ as always divergence free; there are no monopole sources of magnetic field:

$$\overline{\nabla} \cdot \overline{B} = 0 \tag{2.11}$$

In the absence of free current, Ampere's Law (eq. 2.7) yields a curl-free magnetic field intensity $\overline{H}$. The curl-free nature of $\overline{H}$ allows us to define it as the gradient of a scalar potential Φ_m:

$$\overline{H} = -\overline{\nabla}\Phi_m \tag{2.12}$$

Using the Gilbert model which describes a magnetic dipole as due to fictitious positive and negative magnetic charges separated by a fixed distance d (Fig. 2.5), the scalar magnetic potential of a dipole moment $\overline{m}$ is:

$$\Phi_m = \frac{\overline{m} \cdot \overline{a}_r}{4\pi r^2} \tag{2.13}$$

where r is the distance from the center of the dipole to the point of observation and $\overline{a}_r$ is the unit vector in the direction of r.

The magnetic scalar potential of a body with magnetization $\overline{M}$ is given by [36]:

$$\Phi_m = \frac{-1}{4\pi} \int_{Volume} \frac{\overline{\nabla} \cdot \overline{M}}{r} dV + \frac{1}{4\pi} \oint_{Surface} \frac{\overline{M} \cdot \overline{n}}{r} dS \tag{2.14}$$

Once more, this scalar potential is the sum of the left term due to an equivalent volume charge density and the right term due to an equivalent surface charge density. The equivalent volume charge density is given by

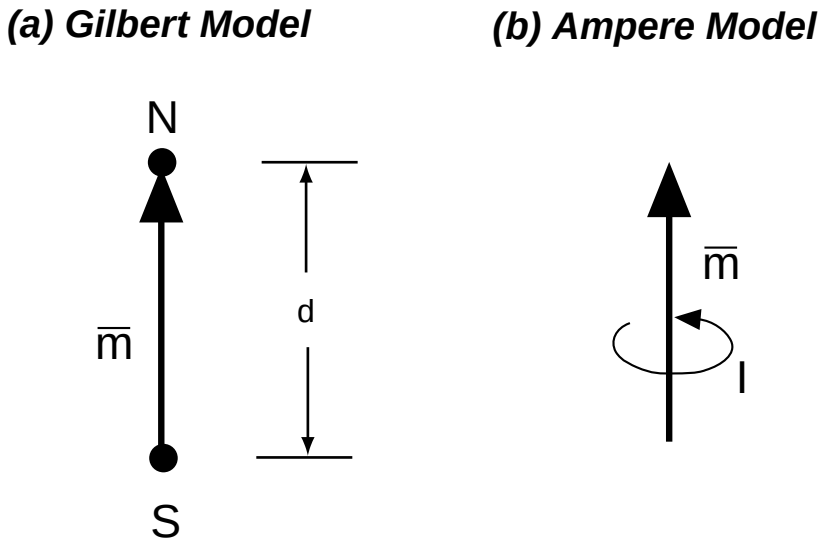

Figure 2.5 (a) A magnetic dipole according to the Gilbert Model is analogous to an electric dipole; that is, the dipole is due to a positive and negative ‘magnetic charge’. (b) Ampere’s model of a magnetic dipole attributes the dipole moment to a microscopic current loop.

$$k_m = -\overline{\nabla} \cdot \overline{M} \tag{2.15}$$

and the equivalent magnetization surface charge density is given by:

$$\sigma_m = \overline{M} \cdot \overline{n} \tag{2.16}$$

2.3.2 Boundary Conditions

The integral form of Maxwell's equations for the magnetic field yield the following boundary conditions on $\overline{B}$, $\overline{H}$, and $\overline{M}$. In all three boundary conditions, $\overline{n}$ is the normal to the surface pointing from region 1 to region 2, according to Fig. 2.6.

1) The normal component $\overline{B}$ is continuous across a boundary:

$$\left(\overline{B}_2 - \overline{B}_1\right) \cdot \overline{n} = 0 \tag{2.17}$$

2) The tangential component of $\overline{H}$ is discontinuous by a free-surface current density $\overline{K}_f$:

$$\overline{n} \times \left(\overline{H}_2 - \overline{H}_1\right) = \overline{K}_f \tag{2.18}$$

In the case of our nanomagnets, the free-current is equal to zero. Therefore, the tangential component of the magnetic field is always continuous unless current is passed through the magnetic object.

3) The tangential component of $\overline{M}$ is discontinuous by the bound current $\overline{K}_b$:

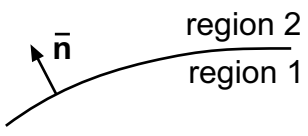

Figure 2.6 Illustration of a unit vector normal to the surface. This vector points from region 1 to region 2, and was defined for the purpose of deriving boundary conditions.

$$\bar{n} \times \left(\bar{M}_2 - \bar{M}_1 \right) = \bar{K}_b \tag{2.19}$$

2.3.3 Magnetic Fields Inside and Outside a Uniformly Magnetized Particle

As an example of magnetic fields inside and outside a uniformly magnetized body, we consider a magnetic sphere in which the magnetization is uniform and points in the positive z-direction (Fig. 2.7a). The magnetization outside the body is equal to 0. Furthermore, in the absence of free currents, H is given by the gradient of a scalar potential (eq. 2.12). Substituting eq. 2.12 into eq. 2.11 yields Laplace's equation:

$$\bar{\nabla}^2 \Phi_m = 0 \tag{2.20}$$

Using boundary conditions, it is fairly straight-forward to solve for the magnetic fields inside and outside a uniformly magnetized sphere with $\overline{M}_{in}=M_0\bar{a}_z$, and radius r_0 [39]. Outside the magnetic body, $\overline{M}=0$ while $\overline{B}$ and $\overline{H}$ are given by:

$$\bar{H}_{out} = \frac{\bar{B}_{out}}{\mu_0} = \frac{2r_0^3 M_0}{3r^3} \cos\theta \cdot \bar{a}_r + \frac{r_0^3 M_0}{3r^3} \sin\theta \cdot \bar{a}_\theta \tag{2.21}$$

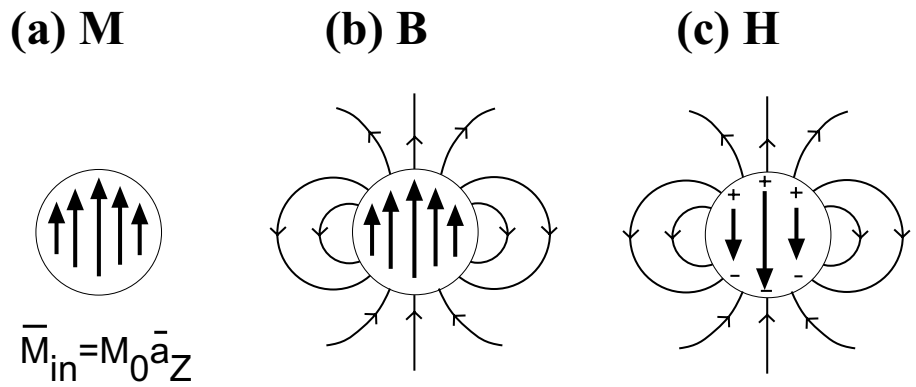

Figure 2.7 The fields of a uniformly magnetized sphere. (a) The magnetization is constant inside the sphere and zero outside. (b) The magnetic flux density is also uniform inside the sphere and is dipole-like outside the sphere. (c) H is a demagnetization field inside the sphere, and points in a direction opposite to the magnetization. Outside the sphere the sphere, the magnetic field H is also dipole-like. This figure is reproduced from [39].

where r is the distance from the center of the sphere to the point of observation. Inside the sphere, the magnetic fields are given by:

$$\overline{B}_{in} = \left(\frac{2\mu_0}{3} \right) \overline{M} \tag{2.22}$$

and

$$\overline{H}_{in} = \frac{-\overline{M}}{3} \tag{2.23}$$

2.3.4 The Demagnetization Field

A general result for all ellipsoidal shapes with uniform magnetization is that the $\overline{H}$ field within the particle will also be uniform but opposite in direction to the magnetization, as seen in equation 2.23. $\overline{H}$ is related to $\overline{M}$ as follows:

$$\overline{H} = N\overline{M} \tag{2.24}$$

$\overline{H}$ inside the body is referred to as the demagnetization field, $\overline{H}_d$, while N is a diagonal tensor known as the demagnetization factor. N_a, N_b and N_c are the diagonal elements of N corresponding to the three principal axes of the ellipsoid. The values of N_a, N_b and N_c are constrained by the following condition:

$$N_a + N_b + N_c = 1 \tag{2.25}$$

For the special case of a sphere, all three principal axes are identical. Therefore, each of the demagnetization factors is equal to 1/3. If the direction of $\overline{M}$ does not coincide with one of the principal axes, $\overline{M}$ may be decomposed into its 3 components along the principal axes of the spheroid. The demagnetization factors hence become the eigenvalues of a demagnetization tensor that is linear when the principle axes are made to coincide with the cartesian x, y, z axes [36]:

$$\begin{pmatrix} H_x \\ H_y \\ H_z \end{pmatrix} = -\begin{pmatrix} N_a & 0 & 0 \\ 0 & N_b & 0 \\ 0 & 0 & N_c \end{pmatrix}\begin{pmatrix} M_x \\ M_y \\ M_z \end{pmatrix} \tag{2.26}$$

The values of N_a, N_b and N_c are quite complex to calculate for the general ellipsoid. However, in the presence of symmetry such as the case of the ellipsoids of revolution, the two demagnetization factors that do not correspond to the symmetry axis are equal. Thus equation 2.25 reduces to:

$$N_{//} + 2N_{\perp} = 1 \tag{2.27}$$

where $N_{//}$ is the demagnetization factor along the symmetry axis and $N_{\perp}$ is a demagnetization factor along any axis perpendicular to the axis of symmetry.

For a prolate ellipsoid, depicted in Fig. 2.8a, $N_{//}$ (z-axis) is given below [14]:

$$N_{//} = \frac{1}{r^2 - 1}\left[\frac{r}{\sqrt{r^2 - 1}}\ln\left(r + \sqrt{r^2 - 1}\right) - 1\right] \tag{2.28}$$

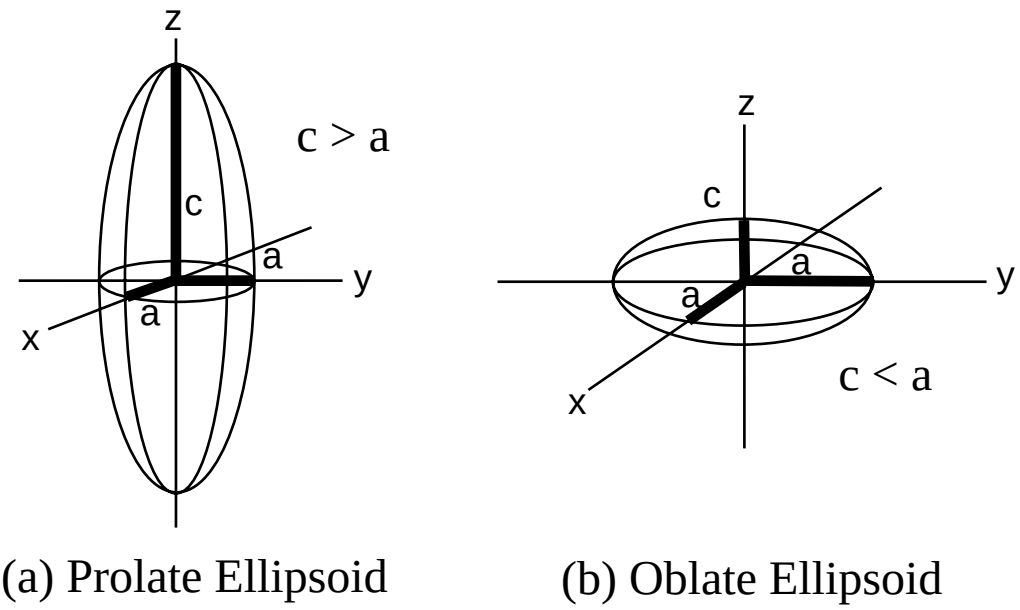

Figure 2.8 (a) A prolate ellipsoid with the axis of symmetry, c, parallel to the z-direction. The minor axes have equal magnitudes, a. (b) An oblate ellipsoid with the axis of symmetry, c, also parallel to the z-direction.

where r = c/a is the aspect-ratio of the particle. In the limit of very high aspect-ratio particles, r>>1, $N_{//}$ ~0 and $N_{\perp}$~1/2. If $\overline{M}$ is parallel to the z-axis, $\overline{H}_d$ ~ 0.

An oblate ellipsoid's symmetry axis is shorter than its other two axes (Fig. 2.8b). The demagnetization factor of an oblate ellipsoid is given by the following:

$$N_{//} = \frac{1}{1-r^2}\left[1 - \frac{r}{\sqrt{1-r^2}}\arcsin\left(\sqrt{1-r^2}\right)\right] \tag{2.29}$$

For r <<1, $N_{//}$ ~ 1 and $N_{\perp}$~ 0. Therefore, in the event that M is parallel to the z-axis, $\overline{H}_d = -\overline{M}$.

Note that the demagnetization factors are a function of the aspect-ratio of the particle rather than the particle's absolute dimensions. This is because the general shape of the particle, not its absolute size, gives rise to a demagnetization field.

The demagnetization field of a particle contributes to the particle's anisotropy. A large demagnetization field can make certain directions unfavorable for magnetization. For instance, the axis of symmetry of an oblate ellipsoid supports a large demagnetization field. Therefore, it is easier to magnetize an oblate ellipsoid of Fig. 2.8b in the xy-plane than parallel to the z-axis.

2.4 Anisotropies in Nanomagnets

Ferromagnetism, at a fundamental level, is due to exchange forces that favor the alignment of neighboring dipoles [36]. Exchange energy is minimized whenever the dipoles are aligned; this effect, however, is symmetrical in space. That is, it does not matter which direction the dipoles point, as long as they all point in the same direction. Our day-to-day experience of magnetic materials contradicts this statement; permanent magnets are not isotropic in space. Several mechanisms give rise to anisotropy in permanent magnets. In this section, we examine the anisotropy mechanisms significant to the design of out-of-plane nanomagnets. Anisotropy effects are described by energy terms that influence the magnetic body.

The nanomagnets we are proposing to fabricate have uniaxial anisotropy perpendicular to the substrate. We label this direction as the z direction, with positive z pointing out of the

plane. Thus the z-axis is an easy axis of magnetization. The x- and y-axes are hard axes. We have already seen in the previous section that the demagnetization field in a prolate spheroid is reduced if the particle is magnetized along its long axis. Thus, the shape of the particle is a source of anisotropy.

The effect of uniaxial anisotropy in a particle is similar to applying a field $\overline{H}_{AN}$ that acts upon the magnetization in the direction of the easy axis. $\overline{H}_{AN}$ is given by:

$$\overline{H}_{AN} = \frac{2K_1}{\mu_0 M} \bar{a}_{AN} \tag{2.30}$$

where K_1 is the uniaxial anisotropy constant of the particle. This field gives a measure of the strength of the anisotropy of the easy axis and the torque necessary to turn the magnetization away from the easy axis [36]. The anisotropy energy of a uniaxial particle is symmetrical with respect to the easy axis. That is, the anisotropy energy density terms, which we explain in the following sections, are an even-function of the angle θ between $\overline{M}$ (Fig. 2.9) and the easy axis as follows:

$$E_{an} = K_1 \sin^2\theta + K_2 \sin^4\theta + ... \tag{2.31}$$

where the higher order terms are usually neglected.

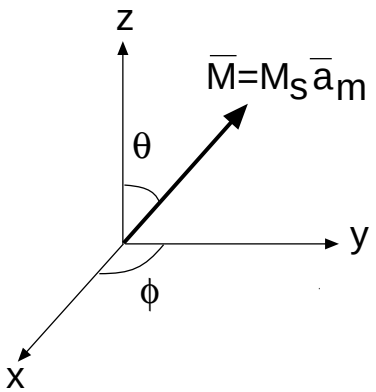

Figure 2.9 The magnetization of a single-domain particle forms an angle θ with the z axis. The vector has a magnitude M_s and a unit vector $\bar{a}_m$.

2.4.1 Sources of Uniaxial Anisotropy in Nanomagnets and Corresponding Energy Terms

In this section we discuss phenomena that give rise to anisotropy in nanomagnets, as well as how to produce uniaxial anisotropy perpendicular to a plane. Anisotropy in nanomagnets is predominantly due to the shape of the particles and the crystalline structure. In this discussion, we ignore magnetoelastic anisotropy present in thin films. We assume that any stress in the particles can relax almost completely because particles are unconfined except at their interface with the substrate. Any field-induced anisotropy is ignored as well [14].

SHAPE ANISOTROPY

Shape anisotropy is a magnetostatic effect that couples the shape of a particle to the direction of magnetization. The demagnetization factors, derived previously, determine the easy direction for magnetization within a particle. The magnetostatic energy density, or self-energy, of the particle is given by [39]:

$$E_m = -\frac{\mu_0}{2}\left(\overline{M} \cdot \overline{H}_d\right) \tag{2.32}$$

The energy of a particle is minimized whenever the magnetization points in the direction of lowest demagnetization field.

Once again, we consider the prolate ellipsoid of Fig. 2.8a. If $\overline{M}$ forms an angle θ with the z-axis, as shown in Fig. 2.9, the magnetostatic energy density of Eq. 2.32 is equal to:

$$E_m = \frac{\mu_0 M_s^{\,2}}{2}\left(N_\perp \sin^2\theta + N_{//}\cos^2\theta\right) \tag{2.33}$$

Equation 2.33 may be rewritten as follows:

$$E_m = \frac{\mu_0 M_s^{\,2}}{2}\left(N_\perp - N_{//}\right)\sin^2\theta + \frac{\mu_0 M_s^{\,2}}{2}N_{//} \tag{2.34}$$

Since this energy is an even function of the angle θ, we conclude that it is a uniaxial energy with a uniaxial shape-anisotropy constant K_s given by:

$$K_s = \frac{\mu_0 M_s^2}{2}\left(N_\perp - N_{//}\right) \tag{2.35}$$

MAGNETOCRYSTALLINE ANISOTROPY

The coupling of the direction of magnetic moments in a magnetic crystal to the axes of the crystal's lattice gives rise to magnetocrystalline anisotropy. The net effect is that there are directions in space along which it is easier to magnetize a ferromagnet than other directions. The difference is expressed as a direction dependent energy term, E(θ), where θ is the angle between the direction of magnetization and the easy axis.

Magnetocrystalline anisotropy is often derived from experimental data on suitable samples [36]. Fe has cubic symmetry and three easy axes corresponding to the three [100] directions of the cubic crystal. Ni, also cubic, has 4 easy axes corresponding to the diagonal [111] directions. Finally, Co has a hexagonal unit cell with a single easy axis of magnetization along the c-axis [0001]. Therefore, Co is the only crystal of these three ferromagnets that is magnetically uniaxial.

A polycrystalline particle will exhibit magnetocrystalline anisotropy only if the easy axis of magnetization of the grains align on average [30]. Magnetic alloys that are amorphous do not exhibit any magnetocrystalline anisotropy.

In crystals where the anisotropy is uniaxial (such as in Co), the magnetocrystalline anisotropy energy is an even function of the angle θ between the direction of magnetization and the magnetocrystalline easy axis. Uniaxial magnetocrystalline energy density is often expressed as:

$$E_{mc} = K_0 + K_1 \sin^2(\theta) + K_2 \sin^4(\theta) + ... \tag{2.36}$$

K_0 is ignored since it does not depend on angle.

2.5 *Total Energy of a Nanomagnet*

The direction of dipole moments, or magnetization configuration, within a particle minimizes the total energy of the particle. In the previous section, we discussed the sources of uniaxial anisotropy energy in a particle of uniform magnetization. We now consider the total energy of a ferromagnet. In addition to anisotropy energy due to shape and the crystal, exchange energy within the particle favors uniform magnetization. Exchange energy increases whenever dipoles are misaligned. That is, exchange energy is present whenever the gradient of the magnetization unit vector $\overline{m}$ is non-zero. If the direction of magnetization changes gradually, exchange energy density is given by [36]:

$$E_{ex} = A_{ex}\left(\left|\overline{\nabla} m_x\right|^2 + \left|\overline{\nabla} m_y\right|^2 + \left|\overline{\nabla} m_z\right|^2\right) + const. \tag{2.37}$$

Finally, the Zeeman energy of a particle in an external field is minimized if the magnetization is aligned with the field. This energy on a unit volume is given by:

$$E_z = -\mu_0\left(\overline{H}_a \cdot \overline{M}\right) \tag{2.38}$$

where $\overline{H}_a$ is the applied field. If α is the angle between the applied field and $\overline{M}$, the energy in equation 2.38 may be written as:

$$E_z = -\mu_0 H_a M_s \cos\alpha \tag{2.39}$$

This energy is minimum whenever α =0.

The total energy within a particle is a sum of the anisotropy, exchange and Zeeman energy:

$$E_{total} = E_{an} + E_{ex} + E_z \tag{2.40}$$

Competition between the different energy terms determines the magnetization configuration that the particle assumes, as well as the mechanisms by which this configuration changes for different fields.

The total energy of a particle depends on the orientation of the magnetization vector $\overline{M}(\bar{r})$. Since $\overline{M}(\bar{r})$ changes in space in all but the smallest ellipsoidal particles which are single-domains, minimizing the total energy is a conceptually and computationaly a non-trivial matter. The field of micromagnetics examines all possible configurations of $\overline{M}(\bar{r})$ that minimize the total energy of any particle [35,36]. Micromagnetics can also determine a magnetization reversal mechanism that minimizes the energy of the particle in the presence of an applied field, as explained in the next section.

2.6 Switching Fields and Mechanisms

The switching field of a uniaxial particle is the minimum field required to rotate the direction of the magnetization by 180º. The magnitude of the switching field depends on the anisotropy of the particle and the mode in which magnetization proceeds within the particle. Here, we identify two reversal mechanisms which are likely to take place in small particles. The switching field is of vital importance since it is the field required to ‘write’ a particle.

2.6.1 Coherent Rotation

Coherent rotation is a magnetization reversal mechanism in which the magnetic dipole moments remain parallel to each other at all times during the reversal process, as illustrated in Figure 2.10. This mechanism is responsible for the magnetization reversal within sufficiently small, uniaxial, single-domain particles (Fig. 2.4c). This form of magnetization reversal was first identified by Stoner and Wohlfarth in their classical 1948 paper [20]. Observations of this form of reversal are rare [38]. Ellipsoidal, 25 nm-Co crystals, prepared by arc discharge, reverse by uniform rotation at a temperature of 6 K [41].

Consider a uniformly magnetized prolate ellipsoid (Fig. 2.11). We apply an external field H_a to this particle. Assuming all anisotropy in the particle is due to shape, the total energy of the particle is given in equation 2.42:

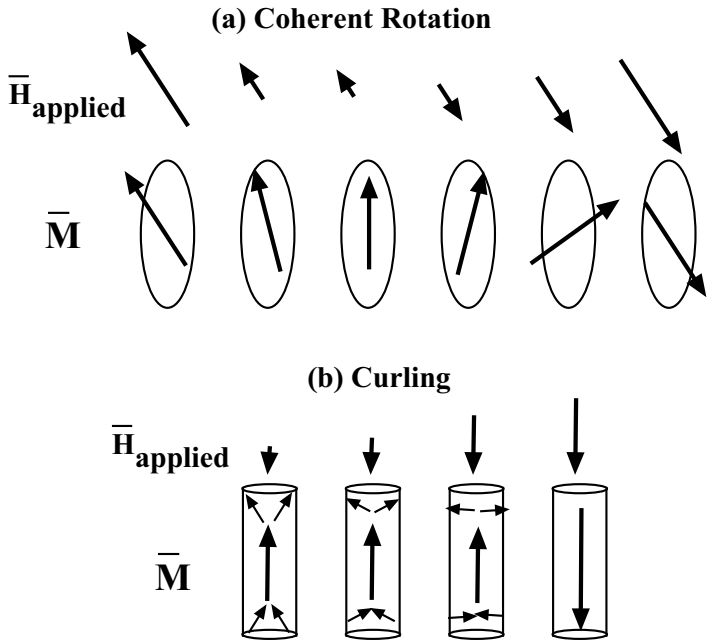

Figure 2.10 (a) An illustration of a single-domain particle reversing its magnetization by coherent rotation. The atomic dipole moments within the particle are parallel at all times yielding uniform magnetization for all external fields. (b) An illustration of a particle reversing its magnetization via a curling mechanism. Initially, the particle's magnetization is non-uniform. As the external field increases, the moments that are not anti-parallel to the external field will begin to rotate. As the external field increases, more moments will align with the external field; however, reversal is achieved in a non-uniform manner. This figure is after [40].

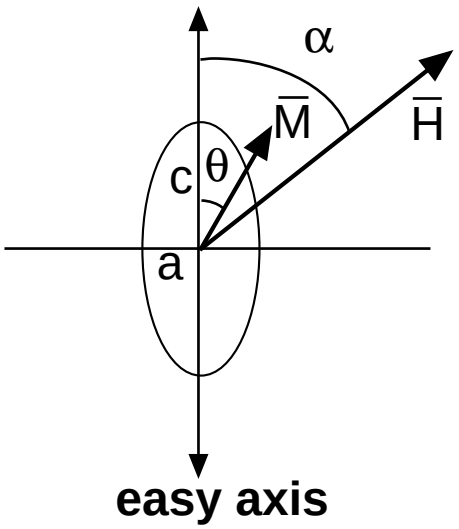

Figure 2.11 This figure illustrates the direction the field H applied to, and magnetization M of an elongated particle in reference to the long axis of that particle.

$$E_{total} = E_{an} + E_z \tag{2.41}$$

$$E_{total} = K_s \sin^2\theta - \mu_0 H_a M_s \cos(\alpha - \theta) \tag{2.42}$$

where K_S is the shape anisotropy and α is the angle between the field and the easy axis of magnetization. The equilibrium position of M_S is also the zero-torque position, that is the angle θ is the solution to [14]:

$$\frac{dE_{total}}{d\theta} = 2K_s \sin\theta\cos\theta - \mu_0 H_a M_s \sin(\alpha - \theta) = 0 \tag{2.43}$$

Suppose the particle is initially magnetized along the positive direction of the easy axis, such that $\theta=0^o$. The magnetizing field H is then reduced to zero and, subsequently, increased in the negative direction of the easy axis ($\alpha=180^o$). The magnetization will become unstable for $\theta=0^o$, and will flip directions whenever the external field exceeds the switching field of the particle. The switching field simultaneously sets the first derivative of the energy (the torque expressed in equation 2.44) and the second derivative of the energy with respect to θ equal to zero. The switching field is derived in ref. [14] and is given by:

$$H_{sw} = \frac{2K_s}{\mu_0 M} \tag{2.44}$$

Coherent rotation in single-domain particles produces square hysteresis loops for magnetization along the easy axis (Fig. 2.4c). If the applied field is perpendicular to the easy axis, i.e. $\alpha=90^o$, the magnetization is a linear function of applied field. Saturation along the hard axis is achieved if the applied field exceeds the switching field of equation 2.44 [14].

. Since coherent rotation minimizes exchange energy by keeping the magnetization uniform during reversal, it is favored in very small particles where exchange forces prevail. Also, this model assumes the shape of the particle is a perfect ellipsoid. Therefore, it is very difficult to observe this form of reversal experimentally since any defect or edge roughness will give rise to non-uniform reversal [42].

2.6.2 Curling

Curling is a non-coherent solution that minimizes the total energy of eq. (2.41), and is often suggested as the reversal mechanism of structures that are several λ_{ex} [43]. Curling may proceed as illustrated in Fig. 2.10b.

Curling is identified by a nucleation field, H_n, that indicates the onset of magnetization reversal. Curling is popular among experimentalists trying to fit their data to a model since H_n may be derived analytically from a linearized set of differential equations describing the energy of an ellipsoid [35]. The curling nucleation field is given below:

$$H_n = -\frac{2K_1}{M_s} - \frac{2A_{ex}q^2}{R^2 M_s} + N_z M_s \tag{2.45}$$

where R is the semi-axis of the spheroid perpendicular to the easy axis, and q is a constant that depends on the aspect ratio of the particle [36].

It is instructive to note that the curling solution was derived assuming the particle is an ellipsoid. The applied field is always in the direction of the easy axis; the spheroid is first saturated in one direction. The applied field is slowly decreased to zero, and then increased in the opposite direction. Therefore, curling may or may not hold for more general shapes and fields.

2.6.3 Micromagnetics

As stated previously, the field of micromagnetics is concerned with finding the magnetization in all of space that minimizes the total energy (eq. 2.41). In the case of complex bodies and multiple anisotropy sources, it is difficult to predict intuitively how the magnetization will reverse.

The motion of the magnetization toward equilibrium is described quantum-mechanically by the Landau-Lifshitz-Gilbert (LLG) equation [44]:

$$\frac{\partial \overline{M}(\bar{r})}{\partial t} = -|\gamma|\overline{M}(\bar{r}) \cdot \overline{H}_{eff} + \frac{\alpha_d}{M_s}\overline{M}(\bar{r}) \cdot \frac{\partial \overline{M}(\bar{r})}{\partial t} \tag{2.46}$$

where γ is a quantum mechanical term describing the frequency of magnetic moments precessing about an applied field, and α_d is a phenomenological damping term. H_{eff} is the effective field acting on the body due to forces of exchange, anisotropy and any externally applied field.

In a micromagnetic simulation, a body is subdivided into finite elements. The LLG equation is solved for each element until a local energy minimum is reached.

The particles presented in this thesis are not ellipsoids. Recently [30], our research group conducted micromagnetic simulations of the equilibrium magnetization configuration of truncated-cone-shaped particles. In a real particle, defects tend to provide sites for reversal to begin. Therefore, switching fields from micromagnetic simulations of model particles that do not account for impurities and defects often overestimate the switching fields in comparison to experimentally observed fields.

CHAPTER 3: FABRICATION

In this work, we employ the planar fabrication process to manufacture periodic arrays of nanostructured magnets. This process is used in the fabrication of integrated circuits, and has been a key enabler of the rapid development of semiconductor technology. The planar process has three main components. First, a lithography step forms a relief image in a resist layer [45]. Next, the pattern in resist, or its negative, is transferred by subsequent material removal and/or deposition steps. Finally, excess material is removed, leaving behind the desired structures on the substrate of choice. This chapter has excerpts from reference [A6] in Appendix A.

3.1 Fabrication Processes

A goal of this investigation is the study of nanomagnets with a variety of physical characteristics. To this end, we designed three sets of processes for the fabrication of arrays of nanostructured magnets; each process is well suited for producing arrays of nanomagnets with unique characteristics. The major process steps are illustrated in Fig. 3.1. The first two processes are of an additive nature. In other words, a template of holes is formed on the substrate; magnetic material is deposited into those holes. Figure 3.1a illustrates the deposition of magnetic material into a template via electroplating. In this process, the substrate is initially coated with a plating base. Holes in resist (step 1) are transferred by reactive-ion etching (RIE) into the underlying thin SiO_2, and subsequently into an anti-reflection coating (ARC) polymer. The substrate shown in step 2 is immersed into a plating bath of a ferromagnetic electrolyte, and electrical-contact is made to the plating base. This process can produce magnetic cylin-

ders (or posts) as tall as the plating template. Since the plate conforms to the template, this process is well suited for the fabrication of high-aspect-ratio magnetic structures.

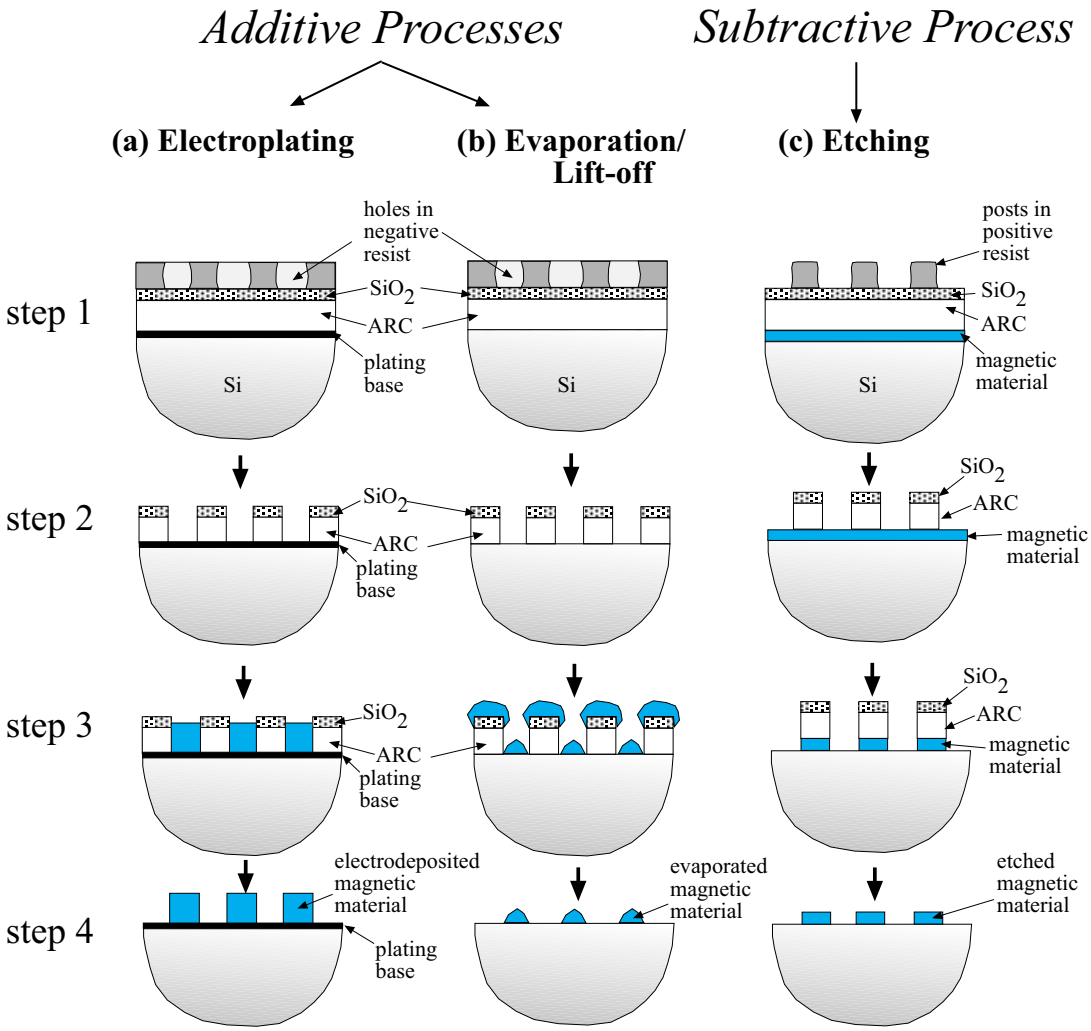

Figure 3.1 Fabrication processes employed for manufacturing arrays of nanostructured magnets. Additive processes pattern a template of holes suitable for the deposition of magnetic material. (a) Magnetic material may be deposited via electroplating if the substrate is initially coated with a plating base. (b) Otherwise, magnetic material may be deposited by evaporation. Excess material as well as the evaporation-template may be removed by lift-off techniques (step 4). (c) Substrates initially coated with a thin magnetic film may be patterned using a subtractive process. Certain regions of the thin film are protected with an etch mask. Unprotected regions are removed by suitable etching techniques.

Often, arrays of shallow magnetic particles are desired. Shallow particles possess a smaller magnetic volume. Hence, their stray field is small and less likely to disturb the magnetization of their neighbors. In a less complex process than electroplating, magnetic material is simply evaporated into the ARC template (Fig. 3.1b). After material deposition, the template is dissolved, and excess magnetic material is removed via lift-off (step 4). This process is suitable for producing pancake-shaped particles as well as cones and truncated cones.

In other instances, we are presented with a magnetic-thin-film-coated substrate, and wish to pattern isolated magnetic islands. In such cases, patterning must proceed via a subtractive process. A subtractive process transfers an array of posts in the photoresist layer into the underlying layers to produce an etch mask for the magnetic thin film (Fig. 3.1c). Unmasked magnetic material is removed with an adequate etch process (step 3). We employ a subtractive process when fabricating prototype magnetic elements for magnetic random access memory (MRAM) applications. The manufacture of MRAM cells entails several aligned lithography steps; the MRAM memory element is often produced first, as outlined in Fig 3.1c [46]. After step 3, the mask is removed and the substrate, now covered with an array of magnetic islands, is prepared for subsequent lithography steps.

In this thesis, we concentrate on additive processes to produce arrays of nanomagnets for hard-disk-like data storage. Unlike a hard-disk, however, we are requiring our magnetic bits be perpendicular to the plane of the substrate. In an additive process, out-of-plane easy axis may be achieved by taking advantage of the phenomena of shape and magneto-crystalline anisotropy. Concurrent efforts in our research group are investigating subtractive processes by patterning films which possess out-of-plane anisotropy such as Co/Pt multilayers [7].

3.2 Lithography

The lithography (or patterning) step in a planar process is traditionally achieved by exposing the resist to a radiation pattern of sufficient energy. Early work reported producing arrays of nanostructured magnets by scanning-electron-beam lithography [47, 18], as well as embossing (or mechanically imprinting) a surface relief structure in photoresist or other suit-

able polymers [48]. We will discuss the suitability of available resist patterning techniques for our specific application.

Any patterning scheme we employ must satisfy the following criteria:

1) Resolution

We aim to understand the transition of particle magnetization from the multidomain state to the single-domain state. In Chapter 2, we demonstrated that isolated particles of Ni and Co lose the ability to support multiple domains whenever their linear dimensions approach a few λ_{ex}. Our simulations indicate that the critical dimension is order of $10\lambda_{ex}$ or ~ 200 nm for Ni particles and ~ 100 nm for Co particles [30].

2) Large Areas

The magnetic signal of a single particle is proportional to its magnetic volume. We must fabricate nanomagnets over areas that are large enough to guarantee a magnetic signal that is detectable by standard magnetometry techniques. Furthermore, large areas of nanomagnets are necessary to demonstrate the suitability for practical applications.

3) Speed

Speed or high throughput may seem less critical in an academic research environment where we focus on the study of the physics of nanomagnets and not on the production of high volumes of storage devices. However, a truly exhaustive study of nanomagnet arrays requires producing a large number of samples of nanomagnets with varying sizes and materials. Additionally, high throughput is a most necessary requirement of a lithography system with commercial viability.

Finally, any lithography which may be used in the future manufacture of hard disks must be cost effective, in order to justify replacing the simple, and relatively inexpensive method of manufacturing magnetic disks in hard drives today.

Prototype patterned media with feature sizes of 35 nm and above have been successfully generated with scanning electron beam lithography (SEBL) [3,47,49,50]. SEBL possesses ample resolution and a capability to generate patterns of arbitrary geometries; however, the slow, serial pattern-writing mode delivers prohibitively low throughput. Embossing tech-

niques such as nano-imprint lithography (NIL) show promise in the throughput arena. However, these schemes have yet to demonstrate distortion-free patterns over large areas.

Interference lithography (IL), a lithography scheme that interferes coherent radiation as a means of generating patterns, has proved most versatile for the purposes of this investigation [16,51-56]. Exposing photoresists with IL is a fast (< 1 min.) process that does not require a mask. Furthermore, an IL generated pattern covers large areas of substrate from 3 to 5 sq. cm.

3.2.1 Interference Lithography

MIT's Space Nanostructures Laboratory (SNL) houses the IL apparatus illustrated schematically in Fig. 3.2a. This system was used to pattern all structures presented in this thesis.

EXPLANATION OF THE SYSTEM

The light source in Fig. 3.2a is an argon-ion laser emitting linearly polarized light of wavelength λ = 351.1 nm. Interference lithography (IL) is implemented in this system by dividing the main beam into two secondary beams (or arms) of equal power and, subsequently using mirrors to redirect the secondary beams such that they are made to interfere. Before they interfere, however, each secondary beam is focused with a lens, and expanded with pinholes that emulate spatial filters. The interference pattern of the expanded beams is a sinusoidal standing wave in space of period P given by:

$$P = \frac{\lambda}{2\sin\theta} \tag{3.1}$$

where λ is the wavelength of the light, and θ is half the angle between the two beams. A pattern of lines of period P may be recorded in a photoresist film that covers a substrate. The substrate is placed at the location of interference (see Fig. 3.1a and b). This system can be set-up to expose periodic patterns with periods from 200 nm to approximately 4 μm [57].

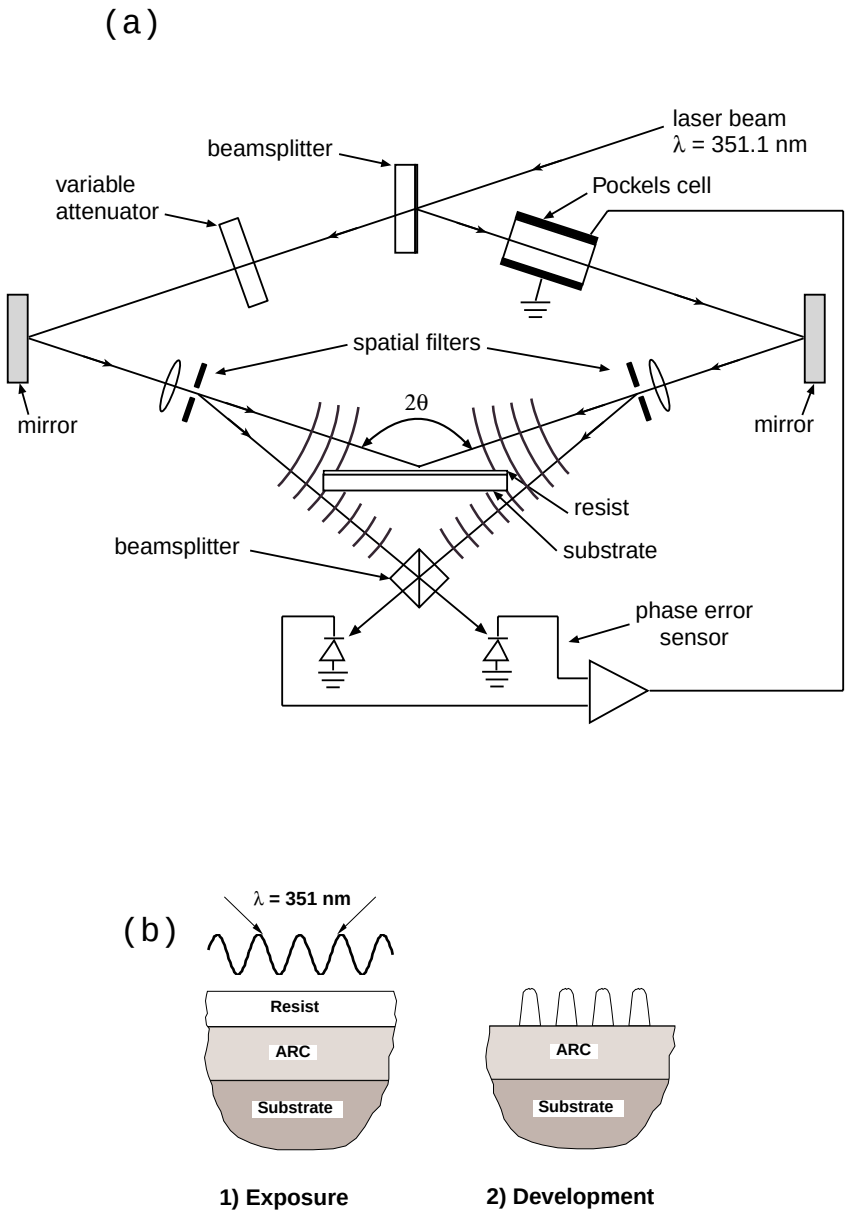

Figure 3.2 An implementation of interference lithography, located in MIT's Space Nanostructures Laboratory. This figure is due to Dr. Mark Schattenburg. (b) A simple lithography stack shown before and after the development of the photoresist which was exposed to an IL-created standing wave. (b) is from [57].

The feedback system which is depicted in Fig 3.1a keeps the interference pattern static in space for the duration of an exposure by maintaining equal optical path lengths in the two interfering beams. Variations in the optical path length of the two arms lead to variation in the spatial position of the interference pattern and, hence, to a reduction in contrast of the resulting image [57].

A single IL exposure produces a grating in resist. Two-dimensional grid patterns are readily generated by rotating the substrate 90° after the first exposure, and performing a second exposure. Assuming equal exposure times for the two exposures, the incident dose distribution is the superposition of two perpendicular sinusoidal standing waves, which can be expressed as:

$$I = A\sin^2\left(\frac{\pi}{P}X\right) + A\sin^2\left(\frac{\pi}{P}Y\right) \tag{3.2}$$

3.2.2 Image Contrast of Two Perpendicular Exposures

A plot of equation (3.2) is shown in Fig. 3.3a. The peaks correspond to the superposition of the maxima of the perpendicular X and Y sinusoids, the minima correspond to the superposition of two minima, and the saddle points separate consecutive maxima and minima. The dose at the peaks is 2A, at the minima is 0 assuming the incident beams are exactly matched, and at the saddle point is A. When imaging 2-D structures, such as arrays of holes or arrays of posts in photoresist, one can choose to define these features either at the minima or the maxima, depending on the polarity of the resist used.

We illustrate in Fig. 3.3b and c that a higher contrast and hence a broader process latitude is realized if the critical features (the holes or the posts) are imaged at the minima. That is, the minima can be used to expose posts in positive resists or holes in negative resists. If one were, for example, to use the maxima in Fig. 3.3a to expose holes in a positive resist, then areas in between the holes would receive a dose (i.e., A) equal to half that at the hole locations (i.e., 2A). This would have the consequence of reduced image contrast and greatly reduced

exposure latitude. Image contrast, which is defined as $K=(I_{max}-I_{min})/(I_{max}+I_{min})$ is equal to 1/3 in Fig. 3.3b, which represents a cut through the maxima, and is equal to unity in Fig. 3.3c, which represents a cut through the minima. Hence, with IL, it is preferable to use positive resists to create posts and negative resists to create holes. The scanning electron micrographs (SEMs) of Fig 3.4a demonstrate a typical attempt at producing a pattern of holes in positive

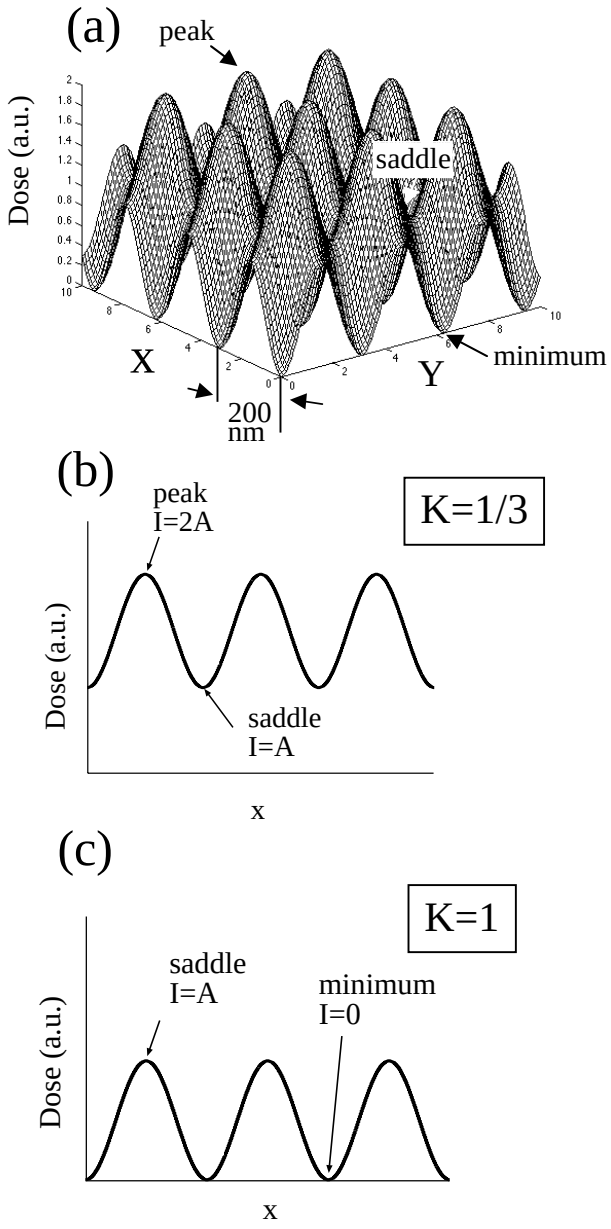

Figure 3.3 Plot of the dose distribution impinging upon the resist as a result of the superposition of two perpendicular grating exposures of equal amplitude. The dose at the peaks is twice the dose at the saddle points. At the minima, the dose is zero. (b) Cross section through the peaks and saddle points. In this case, the contrast $K=(I_{max}-I_{min})/(I_{max}+I_{min})=1/3$. (c) Cross section through the saddle points and minima. The contrast K=1.

resist. Ideally, the full thickness of the resist at the saddle points is kept intact after the exposure; the SEMs indicate that more than half thickness of the resist at the saddle points was developed away. In contrast, the array of holes in Fig 3.4b were printed in negative resist. The thickness of the resist at the saddle point where the resist received half the maximum dose seems identical to the height of the resist at the apex where the resist received the maximum dose.

The issue of whether to use a positive or a negative resist in IL also arises in the fabrication of gratings in which the linewidth is not equal to the space width. To treat this quantitatively, we define the duty cycle of a grating as the ratio of the linewidth to the spatial period,

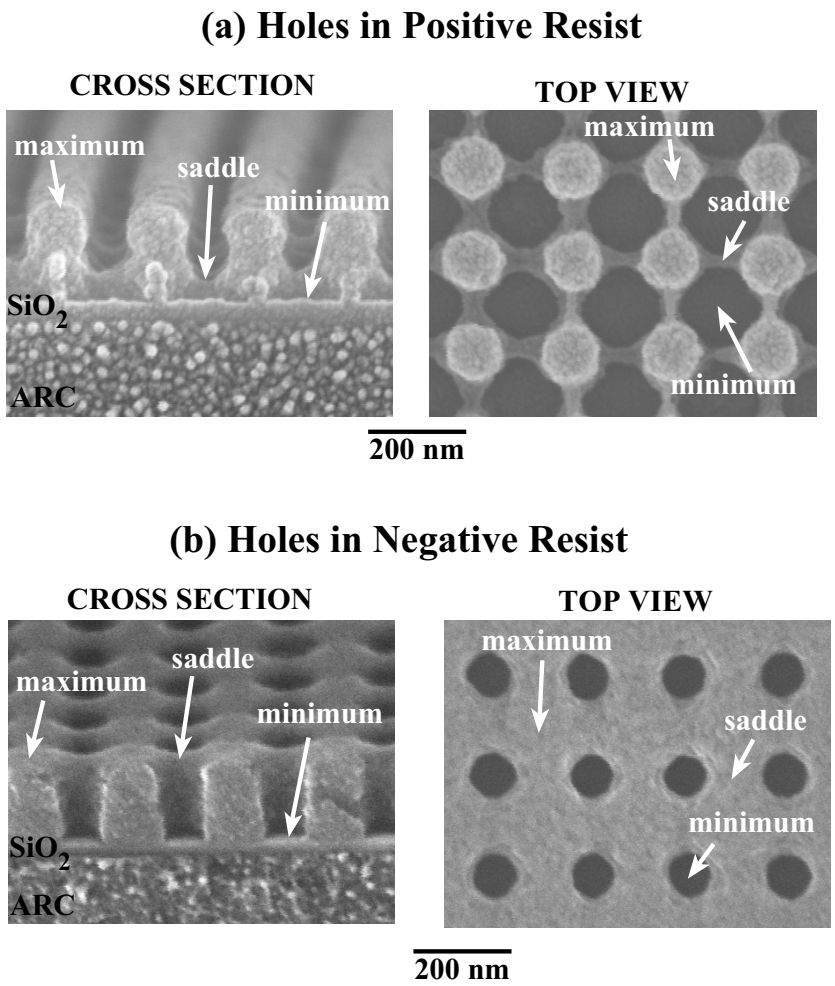

Figure 3.4 (a) Array of holes printed in positive photoresist. Poor image contrast results in wide holes and very thin walls. (b) An array of holes in negative photoresist. A negative resist allows us to control the dimensions of the holes, and to produce thick walls that are appropriate etch masks for the underlying layers.

L/p. We assume an infinite contrast for the resist, i.e., above a given threshold dose a positive resist is totally removed and below the threshold dose a negative resist is totally removed. Figure 3.5 plots the change in duty cycle with respect to a change in the dose, a measure of process latitude, as a function of the grating duty cycle. For duty cycles of greater than 50%, as in the case of wide lines and narrow spaces, the duty cycle changes less quickly for small changes in dose if a negative resist is employed. Appendix B describes how the plot of process latitude vs. duty cycle in Fig. 3.5 was obtained.

3.2.3 Negative Tone Imaging

In order to create large-area arrays of nanomagnets with dimensions in the 100 nm range, using either electroplating or lift-off, a negative resist is preferred, as discussed above. Negative tone imaging may be implemented via image reversal of a positive-tone-working resist or by using a true negative-tone photoresist [58]. We found that positive working resist commonly used for image reversal at G-line wavelengths, such as the AZ5214 resist, do not possess the resolution necessary for printing 100 nm-dense lines and spaces. Appendix C con-

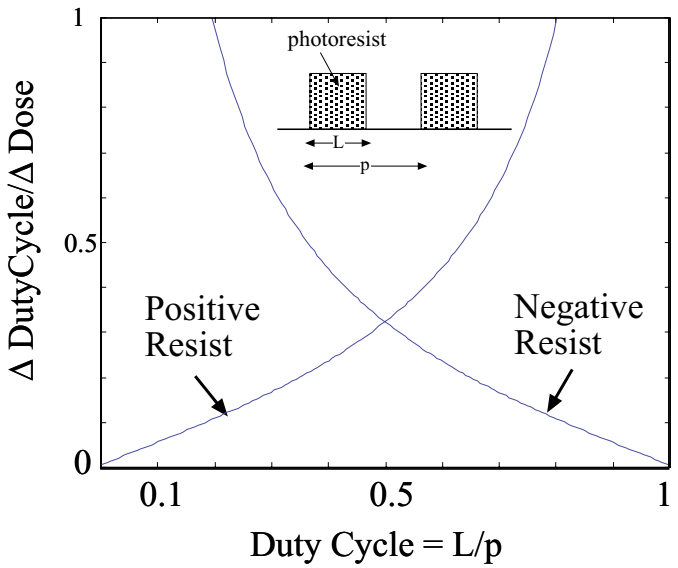

Figure 3.5 Comparison, for positive and negative resist, of the change in duty cycle with respect to a change in dose, as a function of duty cycle. Duty cycle is defined as the ratio of resist linewidth to period. For a duty cycle above 0.5, a negative resist is preferred, i.e. reduced sensitivity of change in duty cycle to change in dose.

tains SEMs of a failed attempt to print a 200 nm-period grating in AZ5214 using IL in the negative and positive tone, as well as coarse features in the negative tone. Early in this investigation, we reported a first demonstration of IL in a negative, chemically-amplified photoresist (OHKA THMR-iN PS1). We have successfully patterned 200 nm-period gratings as well as arrays of holes with precisely controlled diameters down to 56 nm. This photoresist is a chemically amplified resist.

CHEMICALLY AMPLIFIED PHOTORESIST-A BRIEF INTRODUCTION

Chemical amplification chemistry, conceived at IBM by Ito, Wilson and Frechet in the early eighties, was developed to increase the sensitivity of photoresist for sub-100 nm resolution [59]. Initial successes were accompanied by severe problems which kept CA resist from enjoying wide spread use for many years. Most notable among those problems is the resist's sensitivity to airborne bases which could potentially enter the film's surface and quench the photoacid. Since then however, each new generation of CA resist is significantly improved as different methods of enhancing environmental stability are developed [59].

The basic components of the CA negative resist we are using are the photoacid generator, the base resin, and a binder. The imaging mechanism proceeds as follows. The exposing radiation causes the photogeneration of an acid. The photogenerated acid, upon heating, activates the binder. The binder effects a crosslinking event which, upon completion, releases an acid that is free to catalyze a second crosslinking event. Appendix D illustrates this.

3.2.4 Characterizing THMR-iN PS 1 Chemically Amplified Negative Photoresist

LITHOGRAPHY STACK

Figure 3.6a depicts the multilayer lithography stack used in characterizing the negative resist. The interference pattern is recorded in the photoresist film. Silicon substrates are reflective; therefore, the anti-reflection coating layer (ARC) polymer is critical to minimize backreflection into the resist layer which would otherwise degrade process latitude. The SiO_2 interlayer acts as an etch mask for the bottom ARC since the ARC and photoresist etch in similar chemistries. An analytical model was developed in our group to calculate backreflection at

the resist/SiO_2 interface given the real and imaginary indices of refraction of the several layers [60]. We adjust the thickness of the ARC and SiO_2 to achieve minimum backreflection into the resist. This method of protecting the ARC with an interlayer during the transfer of patterns from the resist to the ARC was developed at MIT and is known as the tri-layer imaging process [60]. We employ tri-layer imaging throughout this work for the fabrication of arrays of nanomagnets via additive processes: an array of holes in the resist is transferred into the ARC; the ARC becomes the mold or template for material deposition. For the initial study of the resolution and process latitude of the negative resist, a Brewer Science (XHR-i) ARC was employed. Details of the process including bake time and temperature are listed in Appendix E. Following the exposure, the resist is post-baked at a temperature of 100º to 110º C for 90s. The resist is developed in an 0.26 N tetra-methyl ammonium hydroxide (TMAH) solution.

RESULTS

Figure 3.6b portrays the profiles obtained at a dose of 22 mJ/cm^2. Figure 3.7a is a plot of grating linewidth as a function of dose. Defining process latitude as the change in the dose

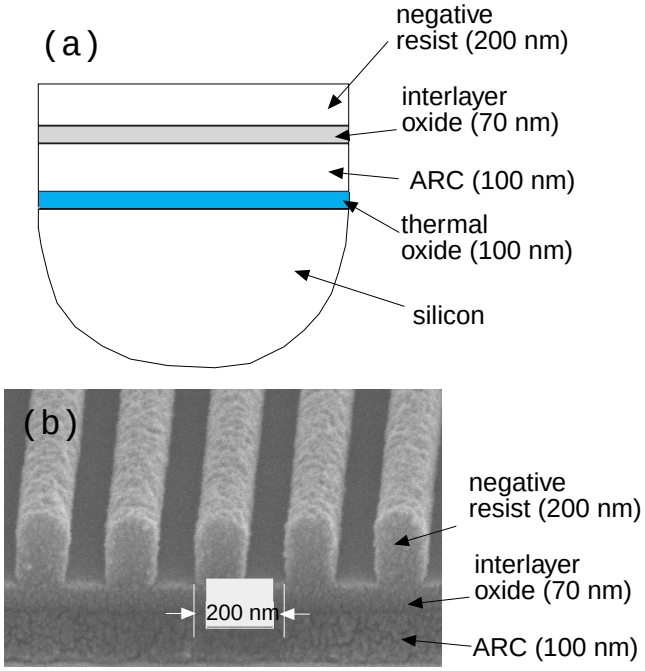

Figure 3.6 (a) The tri-layer used in interference lithography. Silicon wafers with a 100 nm of thermal oxide are coated with ARC, and e-beam evaporated oxide and a negative photoresist imaging layer. (b) Scanning-electron micrograph of a 200 nm-period grating in THMR-iN PS1 negative resist after exposure and development.

necessary to produce a 10% change in linewidth, we estimate a process latitude for printing gratings of about 30%. Figure 3.7b illustrates the process latitude and precise control of hole diameter we achieve with the THMR-iN PS1 negative resist. The process latitude for printing holes is about 15%.

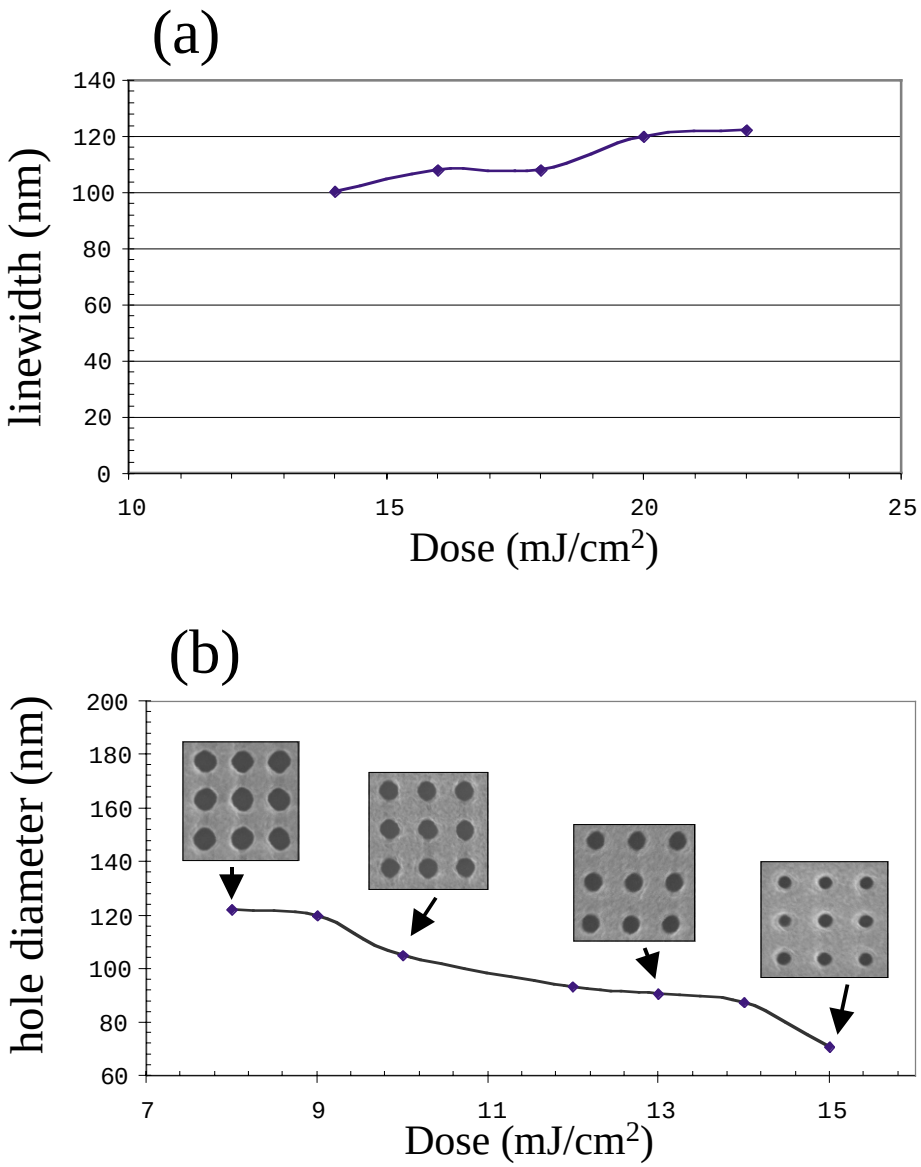

Figure 3.7 (a) Plot of grating linewidth exposed in THMR-iN PS1 negative resist, as a function of exposure dose, illustrating process latitude. (b) Plot and micrographs illustrating the dependence of hole diameter on exposure dose in THMR-iN PS1 negative resist.

3.3 Pattern Transfer

The response of the THMR-iN PS1 negative resist, reported in Fig. 3.7a and b, enables us to fabricate arrays of magnetic dots with a fixed period and a variety of particle diameters. Therefore, we can study the behavior of individual magnetic particles and the extent of interactions among the neighbors as a function of array geometry and particle volume.

Following the lithography step, holes in photoresist are transferred into the interlayer oxide by reactive ion etching in a CHF_3 plasma at a 300 V DC bias. Subsequently, the ARC is etched in an O_2 plasma. Experience has shown that if the ARC thickness is in excess of 100 nm, a chilled (sub-0º C) ARC etch achieves better fidelity in linewidth transfer.

Initially, we chose to fabricate nanomagnets out of "pure" Ni and Co as opposed to ferromagnetic alloys or more complex magnetic compounds. We are also pursuing investigations of electroplated CoP and Ni_xCo_{1-x} [61]. CoP is interesting since the stoichiometry of the plating may be controlled such that an amorphous film, with zero magnetocrystalline anisotropy, is achieved. Table 3.1 summarizes the physical and magnetic properties of Ni and Co. The Co crystal has hexagonal close-packed symmetry. The axis of symmetry for the hexagon is the c-axis which is also an easy axis of magnetization since $K_1 > 0$. Ni on the other hand is cubic, and, since $K_1 < 0$, the axes of the cube are hard axes. The <111> directions are easy directions. If the <111> directions are perpendicular to the substrate they induce out-of-plane anisotropy in the nanomagnets. The saturation magnetization M_s of Co is approximately three times that of Ni. Finally, the exchange length of Co is much smaller than the exchange length of Ni.

Material Properties		
	Ni	**Co**
Crystal	fcc	hcp
M_s	484 emu/cm^3	1422 emu/cm^3
K_1	-0.5· 10^5 erg/cm^3	45· 10^5 erg/cm^3
K_2	-0.2· erg/cm^3	15· erg/cm^3
λ_{ex}	20 nm	7 nm

Table 3.2: Physical and magnetic properties of Ni and Co.

3.3.1 Electroplating

Electrodeposition is well suited to generating high aspect ratio structures. In an electrodeposition process, the plated metal conforms to the walls of the plating template. The substrate is coated with a thin plating base (or plating seed layer). The plating base of choice consists of 20 nm of Au. Au is preferred because it does not form an oxide. We use 5 nm of Cr to promote adhesion of the Au to the substrate. We are able to transfer holes from the photoresist into the ARC that are as small as 80 nm with a 200 nm pitch. Assuming we would like to form magnetic cylinders with aspect-ratio AR =2.5, the ARC must be at least 200 nm thick. To avoid the risk of overplating, we often use an ARC thickness in excess of the minimum requirement. Fig. 3.8a and b show holes in resist before and after pattern transfer into the ARC. Note that the 15 nm SiO_2 layer is an adequate etch mask for 250 nm-thick ARC.

Plating follows pattern transfer into the ARC. Our simple plating apparatus was described previously in [62]. The apparatus consists of a beaker containing an electrolyte of a ferromagnetic element such as Ni or Co, or an alloy such as CoP. The negative electrode of a power supply makes contact to the plating base of the substrate. Subsequently, the substrate is immersed in the plating beaker (Fig. 3.9). The positive electrode of the power supply is connected to a Ni anode that is partially immersed in the same beaker. The substrates are plated shortly after reactive ion etching of ARC in an O_2 plasma, thus the surface of the exposed Au at the bottom of the holes does not need to be cleaned further. As part of our nanomagnet investigation effort, we have plated Ni from a sulfamate solution, Co from both a sulfamate and a sulfate solution and finally CoP. Dr. Mutsuhiro Shima is currently investigating the fea-

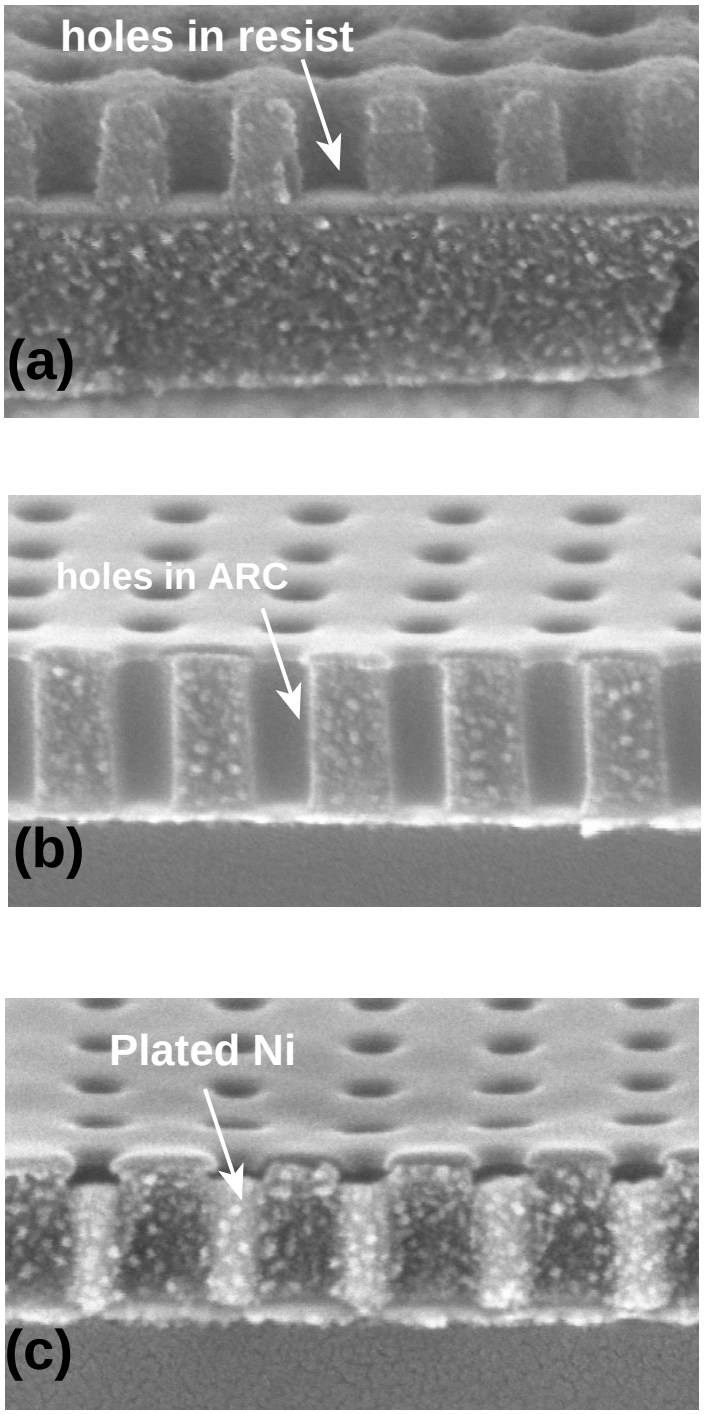

Figure 3.8 Scanning electron micrographs of the process steps for electroplating arrays of nanomagnets. (a) Holes are formed in photoresist by IL. (b) The holes are transferred into the thin oxide, and, subsequently into the ARC layer. (c) A cross section of the sample after electroplating reveals Ni posts embedded in the ARC template.

sibility of achieving out-of-plane anisotropy in CoP particles [61]. This thesis will focus on the plated Ni samples that we have fabricated and characterized, since our work with other materials is still in progress. Material for plating Ni such as the Ni anode and sulfamate solution was purchased from MacDermid Inc., a specialty chemical company (www.macdermid.com). Plating proceeds galvanostatically. The height of the plated structures is controlled with plating time. Ni is plated at a temperature of 50°C with a current density of 8 mA/cm^2. These conditions are said to minimize stress [63]. In addition, boric acid is used to maintain solution pH between 3 and 4. The solution is agitated at 100 rpm during plating using a magnetic stir bar.

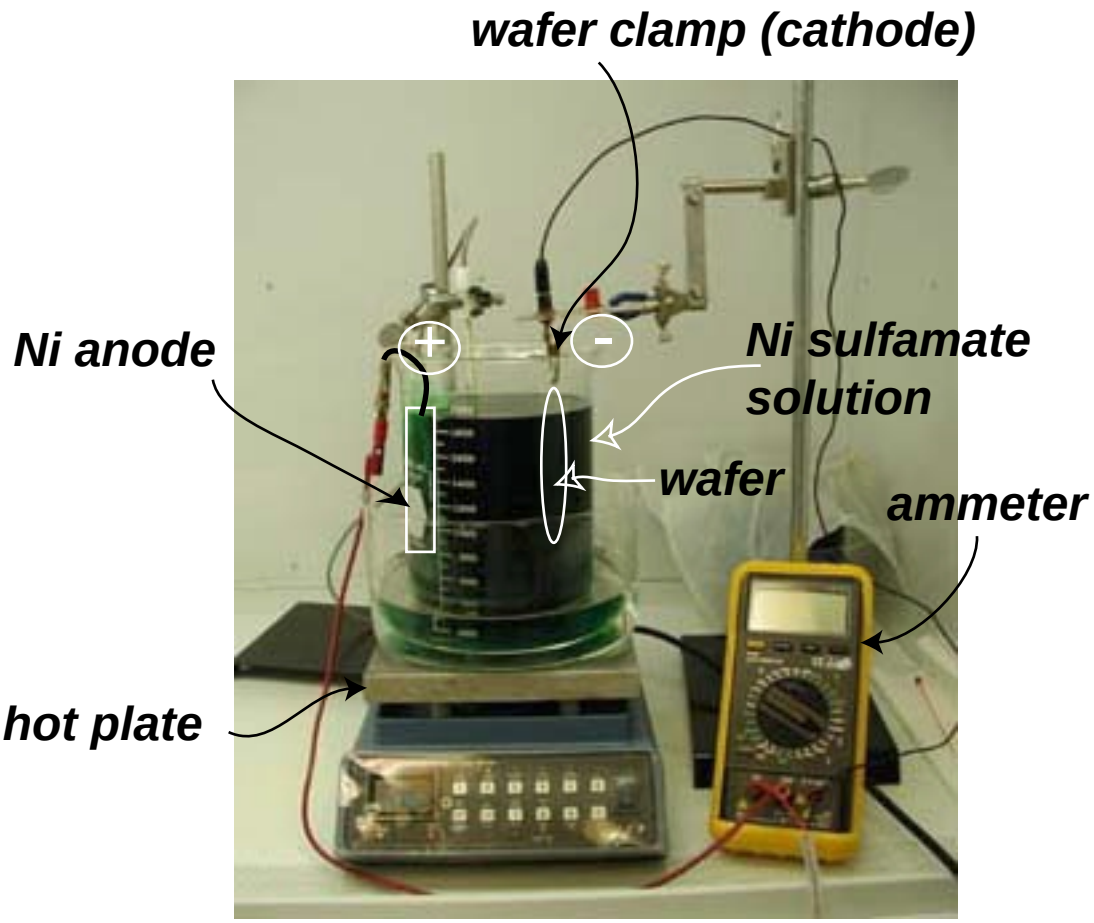

Figure 3.9 The Ni electroplating set-up in the Space Nanostructures Laboratory. The Ni anode is attached with hooks to the side of the beaker. The positive electrode of the power supply (not shown) is connected with alligator clips to the anode hook. The wafer is clamped with an alligator clip that is connected to the cathode of the power supply.

In addition to the sulfamate Ni and boric acid, this commercially available solution contains other proprietary additives that act as anode corrosion aids and an anti-pit agents. As a result of the many ‘contaminants’ in solution, the Ni plate forms fine, equiaxial grains. High voltage transmission-electron microscopy (TEM) was used to image Ni particles that were scraped onto a carbon grid. The particles were electron transparent at 400 kV and could be imaged without thinning. From TEM, we estimate the size of a Ni grain to be on the order of 20 nm (Fig. 3.10). All TEM work reported here was performed by Dr. F. M. Ross at IBM, Yorktown Heights. Data from x-ray diffraction analysis show plated Ni films to have a <111> out-of-plane texture. Since Ni has weak crystal anisotropy, and since the plate is a polycrystal, the magnetic easy axis of electroplated pillars is influenced mostly by shape. For a constant pillar diameter, we vary the height to study the dependence of magnetic anisotropy on aspect ratio. Data from this study will be presented in the next chapter.

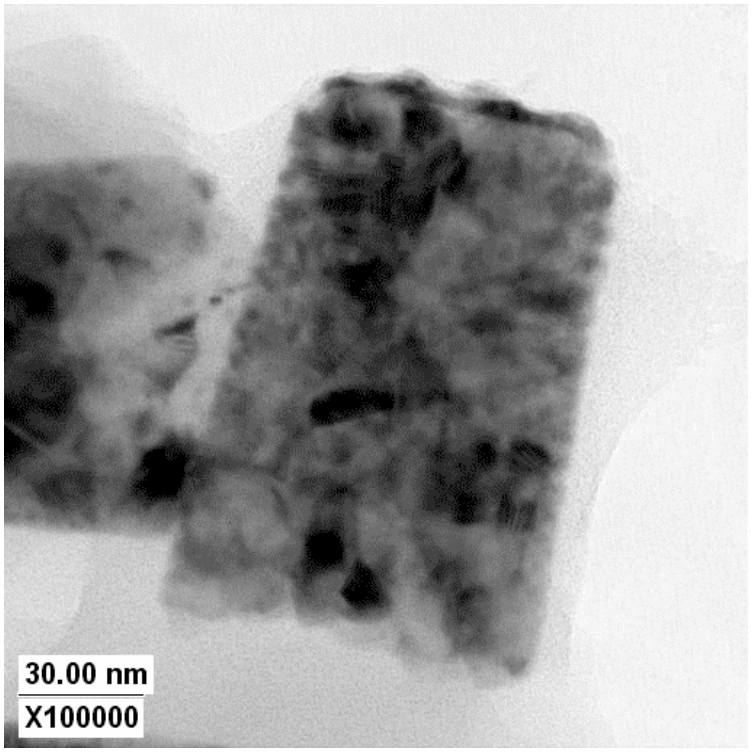

Figure 3.10 Transmission electron micrograph of an electroplated Ni post (shown up-side-down). The image was obtained by passing energetic electrons through the entire Ni post.

To perform bulk characterization of an array of electroplated Ni pillars, we need not remove the plating template. However, the magnetic pillars may be characterized individually using a magnetic scanning probe. To facilitate such experiments, the plating template of ARC may be dissolved in an appropriate solution (such as H_2O:H_2O_2:NH_4OH), or the SiO_2 mask and ARC template may be reactive ion etched by CHF_3 and O_2 respectively.

3.3.2 Evaporation/Lift-off

In a simpler process, the ferromagnetic material may be deposited into the template by evaporation. This process does not require a plating-base-coated substrate. Evaporation is well suited for producing shallow magnetic structures of aspect-ratio (height-to-base diameter ratio) close to, or less than 1. Often, extreme topography in magnetic storage media present challenging tribology problems to read/write heads flying less than 40 nm above the substrate [2]. The evaporation of material into a template of holes produces conical and truncated-cone shapes.

The main steps of the evaporation process are demonstrated in the SEMs of Fig. 3.11. Once again, holes in photoresist are transferred via reactive ion etching into the SiO_2 and ARC layers. Ni and Co films are electron-beam evaporated into the template of holes at a base pressure of approximately $5 \cdot 10^{-6}$ Torr and a deposition rate of 5 Å/s. The evaporation template and excess metal on top is removed in a H_20:H_2O_2:NH_4OH solution (the so-called RCA cleaning solution [45]).

We have used this process to fabricate arrays of Co and Ni nanomagnets with a variety of aspect ratios. The diameter of the template holes may be controlled by changing the exposure dose. Therefore, we can perform studies of particles of a fixed height and varying base diameter. Similarly, we can change the height of a particle by changing the thickness of the evaporated film.

The evaporated films are polycrystalline. Transmission electron micrographs of evaporated Ni particles were obtained in the same way as for electroplated particles (Fig. 3.12). The Ni particles have a columnar grain structure with the grains often extending through the film thickness, and grain diameters of 10-20 nm. A 3-5 nm oxide layer coats the sides of the nano-

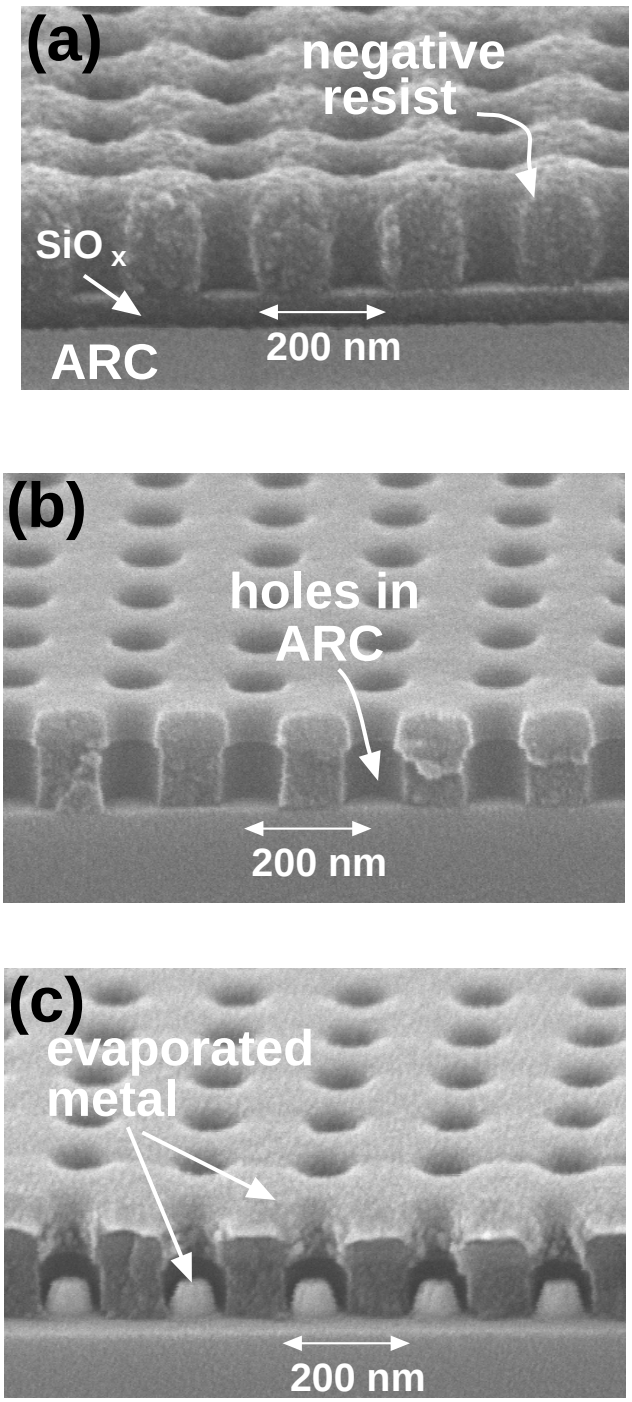

Figure 3.11 Scanning electron micrographs of major steps in an evaporation/lift-off process. (a) The micrograph portrays holes in photoresist formed by interference lithography. (b) The holes are transferred by reactive ion etching into the underlying oxide and ARC. (c) A ferromagnetic material is evaporated onto the template of holes. Excess magnetic material may be removed by dissolving the evaporation template.

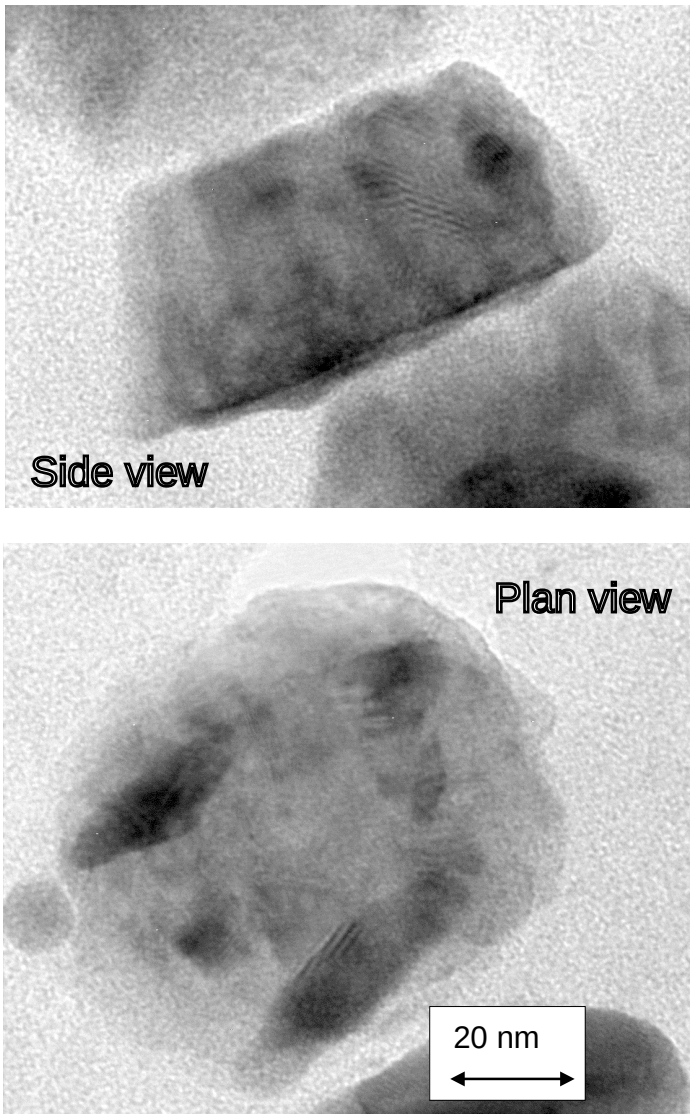

Figure 3.12 Transmission electron micrographs of an evaporated Ni particle. (a) This micrograph was obtained with a cross sectional perspective. (b) Here, the Ni particle is imaged from a top view.

structure that are not in contact with the substrate. X-ray diffraction shows that the Ni films have a preferred (111) texture, while the cobalt has a strong preferred (0002) texture. We estimated the c-axes in the Co to posses a distribution within a 13º half-angle from the normal to the substrate [30].

3.3.3 Etching Process

The etching process may be the only method for patterning the magnetic elements of an MRAM array [31]. An interdisciplinary effort is currently underway in our laboratory to

develop the smallest MRAM device in the world [46]. For completeness, Appendix F in this thesis details an early feasibility study for patterning a Cu/Co-multilayer thin film into isolated islands via ion milling.

CHAPTER 4: CHARACTERIZATION

4.1 Bulk Characterization: Vibrating Sample Magnetometry (VSM)

The magnetism of materials is revealed in their hysteresis loops. A hysteresis loop is the mapping of material magnetization to an externally applied magnetic field. Magnetic characterization of a particle or ensemble of particles involves generating a hysteresis loop.

Hysteresis loops are generated by magnetometers that sense the magnetic moment of a sample. The sensitivity of a vibrating sample magnetometer (VSM) is order of 10^{-8} Am^2 (10^{-5} emu). Our laboratory houses such an instrument. The moment of a typical isolated nanomagnet is order of 10^{-16} Am^2 (10^{-13} emu)*. The nanomagnets presented in this thesis sit on a 200 nm period cartesian grid. Therefore, a sample that is 2 mm on the side will provide the minimum required signal. Thus, we obtain hysteresis loops for 'large-area' samples. A superconducting quantum interference device (SQUID) is a magnetometer that affords two-orders-of magnitude of increased sensitivity. However, the magnetic sensor in a SQUID must be cryogenically cooled [64]. Furthermore, sample mounting in a SQUID is slightly more difficult than for VSM, and the measurement time is much longer.

A hysteresis loop of a sample yields a variety of information including: net magnetic moment, coercivity, remanence, magnetic anisotropy, as well as insight into switching mechanisms of the individual particles that make up the array. Since we are measuring the loop of

* calculation is based on a 100 nm-Ni cube

samples that contain about a billion nanomagnets, the bulk behavior observed from a hysteresis loop may be compared to simulations of hysteresis which assume a particular switching mechanism and distribution of switching fields of the individual nanomagnets.

4.1.1 VSM Principles of Operation

Figure 4.1 is a schematic of a vibrating sample magnetometer (VSM) set-up. The magnetic sample is attached to glass rod. The rod is vibrated at ~ 70 Hz in the vicinity of the detection coils. The detection of the sample's magnetic moment is based on a single principle derived from the Farraday law of induction, namely that a potential drop is induced across the pick-up coils due to a change of flux linked by the coils:

$$V_{IND} = -N\frac{d\phi}{dt} \tag{4.1}$$

where N is the number of turns in the detection coils and ϕ is the flux linked in the coils. The changing flux, ϕ, is proportional to M, the sample's magnetization. Therefore, the induced voltage is a function of M. A giant electromagnet generates a uniform field H_M between the pole tips of the magnet depicted in Fig. 4.1. H_M magnetizes the sample. If H_M is swept slowly, the coils measure the moment of the sample in the direction of the external field for each value

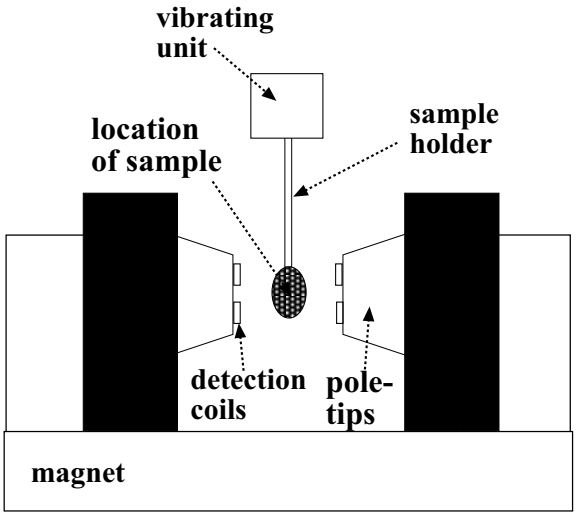

Figure 4.1 A schematic of a vibrating sample magnetometer.

of the external field. Plotting the measured moment as a function of H_M generates a hysteresis loop.

4.2 Electroplated Samples

4.2.1 Sample Discussion

Electroplated samples are cylindrical with a diameter equal to the diameter of the holes in the ARC plating mold and a height determined by the thickness of the plate. To study the behavior of plated Ni samples as a function of aspect-ratio (AR= ratio of the height of the particles to its diameter), we plated the 4 samples shown in Fig. 4.2. The SEMs of each sample are on the left hand side of the figure while the corresponding hysteresis loops, obtained with VSM, for each sample are on the right-hand-side. Sample P1 is shown before the removal of the ARC plating mold. Since the plating mold is not magnetic, it need not be removed before VSM characterization. The attributes of each sample are summarized in Table 4.1.

Sample P0 saturates faster when the applied field is parallel to the plane of the substrate. Therefore, its easy axis is parallel to the substrate. Since this sample revealed a very small remanence and coercivity in both directions, and since its smallest dimension is $9\lambda_{ex}$, we do not expect the individual nanomagnets to be single domain. Therefore, the sample is unsuitable for data storage.

The other three samples (P1, P2, and P3) have dimensions that are several λ_{ex}. To first order, we expect their behavior to be dictated by their shape, since plated Ni samples are polycrystalline with weak <111> texture. In other words, particles with an AR > 1 are expected to be magnetized perpendicular to the plane, and particles with AR < 1 are expected to be magnetized parallel to the plane. Sample P1, with AR=0.73, does indeed have an in-plane easy axis. However, unlike sample P0, the in-plane remanence appears high, leading us to conclude that the nanomagnets are in plane dipoles. The small in-plane coercivity is consistent with all in-plane directions being easy directions of magnetization. Ideally, the in-plane coercivity would be exactly zero; the presence of pinning sites gives rise to non-zero coercivity. Samples P2 (AR=1.4) and P3 (AR=2.4) have an easy axis of magnetization perpendicular to the sub-

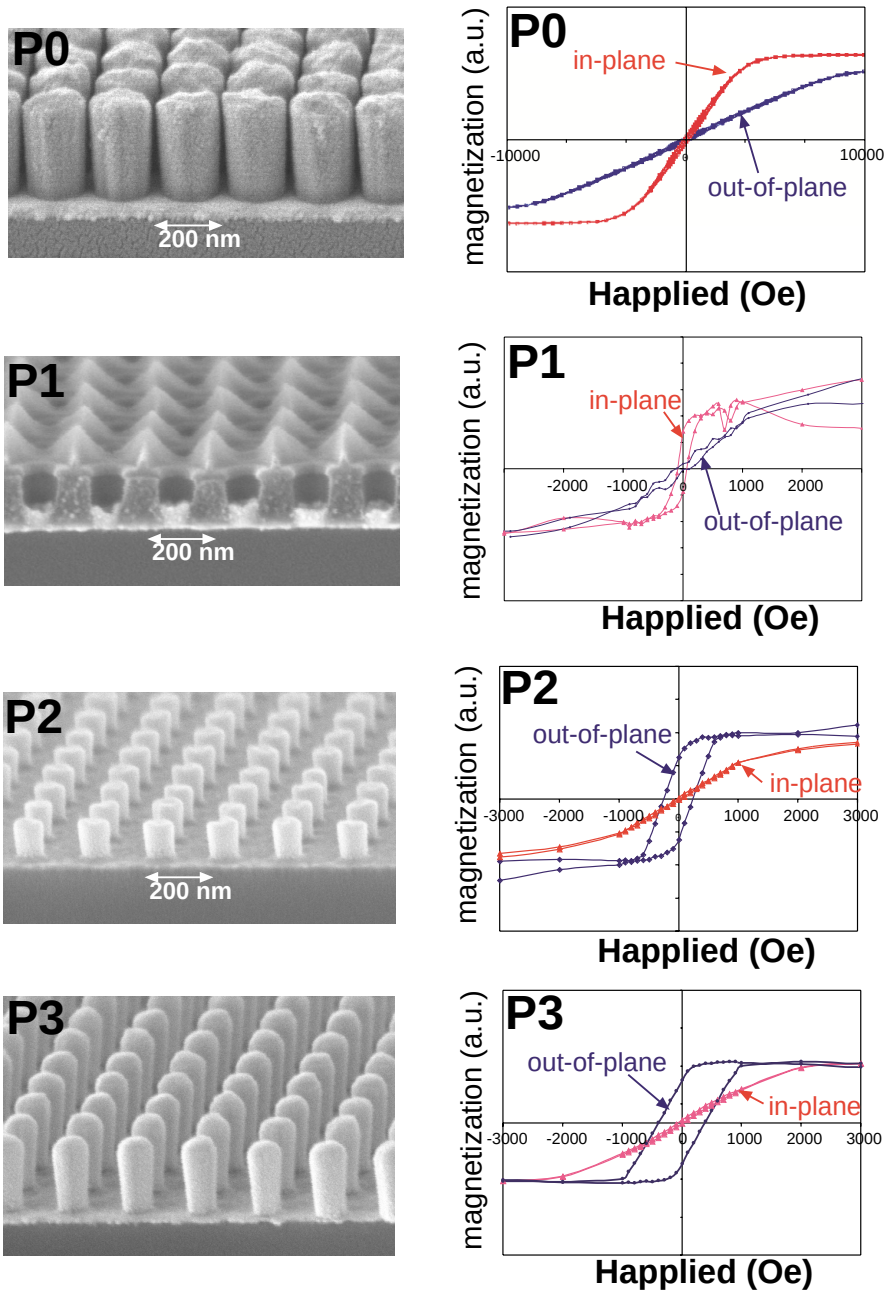

Figure 4.2 Scanning electron micrographs (left) and corresponding hysteresis loops (left) of electroplated Ni samples.

1	2	3	4	5	6
Sample Name	**Height 'h' (nm)**	**Diameter 'd' (nm)**	**Aspect ratio AR=h/d**	**Moment of a nanomagnet (emu)**	**Squareness (out-of-plane)**
P0	300	180	1.7	$2.2\cdot 10^{-12}$	~0
P1	70	95	0.73	$1.4\cdot 10^{-13}$	6%
P2	125	90	1.4	$2.3\cdot 10^{-13}$	66%
P3	220	90	2.4	$4\cdot 10^{-13}$	70%
7	**8**	**9**	**10**	**11**	**12**
Sample Name	**Easy-axis**	**H_c in-plane (Oe)**	**H_c out-of-plane (Oe)**	**H_i^* (Oe)**	**$9\cdot H_i$ (Oe/Am^{-1})**
P0	In-plane	100		276	~2500
P1	In-plane	110	44	18	162
P2	Out-of-plane	27	240	28	252
P3	Out-of-plane	46	392	50	450

* computed assuming uniform magnetization perpendicular to the plane

Table 4.1: Physical and magnetic characteristics of the electroplated Ni samples shown in Figure 4.2.

strate, and hard axes parallel to the substrate. In fact, the hysteresis loops of samples P2 and P3 are consistent with an array of single-domain particles [65]. Furthermore, magnetic force imaging of the nanomagnets in sample P3 confirm this observation (these images will be presented in following sections). Similar imaging of sample P0 performed at the University of Minnesota does not reveal a field due to a single-domain particle. The shear in the loops of samples P2 and P3 can be attributed to magnetostatic interactions and a spread in the switching fields of the individual nanomagnets, as discussed in the next section. Samples P2 and P3 have fairly large remanence: 66% in the case of P2 and 70% in the case of P3. At first glance, these two samples appear suitable for storage. Upon further investigation, we find that the magnetostatic field affecting each particle due to the magnetization of its neighbor is too high.

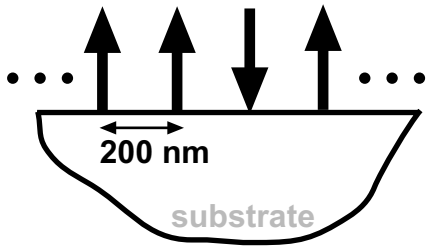

Figure 4.3 Illustration of magnetic dipoles perpendicular to the plane of the substrate.

4.2.2 Interactions

To quantify magnetostatic interactions of samples with out-of-plane easy axis, we approximate the nanomagnets by dipoles that point into and out of the plane, as shown in Figure 4.3. The assigned moment, m, of each dipole is equal to the moment of a single nanomagnet, computed in column 5 of Table 4.1. From VSM, we measure the moment of electroplated Ni to be 60% that of pure Ni. We assume the lower magnetization of electroplated Ni is due to the co-deposition of non-magnetic material. We estimate the field of a dipole at a distance r away from the center of the dipole using the following coordinate-free dipole field [66]:

$$\bar{H}_i = \frac{1}{4\pi r^3}\left[3(\bar{m}\cdot\bar{a}_r)\bar{a}_r - \bar{m}\right], \tag{4.2}$$

where $\bar{a}_r$ is the unit vector of the vector $\bar{r}$ from a dipole to its nearest neighbor. For all our samples, r=200 nm. We calculate the nearest neighbor field H_i to be 28 Oe and 50 Oe in samples P2 and P3 respectively. Suppose all the nanomagnets in sample P3 are magnetized up. According to reference [67], any one nanomagnet in the sample will experience a total downward field of $9\cdot H_i$ due to all the nanomagnets in the array. We compute this maximum neighbor field in column 12 of Table 4.1. Since we approximate the nanomagnets by magnetostatically interacting dipoles, the coercivity of each sample is equivalent to the average switching field associated with each nanomagnet. To estimate the level of magnetostatic interactions among the nearest neighbors in a sample, we compare $9\cdot H_i$ to the coercivity, H_c, of the sample. In both samples P2 and P3, $9\cdot H_i > H_c$, indicating strong interactions among the

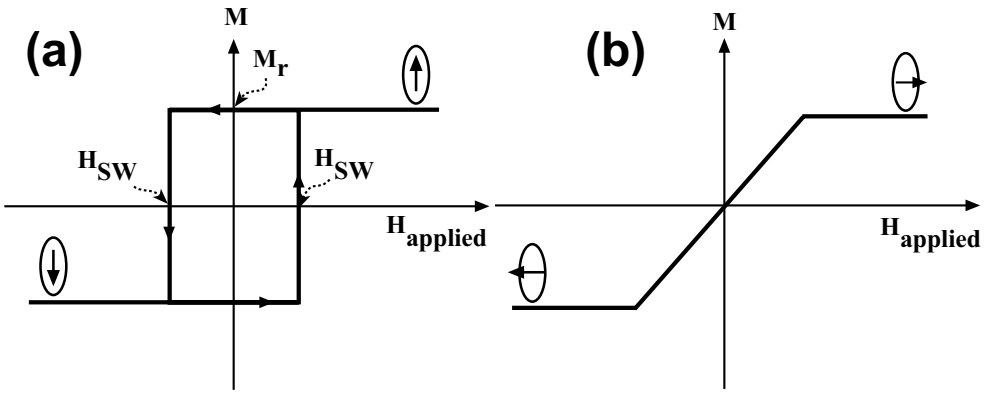

Figure 4.4 Hysteresis loops of a single domain, uniaxial magnetic particle. (a) The external field is applied along the easy axis of magnetization. (b) The external field is applied perpendicular to the easy axis of the particle.

neighbors. Strong magnetostatic interactions lead to instability in the magnetization patterns, thus making the samples unsuitable for data storage.

4.2.3 Modelling Hysteresis in Electroplated Ni

We have modeled the nanomagnets in sample P3 as magnetostatically interacting dipoles. The out-of-plane hysteresis loop of an individual dipole has the 'square' shape depicted in Fig. 4.4 characteristic of a single-domain particle with 2 stable states. The dipole switches directions whenever the external field exceeds the dipole's switching field, H_{sw}. If all the nanomagnets in an array had identical switching fields and did not interact magnetostatically, the collective loop would look identical to the loop of a single particle. The loop of sample P3 appears as a sheared square. As stated previously, the two factors which contribute to the shear are magnetostatic interactions between the particles, and a distribution of the switching fields of the particles in an array. Next, we examine the distortion from a perfect square that each of these phenomena produces in a hysteresis loop.

A computer routine was written (by M. Hwang) in MATLAB® to simulate the hysteresis loop of an array of magnetostatically-interacting dipoles. The switching fields of the dipoles are assumed to have a Gaussian distribution [65]. The Gaussian's mean is assigned as the out-of-plane coercivity of the sample. The strength of the magnetostatic interactions is determined as explained previously. Reference [65] describes the algorithm used by the simu-

lation. The only free parameter available to us is the standard deviation, σ_{SW}, of the switching field Gaussian. We use this model to fit a simulated hysteresis loop to the out-of-plane loop of sample P3.

Sample P3 has an out-of-plane coercivity H_c=392 Oe. First, we consider the case where the magnetostatic interactions in the array are weak, though this case is unrealistic considering the magnetic volume and the packing density of the particles in sample P3. We simulate an array of 12x12 dipoles, assuming the magnetization of each dipole is equal to 30% of the magnetization of pure Ni. We generate loops for σ_{SW} = 10, 150, and 200 Oe. The results are shown in Fig. 4.5a. Since the interactions are weak, the standard deviation must be made greater than 200 Oe to shear the loop by the required amount. An array of non-interacting dipoles can only produce loops where the ratio of the magnetization at remanence to the saturation magnetization (i.e. the loop squareness) is equal to 1, regardless of σ_{SW}.

Next, we consider the case of a small standard deviation σ_{SW} = 10 (Figure 4.5b). We generate loops for two cases: (1) the magnetization is 60% that of pure Ni as in the case of sample P3, and (2) a magnetization characteristic of 100% pure Ni. We observe that a small standard deviation generates sheared squares with sharp corners. Increasing the strength of the magnetostatic interactions increases the slope but does not give rise to the S-shape observed in our data. From case (1), we determine the contribution of magnetostatic interactions to shear in sample P3's hysteresis loop. The rest of the distortion from a perfect square must be due to a larger σ_{SW}.

Finally, we set the moment of the dipoles in the simulation equal to sample P3, and we increase σ_{SW} such that we are able to fit the data. Figure 4.5c plots simulations for σ_{SW} = 100, 150, and 200 Oe. We obtain the best fit to our data when σ_{SW} = 150 Oe. It appears from the simulations that the slopes of the S-shaped loop are caused by the interactions which reduce the remanence from 1, while the rounding of the corners is caused by the spread in the switching fields of the nanomagnets in the sample.

The results of the simulations are summarized qualitatively in Fig. 4.6. Basically, the magnetostatic interactions produce a slope in the loop proportional to $M_s/9 \cdot H_i$. The rounding of the corners may be fit by adjusting the spread of switching fields, σ_{SW}.

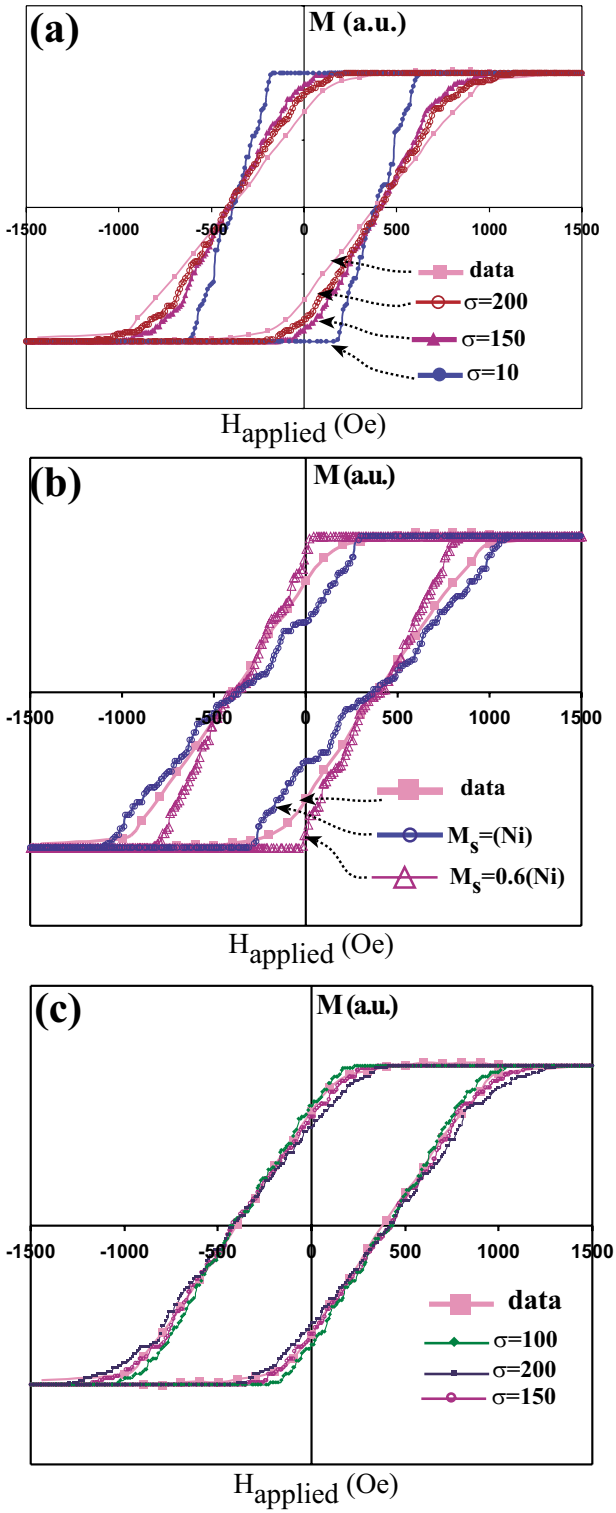

Figure 4.5 Comparison of simulated hysteresis loops of an array of magnetostatically interacting dipoles to the hysteresis loop of sample P3. (a) The simulation assumes that the magnetostatic interaction field is weak for a variety of switching field distributions (b) The first simulation where $M_s=0.6 \cdot M_{sNi}$ assumes a realistic magnetostatic field and a very narrow spread in the nanomagnet switching field, while the second simulation ($M_s=M_{sNi}$) assumes large magnetostatic interactions field and a narrow spread of switching field. (c) Simulation of a realistic case for sample P3.

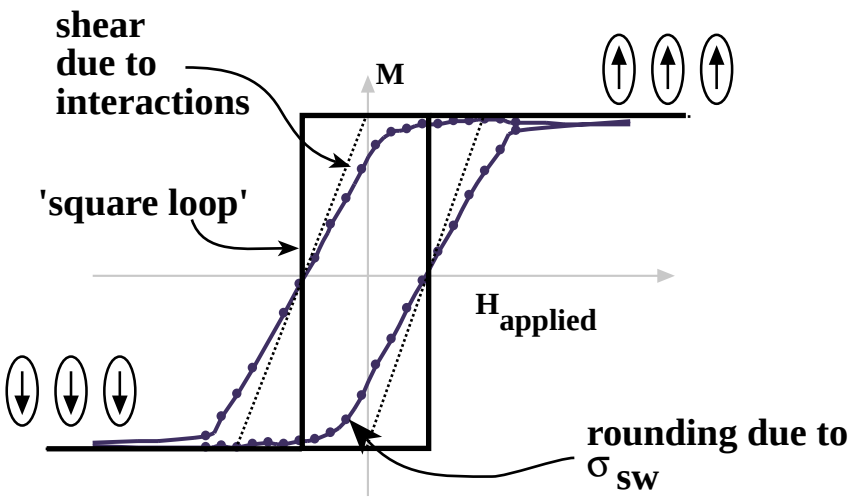

Figure 4.6 Illustration of the effect of magnetostatic interactions and spread in switching fields of an array of dipoles on a collective hysteresis loop.

Since the fit between simulation and data is excellent, we conclude that our sample may be represented by an array of magnetostatically interacting dipoles whose strength is given by the geometry of the nanomagnets. The accuracy of our fitting parameter, σ_{SW}, may be verified with magnetic force microscopy (MFM) experiments, as explained in the following sections.

Sample P3 is unsuitable for data storage on account of the large magnetostatic interaction field experienced by each nanomagnet due to its neighbors. Interestingly, 75% of the magnetostatic field is due to the neighbors in the first 2 nearest shells (see Fig. 4.7). To reduce magnetostatic interactions, we can increase the distance separating the nanomagnets. This solution is not very interesting since it implies reducing the areal density. Otherwise, we can reduce the magnetic volume of the particle while maintaining its aspect ratio and array pitch. This may perhaps be achieved by oxidizing the Ni posts, or fabricating posts with a lower M_s material.

4.3 Evaporated Samples

A large number of Ni and Co samples were fabricated via the evaporation/lift-off process. SEMs and corresponding hysteresis loops for samples of evaporated Ni are shown in Fig.

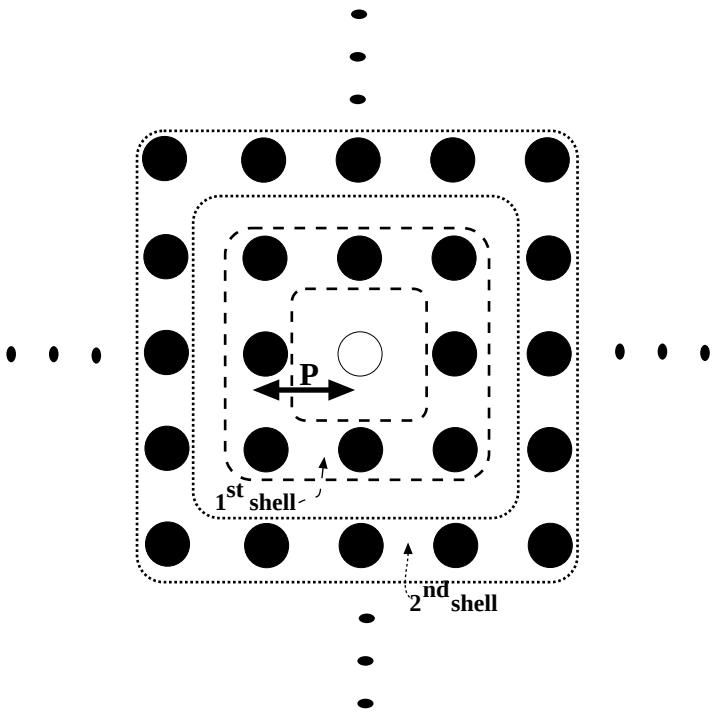

Figure 4.7 A top view of a square array of nanomagnets illustrating the first- and second-neighbor shells of the particle in the center of the array.

4.8, in order of increasing aspect-ratio. All samples have a pitch of 200 nm. In the case of these conical and truncated-cone particles, aspect-ratio (AR) is defined as the ratio of the particle height-to-base diameter. The aspect-ratio of the particles was varied by varying the exposure dose and/or the thickness of the evaporant. SEMs of evaporated Co particles and corresponding hysteresis loops are shown in Fig. 4.9. Table 4.2 lists physical and magnetic properties of the Ni and Co samples.

4.3.1 Observations

For both Ni and Co, a change in net anisotropy occurs for aspect ratios AR of 0.65. For particles with AR > 0.65, the out-of-plane direction is an easy axis with coercivity of up to 600 Oe for the tallest particles (AR = 1.2), while the in-plane direction is a hard axis. For flat particles, with AR < 0.65, there is an easy plane parallel to the base of the particle. The out-of-plane direction is a hard axis. Since these particles all have cylindrical symmetry, zero in-plane coercivity would be expected. However, in-plane coercivities of 30 – 70 Oe for Ni and

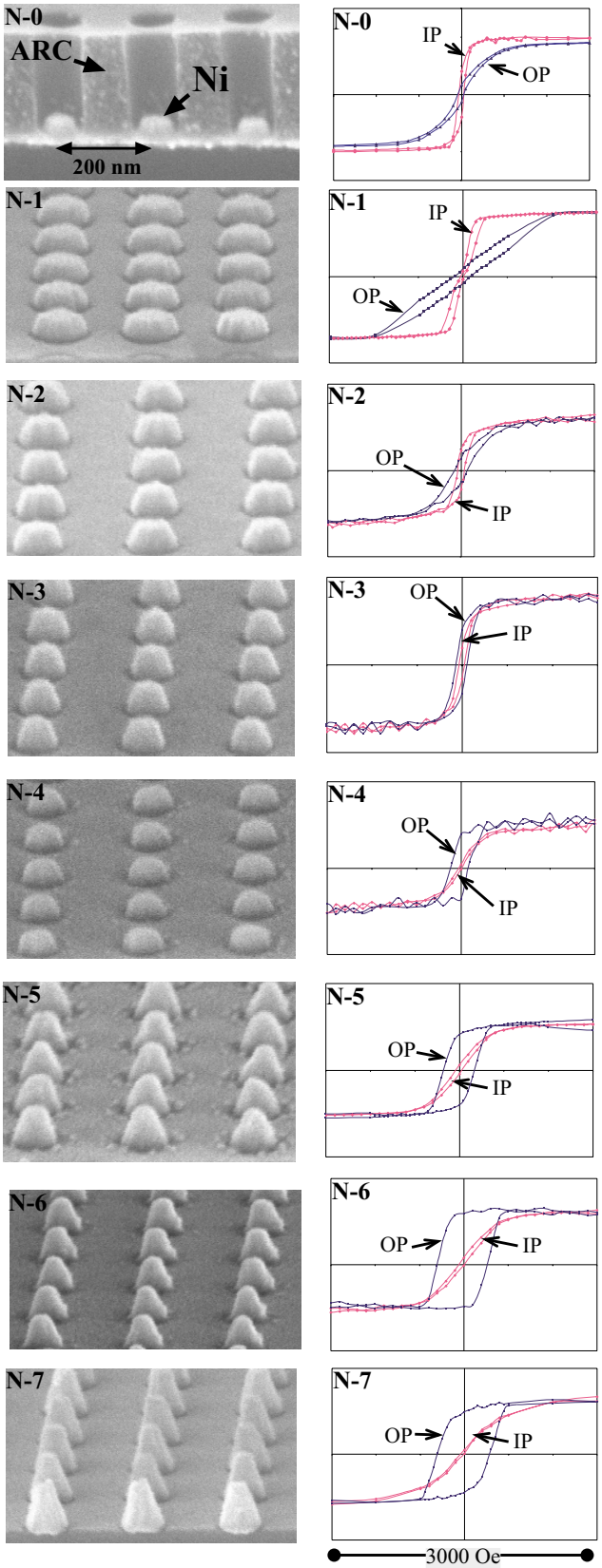

Figure 4.8 Scanning electron micrographs and corresponding hysteresis loops of evaporated Ni samples.

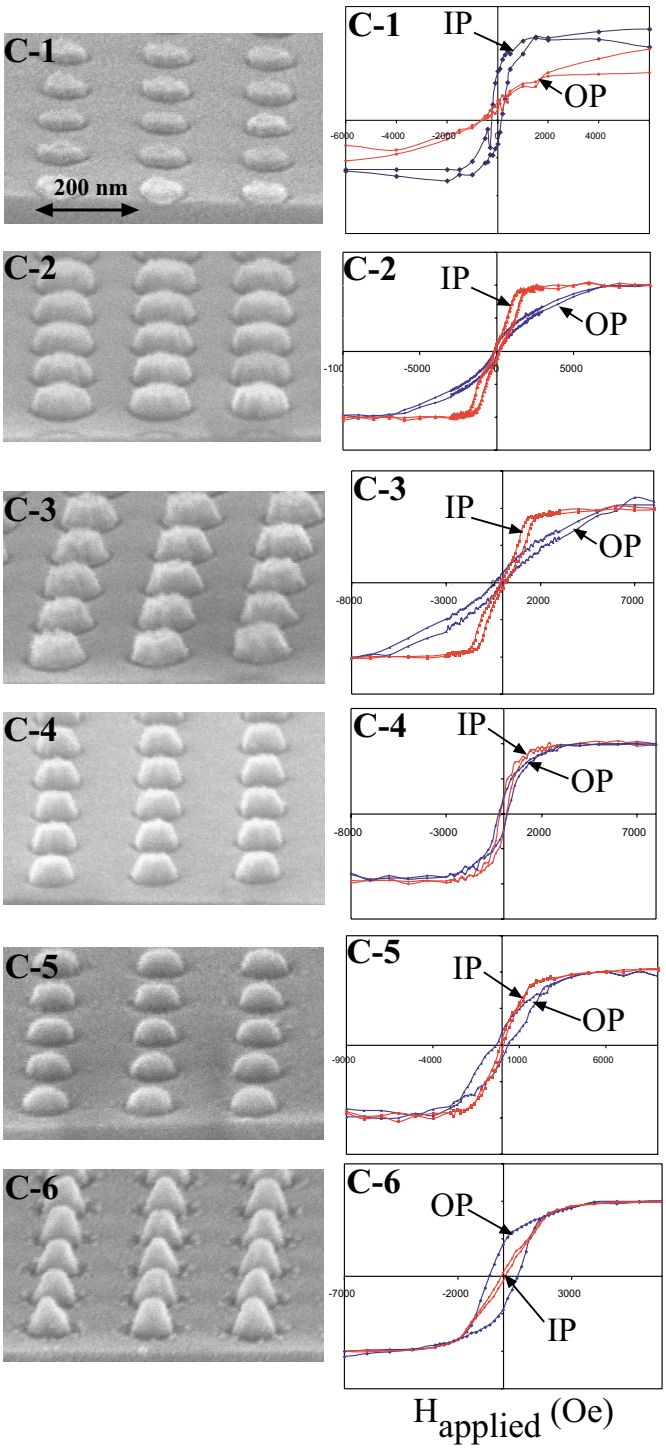

Figure 4.9 Scanning electron micrographs and corresponding hysteresis loops of evaporated Co particles.

90 – 220 Oe for Co are observed, indicating pinning of the magnetization as it rotates in plane, perhaps due to edge irregularities or other microstructural features [30].

Interestingly, not all hysteresis loops of the particles with out-of-plane easy axis conform to the sheared square model of the electroplated Ni particles. Rather, they resemble the hypothetical loops of particles with a flower like magnetization configuration (Fig. 2.4b). This observation is consistent with the dimensions of these particles (several λ_{ex}). The only way to determine the remanence magnetization configuration of these particles is via micromagnetic simulations. In reference [30], we report on the results of micromagnetic simulations of truncated cone particles, and compare the results to our experimental observations. The following section, which summarizes our findings, follows ref. [30] closely.

Sample	Height *h* (nm)	Base *b* (nm)	Top *a* (nm)	Aspect ratio a.r. = *h/b*	Coercivity in plane (Oe)	Coercivity out of plane (Oe)	Nearest neighbor field H_i (Oe)
N-0	35	80	57	0.43	60	60	8
N-1	55	122	107	0.45	42	179	34
N-2	55	89	50	0.62	77	145	13
N-3	55	84	60	0.65	59	118	14
N-4	55	75	45	0.73	32	201	10
N-5	80	89	36	0.90	69	347	16
N-6	80	80	36	1.00	61	560	13
N-7	110	91	37	1.21	35	586	23
C-1	20	95	76	0.22	220	100	20
C-2	55	125	90	0.44	162	136	89
C-3	55	123	85	0.45	130	227	84
C-4	55	86	85	0.64	168	223	56
C-5	55	79	50	0.70	91	340	32
C-6	80	85	32	0.94	87	620	41

Table 4.2: Physical and magnetic characteristics of evaporated Ni and Co samples shown in Fig. 4.8 and 4.9 respectively.

4.3.2 Micromagnetic Simulations of Conical Nanomagnets

As stated previously, the evaporated particles presented in this thesis are too small to form domain walls. However, their dimensions and non-ellipsoidal shape prevent the stability of a single-domain with $\nabla \cdot \overline{M}=0$.

The micromagnetic simulations of reference [30] confirm that the magnetization configuration of truncated cones with dimensions from $2\lambda_{ex}$ to $10\lambda_{ex}$ resemble qualitatively the illustration of Fig. 2.4b. In fact, for small diameters, the particle has a remanence close to the saturation magnetization and the magnetization remains parallel to its axis, with small deviations at the top and bottom surfaces (Fig. 4.10a). This will be called a 'flower' state, after similar magnetization patterns calculated for prismatic and cubic particles [21]. However, as the diameter increases past $3\lambda_{ex}$ the axial remanence begins to drop as a magnetization vortex develops along the central axis of the particle and the magnetization at the perimeter becomes tilted into the sample plane (Fig. 4.10b). The tilt develops first near the base of the particle, where the magnetization forms a helical structure; as the particle size increases, the magnetization lies closer to the base plane and the axial remanence decreases monotonically. At diameters of $12\lambda_{ex}$, the particle forms multiple domains and the axial remanence is close to zero.

The exact dimension of transition from flower to vortex depends on the particle aspect ratio and the perpendicular anisotropy. For example, a strong out-of-plane anisotropy will stabilize the flower state for dimensions greater than $4\lambda_{ex}$ in Co particles [30].

Columns 4 and 7 of Table 4.3 show a comparison between experimental and calculated remanence (expressed as a ratio) for each sample. These results were obtained by M. Hwang using the micromagnetic simulators developed by M. Redjdal at Boston University [44]. The dimensions of the model were adjusted to fit the measured particle dimensions as closely as possible. A comparison between experimental and calculated remanence data for nickel particles reveals that the general trend in axial remanence is followed well, with an increase in remanence through the series as AR increases and b decreases. However, the measured remanence values are higher than the model values by as much as 20%. We believe this to be due to the presence of out-of-plane anisotropy in the nickel, which stabilizes the magnetization paral-

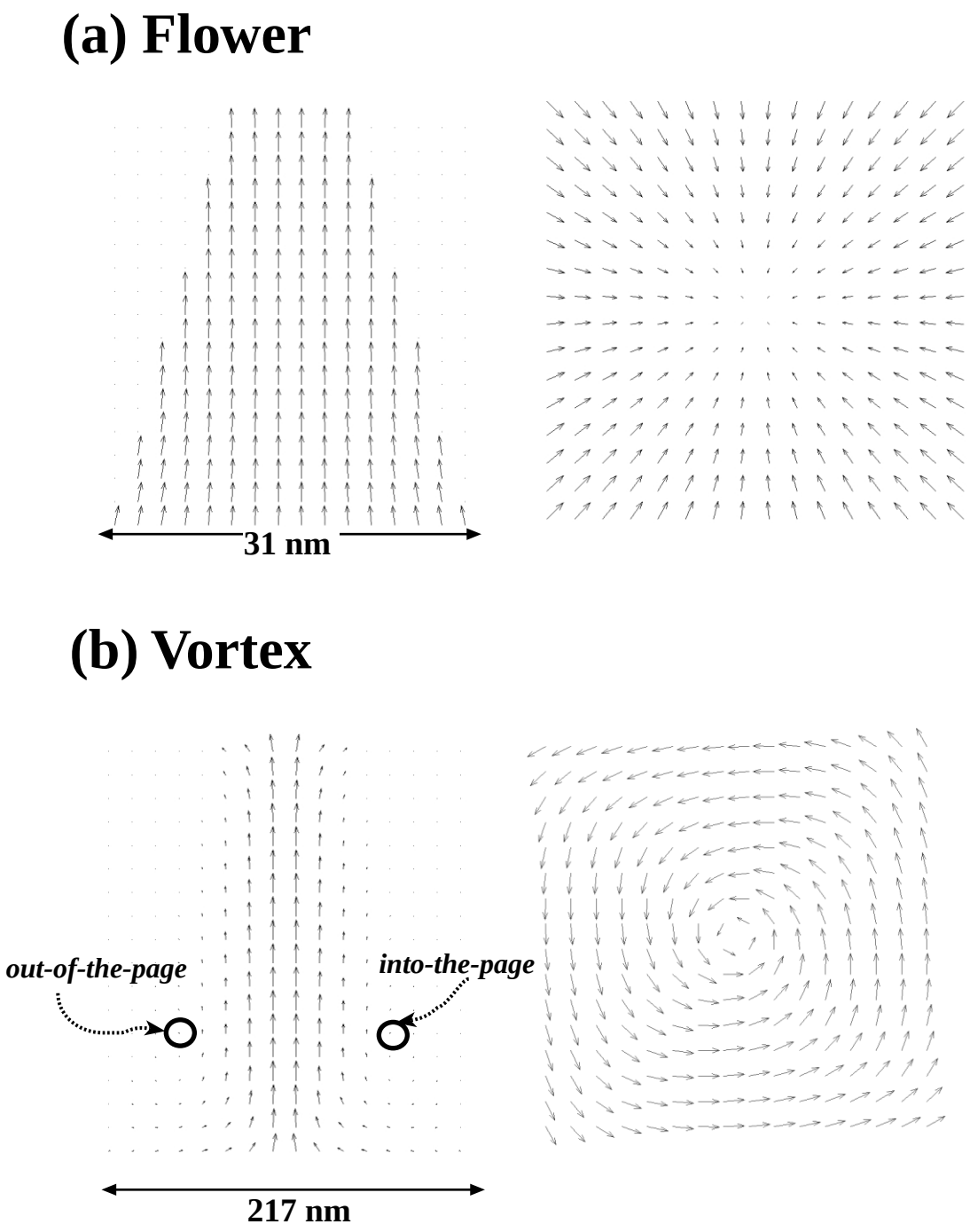

Figure 4.10 (a) The center longitudinal cross section of the flower state (left) and the projection of the magnetization on the bottom plane (right). The diameter is $1.6\lambda_{ex}$. (b) The center longitudinal cross section of the vortex state where the diameter is equal to $10.9\lambda_{ex}$ [30].

	Experimental			Model					
1	**2**	**3**	**4**	**5**	**6**	**7**	**8**	**9**	**10**
Sample	*b* (nm)	*h/b*	M_z/M_s	*b* (nm)	*h/b*	M_z/M_s for $K_z=0$	M_z/M_s for $K_z= 5\ 10^4$ erg cm^{-3}	M_z/M_s for $K_z= 2\ 10^5$ erg cm^{-3}	M_z/M_s for $K_z=2.7\ 10^6$ erg cm^{-3}
N-1	122	0.45	0.12	121	0.45	0.08	0.08	1.18	
N-2	89	0.62	0.22	89	0.61	0.28	0.32	0.56	
N-3	84	0.65	0.40	84	0.65	0.36	0.42	0.72	
N-4	75	0.73	0.65	75	0.74	0.62	0.70	0.91	
N-5	89	0.90	0.79	89	0.90	0.60	0.67	0.83	
N-6	80	1.00	0.87	80	1.00	0.72	0.77	0.91	
N-7	91	1.21	0.81	90	1.22	0.63	0.67	0.81	
C-4	86	0.64	0.21	86	0.65	0.00			0.08
C-5	79	0.70	0.17	79	0.71	0.00			0.33
C-6	85	0.94	0.40	85	0.94	0.00			0.68

Table 4.3: The simulated ratio of the remanence to the saturation magnetization of evaporated Ni and Co samples for a variety of anisotropy conditions.

lel to the particle axis and raises the remanence. The preference of the [111] crystal axes for orientation perpendicular to the plane contributes to this behavior. However, the anisotropy introduced by the weak texture must be smaller than the magnetocrystalline anisotropy of nickel. Column 8 shows the effects of axial anisotropy of $5 \cdot 10^4$ erg/cm^3, which increases the remanence by up to ~15% depending on aspect-ratio. Furthermore, if we account for the anisotropy introduced by the columnar microstructure of evaporated grains (Column 9), we increase the remanence beyond what is measured.

Cobalt particles are expected to behave quite differently from nickel particles of the same size because the exchange length of cobalt is smaller. The 85 nm diameter Co particles correspond to $12\lambda_{ex}$; the micromagnetic model predicts the existence of multiple domains, and negligible remanence within particles of this size. Experimentally, however, Co samples such as C-6 show magnetization states similar to the taller Ni samples. We believe that the strong magnetocrystalline anisotropy of the cobalt stabilizes the magnetization along the axis of the particle and increases the axial remanence. The magnetocrystalline anisotropy is due to the preferential alignment of the c-axes perpendicular to the film plane. The magnitude of this

anisotropy can be estimated from the distribution of c-axes determined by x-ray diffraction [30]. We estimate an anisotropy of $0.66K_u$, where $K_u = 4.5 \cdot 10^6$ erg/cm^3 is the uniaxial anisotropy of Co. Cobalt also has a columnar microstructure which contributes to stabilizing the axial magnetization as in the case of nickel. This effect is probably minor compared to the magnetocrystalline anisotropy. Co particles of dimensions matching samples C-4, C-5 and C-6 were also modelled (Table 4.3, column 10), with anisotropy of $0.66K_u$. Compared to experiment, the model predicts a faster increase of remanence with aspect ratio. This is probably because the amount of anisotropy may vary with grain size and shape for each particle geometry.

4.3.3 Particle Interactions

We calculate the upper bound of the strength of interactions between particles, assuming they are uniformly magnetized. The nearest-neighbor field H_i and $9 \cdot H_i$ are calculated based on a dipole approximation (Table 4.2, column 8 and 9). The saturation magnetization of evaporated Ni and Co is similar to that of pure Ni and Co. For all samples with OP easy axis, the maximum interaction field is always less than 2/3 of the samples' coercivity. Therefore, the nanomagnets in these samples are weakly interacting and appear suitable for data storage. We verify this assumption with magnetic force microscopy experiments.

4.4 Imaging the field of Individual Nanomagnets: Magnetic Force Microscopy

A magnetic force microscope (MFM) is the instrument of choice for performing microscopic magnetic characterization of individual nanomagnets. An MFM can simultaneously image sample topography and the stray magnetic fields above the surface of a sample with very high resolution, hence providing a powerful way of correlating magnetic behavior to sample geometry [68]. Also, MFM has potential application to storage read/write technology [10,69].

In this work, we use MFM to verify that the stray fields above samples with perpendicular easy axis indeed resemble the fields of single-domain particles. An MFM image of an array of particles reveals the magnetization pattern assumed by nearest neighbors, thus provid-

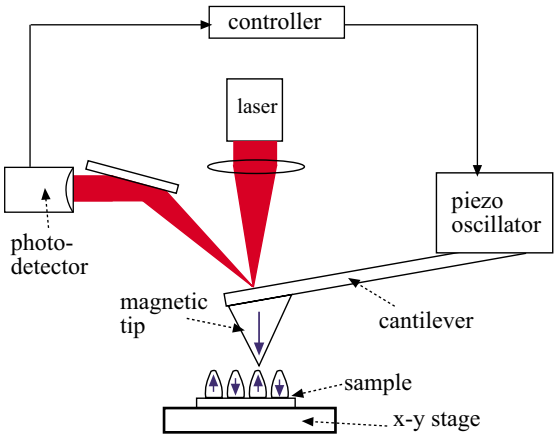

Figure 4.11 Schematic illustration of a magnetic force microscope imaging a magnetic samples. The cantilever is oscillated at a frequency that is close to its resonant frequency. Whenever the magnetic tip is at close proximity to the magnetic sample, the force between tip and sample affects a change in the dynamic properties of the cantilever. The motion of the cantilever is tracked by the photodetector that monitors a laser reflected off the back of the cantilever.

ing insight to neighbor interactions. By using MFM and an *in situ* magnet, we can measure the switching fields of the nanomagnets in a sample. In this manner, we can construct portions of hysteresis loops based on counting the number of particles in an array that switch when subject to a certain external field.

The magnetic force microscope used in this work is a Digital Instruments Nanoscope III equipped with a Dimension 3000 Scanning Probe Microscope.

4.4.1 Principles of Operation

In simple terms, a magnetic force microscope (MFM) is an atomic force microscope (AFM) with a magnetic tip (Fig. 4.11). The tip is located at the free end of a 100 to 250 μm-long cantilever. Forces on the tip due to its interaction with the sample deflect the cantilever. A deflection sensor, made up of a laser and photodetector, monitor cantilever deflection. The cantilever is scanned with piezo-scanners across the sample surface such that a map of the tip-sample interaction is produced. The tip-sample interaction may represent sample topography or sample stray fields, depending on the separation between the tip and the sample.

4.4.2 MFM Operation in Dynamic Mode

A highly sensitive approach to mapping the effect of tip-sample interactions is to take advantage of the cantilever's dynamic properties such as its resonant frequency [70,71]. This consists of driving the cantilever to oscillate near its resonance, and observing the impact of the force due to the sample on the dynamic properties of the cantilever, such as a change in frequency, amplitude and/or phase. This method is also known as the AC-detection method. For MFM measurements, the tip is scanned at greater than 20 nm above the surface where the Van der Waals forces, typically used to measure topography, have become negligible.

The AC detection method is sensitive to the gradient of the sample's force on the tip. The presence of force gradients in the direction of tip oscillation modify the effective spring constant of the cantilever according to:

$$k_{eff} = k - \frac{\partial F_z}{\partial z} \tag{4.3}$$

where k is the intrinsic spring constant and F is the force on the tip due to its interaction with the sample [69]. An attractive force on the tip acts to decrease (weaken) the effective spring constant while a repulsive force acts to increase (stiffen) the effective spring constant_that is, a force whose magnitude increases in the negative z-direction has a dF_z/dz that is greater than 0. A change in effective spring constant shifts the resonant frequency of the cantilever as follows. Let $\omega_0 = (k/m)^{-1/2}$ be the natural frequency of the cantilever and ω the effective frequency:

$$\omega = \sqrt{\frac{k_{eff}}{m}} \tag{4.4}$$

where m is the effective mass of the cantilever. Substituting equation 4.3 into the above yields:

$$\omega = \omega_0 \sqrt{1 - \frac{\left(\partial F_z / \partial z\right)}{k}} \tag{4.5}$$

If the force gradient is small relative to the spring constant k, ω can be approximated to:

$$\omega \approx \omega_0 \left(1 - \frac{1}{2k} \cdot \frac{\partial F_z}{\partial z} \right) \tag{4.6}$$

Therefore, the shift in resonant frequency of the cantilever due to the force gradient,

$\Delta\omega = \omega - \omega_0$, is now given by:

$$\Delta\omega \approx \frac{-1}{2k} \cdot \frac{\partial F_z}{\partial z} \cdot \omega_0 \tag{4.7}$$

An attractive force ($\partial F_z/\partial z > 0$) will decrease the resonant frequency while a repulsive force ($\partial F_z/\partial z < 0$) will increase the resonant frequency.

In AC mode, the cantilever/tip assembly may be regarded as a forced harmonic oscillator; the amplitude and phase of oscillations are a function of the resonant frequency. The phase of the cantilever, if driven at a frequency ω different from its resonant frequency, is given by:

$$\phi = \tan^{-1} \frac{\omega \omega_o}{Q(\omega^2 - \omega_o^{\,2})} \tag{4.8}$$

The shift in the resonant frequency given in equation 4.7 will effect a shift in the phase derived as follows [69]:

$$\frac{\Delta \phi}{\Delta \omega_0} = \left[\frac{\partial \phi}{\partial \omega} \right]_{\omega_0} \tag{4.9}$$

$$\Delta\phi = -\frac{Q}{k} \frac{\partial F_z}{\partial z} \tag{4.10}$$

where Q is the quality factor of the cantilever resonance. This phase shift is monitored by the photodetector, and is the measure of the force gradients due to the tip's interactions with the sample.

The AC detection technique was used for the work presented in this thesis. All "magnetic" images are maps of the above change in phase as a magnetic tip is scanned over the surface. In the next section, we derive the magnetic force on the tip.

4.4.3 Magnetic Substrates

Given the sample's stray field $\overline{H}$, each magnetic moment m in the tip experiences a force $\overline{F}$ given by [71]:

$$\bar{F} = \mu_0 \nabla(\bar{m} \cdot \bar{H}) \tag{4.11}$$

For a derivation of the force of a magnetic field on a magnetic dipole, see reference [72] on page 368. In the absence of an external free current at the location of the dipole, equation 4.11 is further simplified into:

$$\bar{F} = \mu_0 (\bar{m} \cdot \nabla)\bar{H} \tag{4.12}$$

If the tip has N dipoles per unit volume, the force density is:

$$\bar{f} = N\bar{F} = \mu_0 (\bar{M} \cdot \bar{\nabla})\bar{H} \tag{4.13}$$

Therefore, the total force on the tip is given by the following volume integral:

$$\bar{F}_{total} = \int_V \bar{f} dV \tag{4.14}$$

4.4.4 Single dipole tip approximation

Most of the experimental literature on MFM makes the simplifying assumption that the tip is a single magnetic dipole directed along the tip's axis [32-34, 73-76]. There is strong evidence supporting this assumption such as the shape anisotropy along the axis of the tip as well as holographic TEMs of the tips which reveal field lines emanating from what appears as a dipole pointing along the axis of the tip (Figure 4.12).

Assuming that the tip is a single dipole directed along z, the phase shift given by equation 4.10 now becomes:

$$\Delta\phi = -\mu_0 \frac{Q}{k} m_z \frac{\partial^2 H_z}{\partial z^2} \tag{4.15}$$

Therefore, by tracking the change in the phase of the oscillating cantilever as it scans the surface, we are effectively imaging the second derivative of the magnetic sample's stray fields.

4.4.5 Topography-Free Magnetic Imaging (Tapping/Lift mode)

MFM images are acquired in AC non-contact mode, at a nominal tip-sample separation of at least 20 nm. The force-distance curve of Fig. 4.13 is a plot of the Van der Waals (VDW) forces on the tip as a function of tip/sample separation. From Fig. 4.13, we conclude that the VDW forces have diminished significantly at 20 nm above the surface. To further cleanse the magnetic image from any 'contamination' due to topography, the makers of our MFM developed a clever method known as tapping/liftmode™. This method is described in reference [69] as follows: "The tip makes two passes over each raster scan line. In the first pass, the tip oscillates and lightly taps the sample to determine surface topography (Tapping Mode). In the second pass the tip is lifted to a selected height from the surface, typically between 10 and 200 nm. This height is added point by point to the recorded topography to

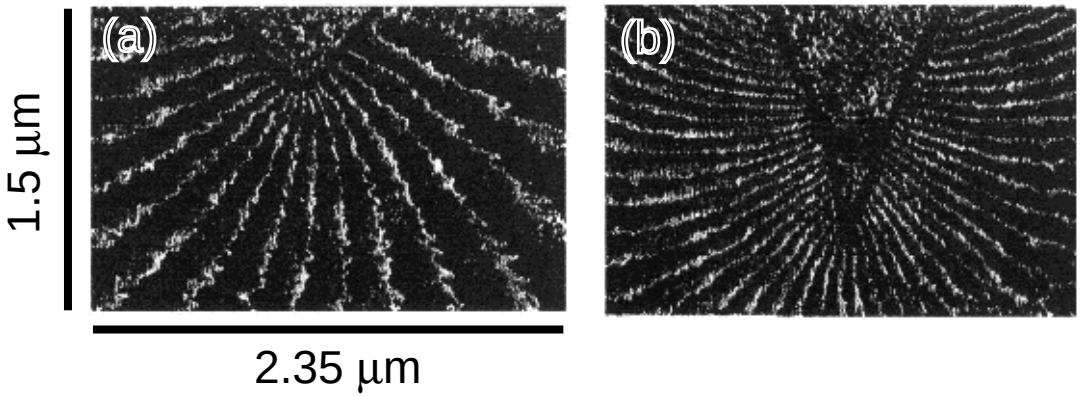

Figure 4.12 Electron holograms of thin film MFM probes. The two images (a) and (b) have the same scale. Equiphase lines for (a) a conical probe covered with 30 nm-thick Co film; and (b) a pyramidal tip covered with 16 nm thick CoCrPt film. Images were extracted from [71].

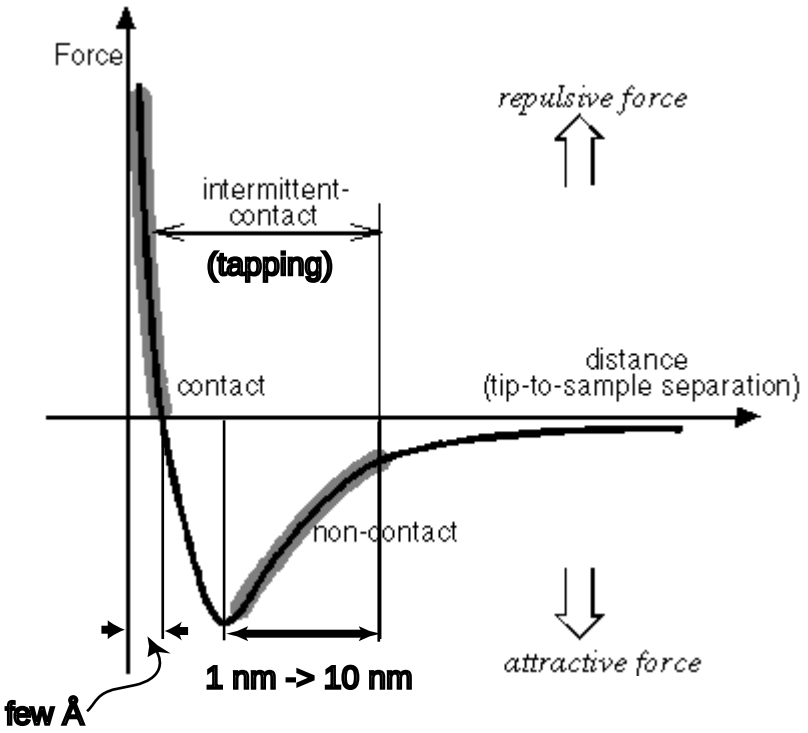

Figure 4.13 Plot of the interatomic-force between the tip of a scanning probe and the sample surface vs. distance between tip and surface, for a clean, non-magnetic, electrically neutral surface [77].

keep the tip-sample separation constant during scanning (Fig. 4.14). Magnetic force data is recorded during the second pass." The topographic image acquired during the first pass corresponds scan-line by scan-line to the magnetic image acquired in the second pass. This tech-

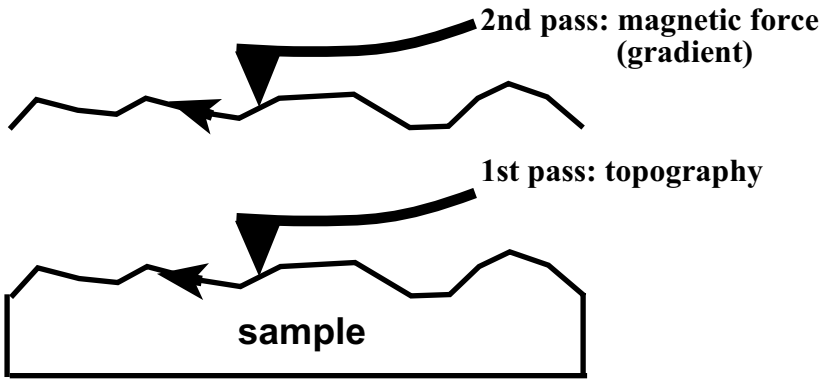

Figure 4.14 Schematic illustration of magnetic force microscopy by tapping/liftmode™. In the first pass, the tip images the topography by intermittently contacting the surface. In the second pass, the tip is lifted to a fixed height above the surface, and will retrace the topography such that any forces on the tip due to topography are always constant. This figure is reproduced from [69].

nique allows straight-forward correlation between sample geometry and magnetic domain structure.

4.4.6 Probes and Resolution

The lateral resolution of the magnetic image is limited by the probe-sample separation. Furthermore, MFM resolution and sensitivity depend strongly on the tip's geometry and magnetic composition. There are two common methods of fabricating tips for MFM. The first is the electrochemical etching of a ferromagnetic wire to a sharp point. This technique is less popular since wires with identical characteristics are difficult to reproduce [70]. Also, stray fields from etched wires are often too strong for non-destructive magnetic imaging [78]. The more popular method involves coating non-magnetic standard Si tips with a magnetic alloy [69]. The field of MFM advanced tremendously with the advent of batch-fabricated Si tips by standard planar processes similar to the ones described in Chapter 2 of this thesis [71]. Using photolithography and multiple etching steps, thousands of diving-board cantilevers with integrated tips are batch-fabricated on a single-crystal Si wafer (Fig. 4.15). Following that, the entire wafer is coated with a sputtered magnetic alloy, producing magnetic tips of similar char-

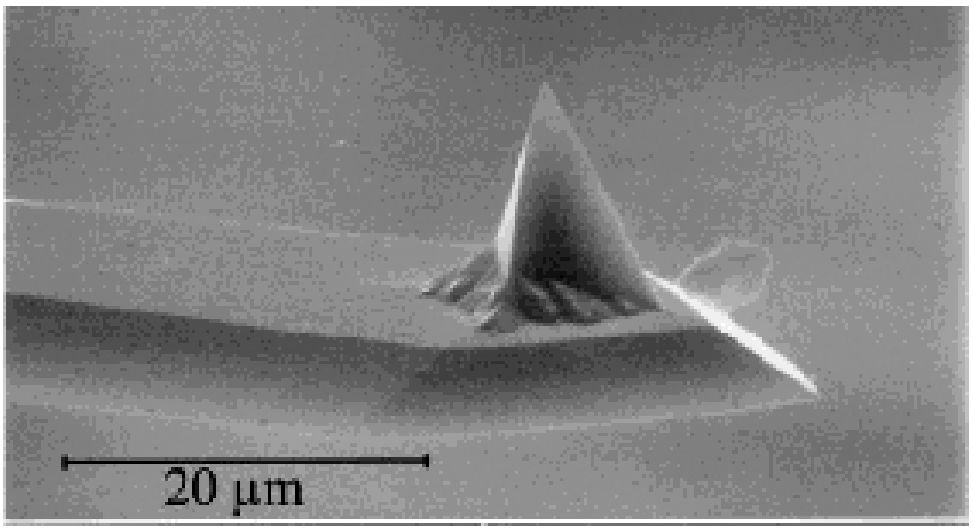

Figure 4.15 Scanning electron micrograph of a silicon cantilever and integrated tip. The tip has the shape of an asymmetrical pyramid. All tips used to acquire the force images in this thesis resemble this tip. This figure was extracted from [71].

acteristics. All probes used in this work are single-crystal Si cantilevers with pyramidal tips; the tips are coated with 40 nm of a Co-Cr alloy. This alloy shows strong out-of-plane anisotropy when sputtered onto glass substrates [75]. We refer to these probes as “regular moment” tips. We also use a “low-moment” tip to perform non-destructive imaging of the demagnetized state of a sample_ “low moment” tips are typically sputtered with 15 nm of the same Co-Cr alloy as “regular moment” tips [75]. Our cantilevers are 225 μm long with a spring constant of k~3 N/m, resonant frequency ω_0~ 80 kHz, and Q~200 in air. The end-radius of curvature of an uncoated tip is typically 5-10 nm [69]. The radius of curvature of a coated tip is about 30 nm, and has demonstrated resolutions better than 50 nm [10,43].

4.4.7 Imaging dipoles with dipoles

To achieve a graphical representation of the relationship of a diverging magnetic field to the change in phase experienced by an oscillating cantilever, we plot equation 4.15 for the field of a dipole pointing in the positive z direction (Fig. 4.16). Imaging the field of a dipole may be considered the impulse response of the microscope [73]. The field in the z-direction due to the sample is given by:

$$H_z = \frac{m_z}{4\pi} \frac{\left(2z^2 - x^2\right)}{\left(z^2 + x^2\right)^{5/2}} \tag{4.16}$$

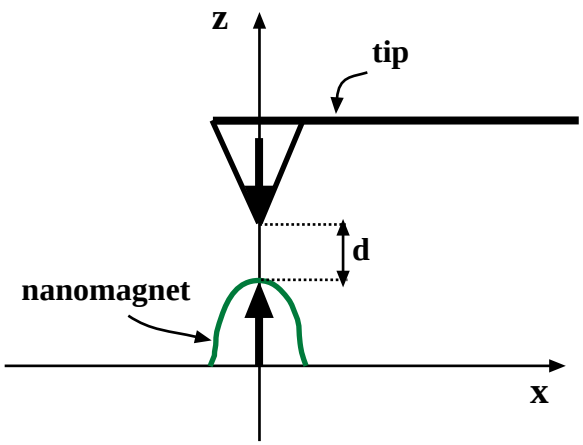

Figure 4.16 Schematic illustration of a magnetic-dipole tip imaging a magnetic-dipole particle.

where m_z is the strength of the sample's moment, and z is the location of the tip above the sample. A plot of the field in Equation 4.16, computed at a distance z=30 nm above the sample, is shown in Fig. 4.17a. The force on the tip due to the sample's field (eq. 4.11) is proportional to the first derivative of the z-component of this field. The first derivative of the field is shown in Fig. 4.17b. Finally, the signal that we probe with an MFM is the change in the phase of the oscillating cantilever; this signal is proportional to the second derivative of the z-component of the field (Fig. 4.17c). In Fig. 4.18, we plot the second derivative with respect to z of the field in equation 4.16, i.e. the change in phase, when the tip is at various scan-heights above an array of dipoles. The distance between tip and sample is given by z. Note that for small z, the signal changes polarity around the main peaks. As z increases, resolution is decreased and the lobes around the main peaks disappear.

In this work, we perform MFM using tapping/lift-mode. Therefore, scanning an array of particles generates two corresponding images of the topography and magnetic stray fields above the sample. An MFM micrograph of sample N-7, evaporated Ni, is shown in Fig. 4.19. The image on the left is the topography in which all particles appear identical in contrast. The image on the right is the magnetic phase-image. The magnetic image was captured at a tip-sample separation of 50 nm. Nanomagnets that attract the tip effect a negative change in the phase (dark spot) while nanomagnets that repel the tip effect a positive change in phase (light spot). This image was acquired with a regular moment tip. The strength of this tip often exceeded the switching fields of the nanomagnets in the array. Certain dots in the magnetic image appear to switch polarity from light to dark during the scan. This observation is evidence of the tip's ability to magnetize the sample. There is good qualitative agreement between the simulations in Figure 4.18 and the magnetic image of sample N-7. The simulation assumes both tip and sample are perfectly localized dipoles. The finite width of the real tip and nanomagnet serve to broaden the full-width-at-half-the-maximum of the peaks in the magnetic image [73].

Finally, we present an experimental demonstration of magnetic imaging at a variety of tip positions above the sample. Figure 4.20 contains micrographs of the phase image of sample P3 (tall, electroplated Ni) for tip positions from 30 nm to 200 nm. We observe a diminishing of the signal-to-noise ratio as the tip-surface separation is increased. However, we are able

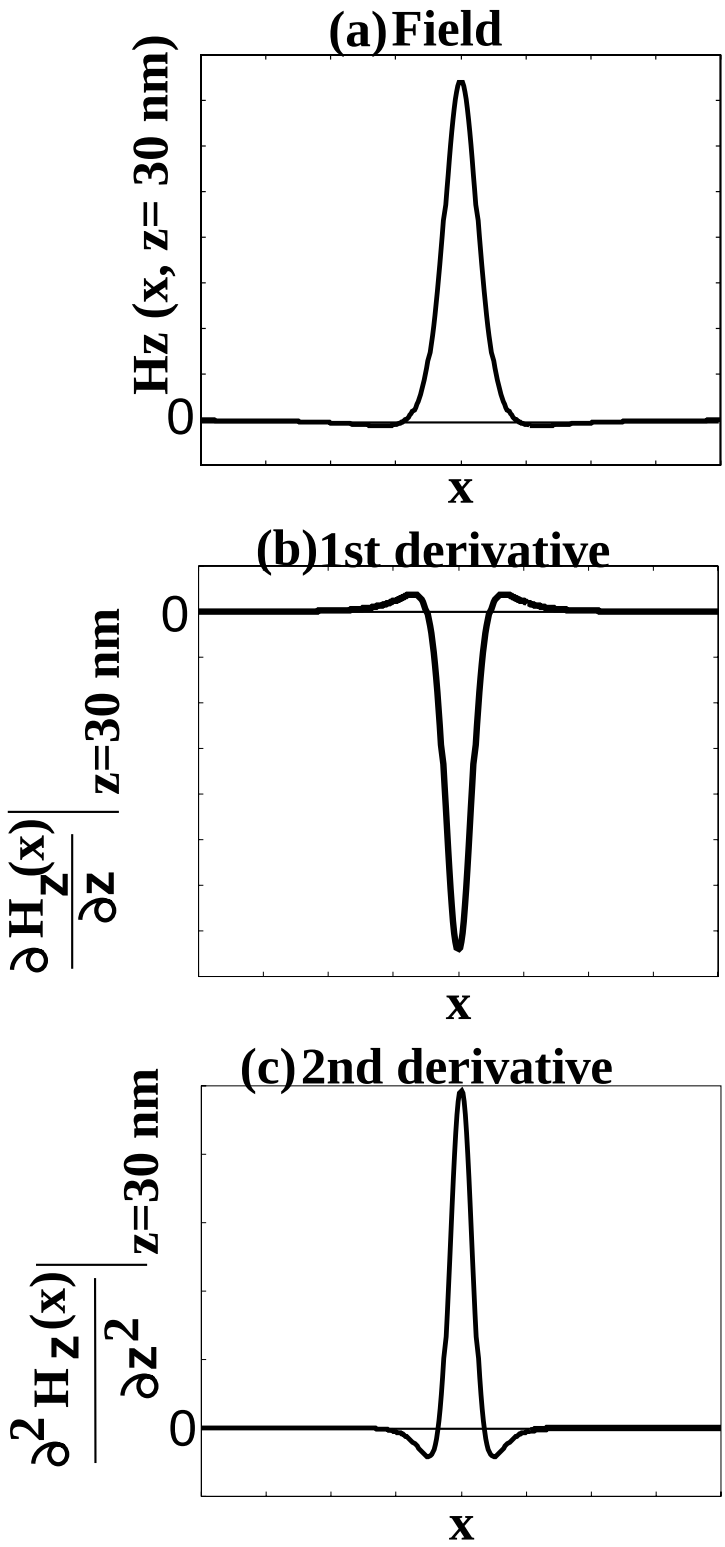

Figure 4.17 (a) A plot of the z-component of the H field above a dipole as a function of x at a distance of z=30 nm above the dipole. (b) The first partial derivative in z of the z-component of the H field plotted as a function of x for z=30 nm above the dipole. (c) The second partial derivative in z of the H field in (a) as a function of x.

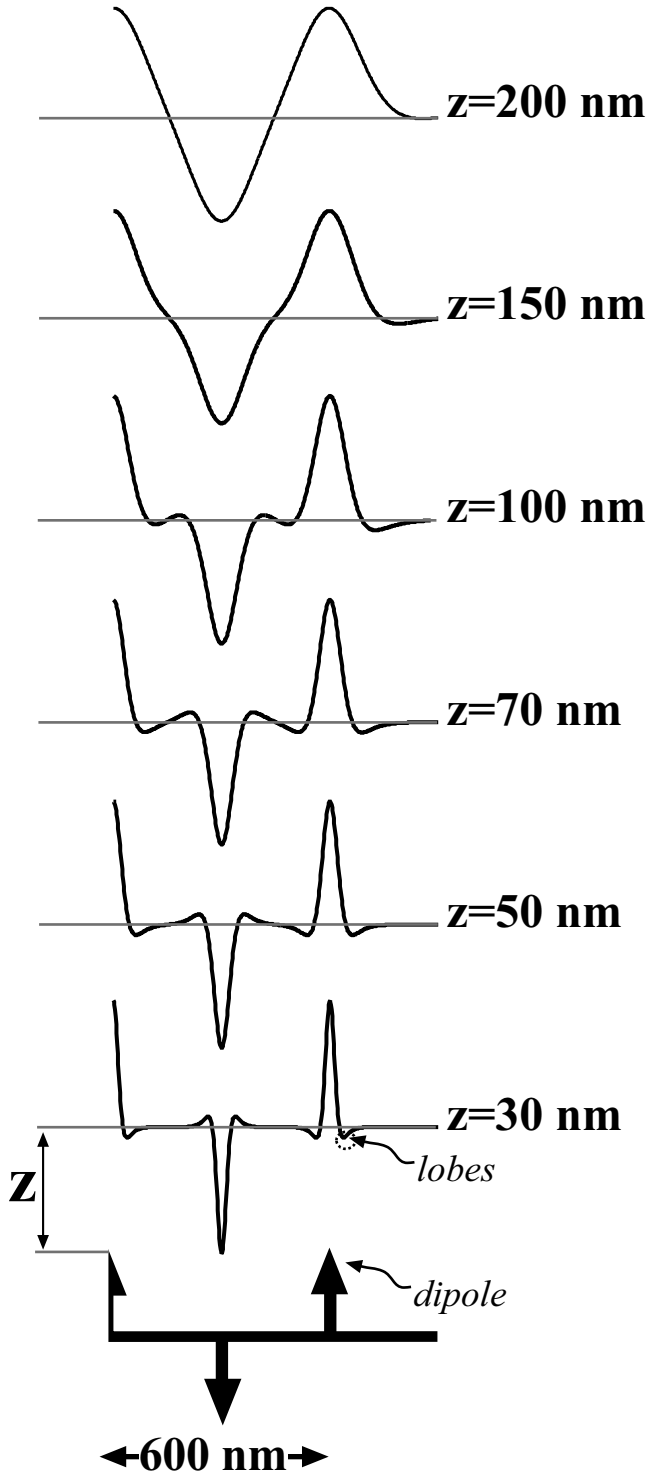

Figure 4.18 A plot of the second partial derivative in z of the z-component of the H field above the dipoles (illustrated at the bottom of the figure). The second partial derivative is computed for z=30, 50, 70, 100, 150, and 200 nm above the dipoles.

to distinguish an attractive particle from a repulsive particle even when the tip is 100 nm above the surface.

4.4.8 Probe calibration

Calculation of the stray fields of a magnetic tip require detailed knowledge of tip geometry and morphology. Experience has shown us that seemingly identical tips may exhibit significantly different field strength. To enable semi-quantitative interpretations of the magnetic images, we developed a method to characterize the tips. In fact, our method makes use of our samples to estimate the strength of a tip's stray field.

Due to strong magnetostatic interactions, sample P3, the highest aspect-ratio plated Ni sample, achieves the lowest magnetostatic energy state whenever adjacent pillars have antiparallel magnetization. This ground state may be induced in the sample by AC demagnetization in a vibrating sample magnetometer. To AC demagnetize the sample, an applied field is cycled

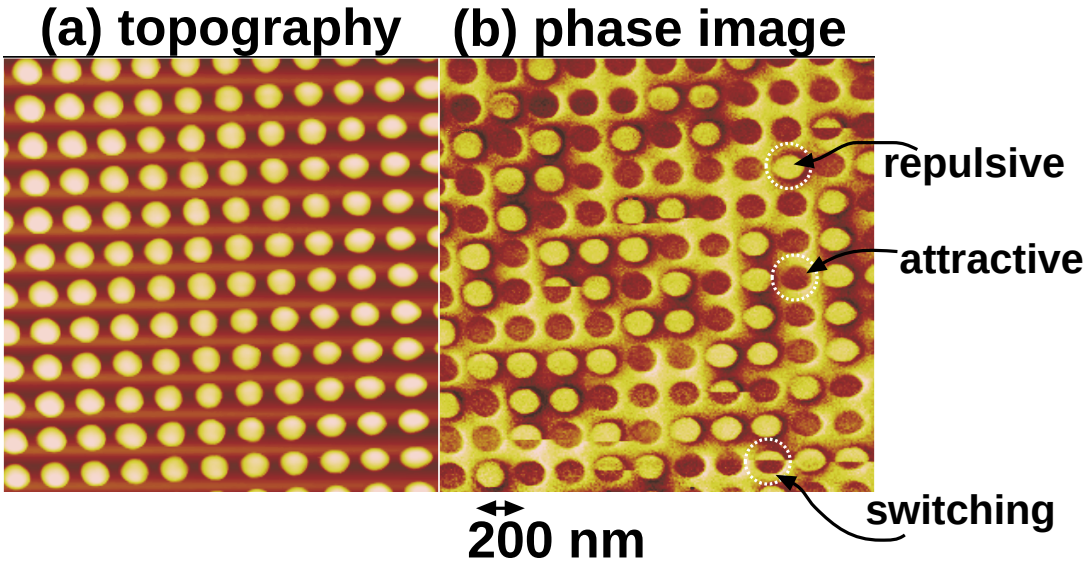

Figure 4.19 Two corresponding micrographs of the topography as well as phase image of evaporated Ni sample N7, acquired by magnetic force microscopy. (b) The phase image which indicates the second partial derivative in z of the z-component of the H field above the sample is typical of an array of dipole fields perpendicular to the substrate.

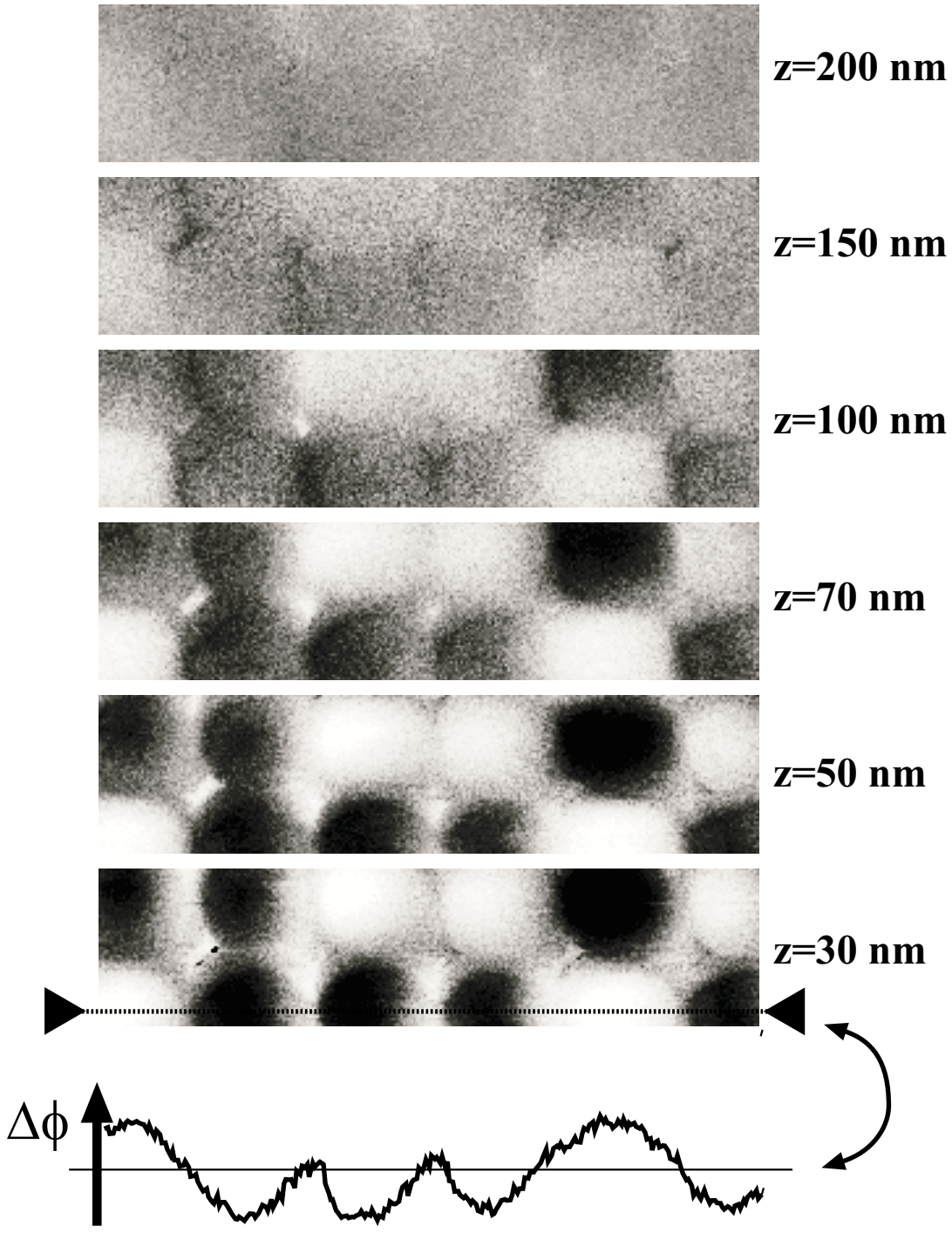

Figure 4.20 Phase images of electroplated Ni sample P3 acquired with the tip at z=30, 50, 70, 100, 150 and 200 nm above the surface. The line trace at the bottom of the figure (which corresponds to the indicates cross section) is a plot of the change in phase of the oscillating cantilever as the tip traces the surface topography at 30 nm above the surface.

from a value that saturates the sample to steadily decreasing values as illustrated in Fig. 4.21. The net moment of an AC-demagnetized sample is equal to zero, with half the posts magnetized up and half magnetized down.

The MFM image of this sample at ground state would resemble a checkerboard. This checkerboard state is observed, provided the stray field of the imaging tip is weaker than the coercivity of the individual particles. Figure 4.22 is an MFM image of sample P3 after AC-demagnetization; the image was acquired with a ‘low moment’ tip. The original image is displayed on the left. After removing the noise and increasing the contrast via software, we observe large patches of a checkerboard structure in the image on the right. Note that the original magnetic image is noisy since the signal is proportional to the moment of the tip, as shown in equation 4.15. This image illustrates the trade-off between non-interfering imaging and a good signal.

Ideally, we would use a stronger tip since weak tips are too noisy to resolve all magnetic structure. To measure the field from a strong tip, we image the same AC-demagnetized sample with a ‘regular moment’ tip as shown in Fig. 4.23. We note the following: 1) The increase in signal strength compared to the ‘low moment’ tip is proportional to the increase in

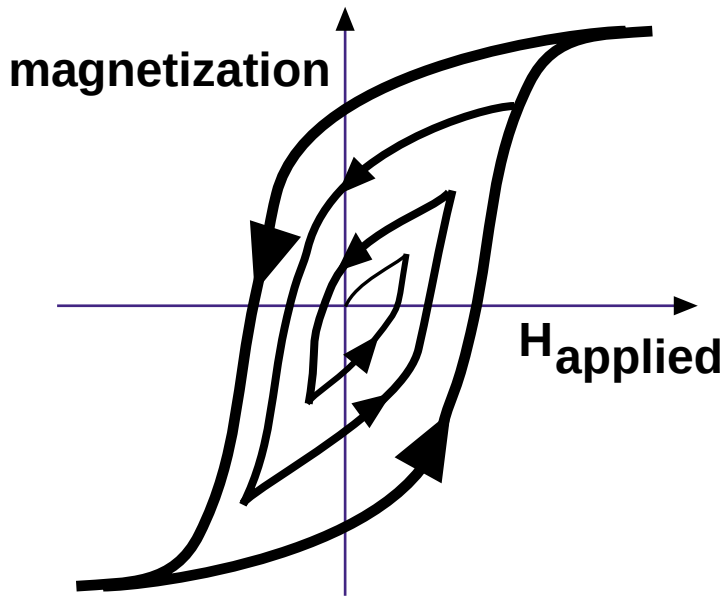

Figure 4.21 The process of demagnetizing a samples by cycling the applied field with a decreasing amplitude [14].

magnetic material coating the tip. 2) The sample's total moment is no longer 0; the number of attractive dots is much larger than the number of repulsive dots. We define the attractive dots

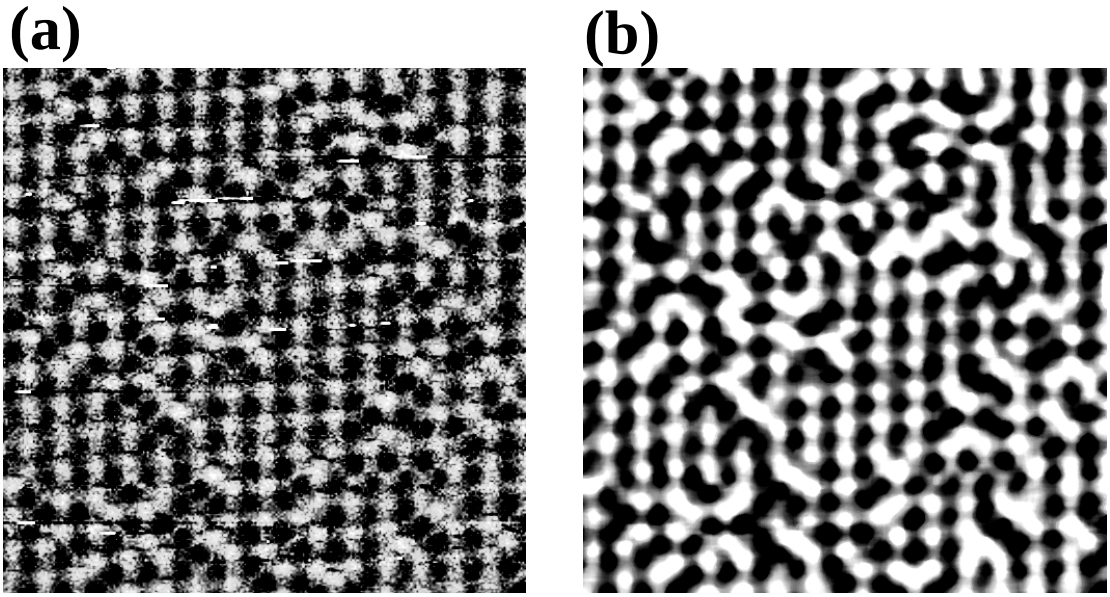

Figure 4.22 (a) A magnetic force (phase) image of electroplated Ni sample P3 after AC-demagnetization. This image was acquired with a week tip that does not disturb the magnetization of the sample. Consequently, the image is noisy. (b) This is a filtered version of the image in (a) that makes it easier to see the checker-board pattern that forms as a result of magnetostatic interactions.

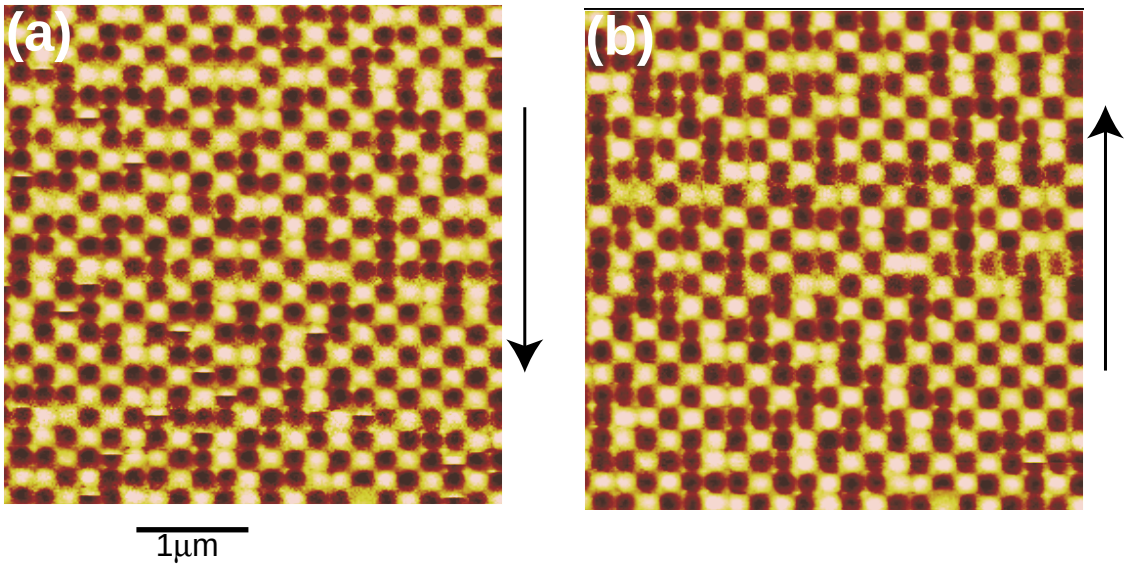

Figure 4.23 Magnetic force (phase) images of electroplated sample P3, acquired with a 'regular moment' tip. The arrows on the side of the figure indicate the direction of scan. Scan (a) was performed first, and scan (b) is a rescan of the same area as (a) in the opposite direction. Note that we observe switching in scan (a) but not (b).

as pointing up. By counting the number of dots that are up and the number of dots that are down, we estimate the sample's magnetization to be equal to $0.13M_s$, where M_s is achieved if all dots are pointing up. The external field required to bring the sample from the demagnetized state to a $0.13M_s$ state may be extracted from the sample's virgin curve (Fig. 4.24). A virgin curve is obtained using VSM AC demagnetization. An external field is increased from 0 until the sample is saturated. As with a hysteresis loop, the sample's moment is measured and plotted for each value of the external field. From this data, we estimate a tip field equal to 375 Oe.

Appendix G contains a number of scans performed with the same tip to evaluate the effect of wear on the strength of the tip. Tip wear is observed if the measured moment of the sample decreases, indicating that the tip is magnetizing fewer particles. The estimated moment of the sample does not degrade even after 10, 4 μm x 4 μm scans. This technique is

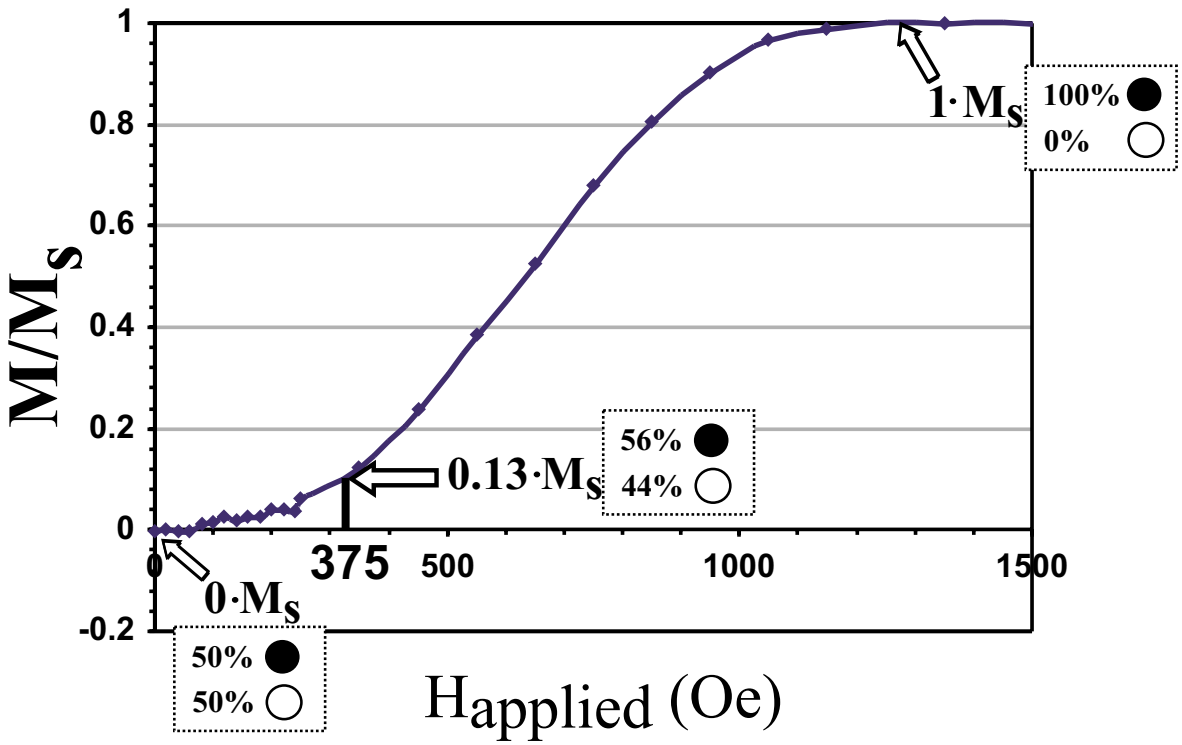

Figure 4.24 A plot of the virgin curve of electroplated sample P3. The saturation magnetization of this sample is M_s = 290 Oe. This plot is used to determine the field required to achieve a certain magnetization in the sample for the purpose of calibrating the strength of an MFM tip.

useful for estimating the stray field of a tip whenever the tip's strength is comparable to the coercivity of the calibration sample.

4.4.9 Switching-Field Experiments

MFM enables us to measure the switching field of the nanomagnets in our samples. This is arguably one of the more important applications of this form of microscopy. The experiment requires subjecting the sample to an external field of different values. The experimental procedure is explained in the following sections.

Experimental Apparatus

To apply an external field to our sample, we use a permanent magnet oriented perpendicular to the plane of the substrate. We position this magnet below the sample stage (Fig. 4.25). By varying the distance d that separates the sample from the magnet, we vary the external field that the sample is subject to. The total external field at the location of the sample is given by the sum of the field from the tip and the field from the permanent magnet:

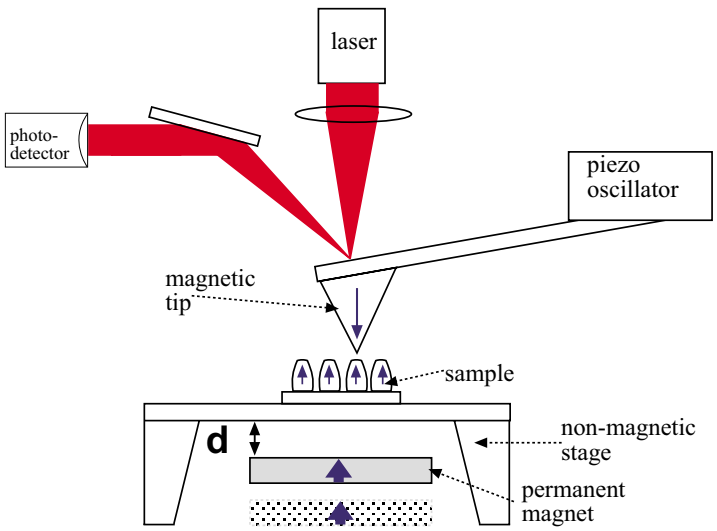

Figure 4.25 A schematic illustration of a method of applying a tunable external field to the sample during magnetic force microscopy using a permanent magnet. The permanent magnet is placed below the sample, and the distance separating sample and magnet is varied.

$$H_{ext\_tot} = H_{PM} + H_{tip} \tag{4.17}$$

where H_{ext_tot} is the total external field, H_{PM} is the field at the sample location due to the permanent magnet, and H_{tip} is the tip's field at the location of the sample.

More conventional methods of applying an external field to a sample in MFM involve placing the sample over a solenoid and passing current through the solenoid [79-81]. Our method which was developed by M. Abraham [43,82] has many practical advantages such as:

1) the absence of heating. In the case of a solenoid, if large amounts of current is passed through the winding, the heat produced becomes a limiting factor. The current can not be kept on for extended periods of time. This forces the investigator to obtain MFM images once the current is turned off; these images represent the remanent state of the sample and not the true, in-field, state [67].

2) volume issues. The number of windings necessary to generate a field of several hundred Oersteds requires a solenoid of a very large volume compared to a permanent magnet of identical strength.

One disadvantage of a permanent magnet is that the field has a diverging component whenever the sample is far from the magnet. Also, the magnitude of the field does not change linearly as a function of distance. Therefore, we can not vary the field by fixed-magnitude increments, which limits our ability to measure the particle switching field precisely. The on-

axis magnetic flux density of a cylindrical magnet with magnetization M_s (see Fig. 4.26) at a distance d above the magnet is approximated by [83]:

$$B = \frac{\mu_0 M_s}{2}\left(\frac{L+d}{\sqrt{R^2+(L+d)^2}} - \frac{d}{\sqrt{R^2+d^2}} \right) \tag{4.18}$$

where L is the length, R is the radius of the magnet.

4.4.10 Saturation Experiments

A saturation experiment is performed with an *in situ* tunable magnetic field. This external field is increased starting from a small value until all nanomagnets in the sample are oriented in the same direction as the external field. MFM scans are obtained for each value of external field.

ELECTROPLATED NI SAMPLE

We report on a saturation experiment performed on an “as grown” Ni sample. That is, the sample is not exposed to a magnetic field *a priori*. The MFM tip field and the permanent magnet field are oriented in the same direction, as indicated in Fig. 4.27. The total external field is given by equation 4.17. Initially, the permanent magnet (PM) is far from the sample such that its contribution is weak. The PM is made to approach the sample. Figures 4.27a through f are magnetic images of a 4 μm x 4 μm array of particles as H_{ext_tot} increases from

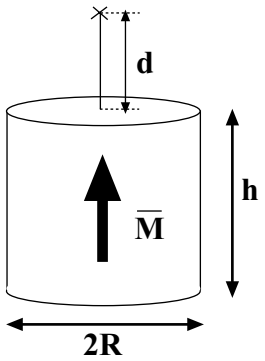

Figure 4.26 A cylindrical bar magnet magnetized along the axis of the cylinder. The magnetic field expressed in equation 4.18 is computed at a distance d above the magnet.

206 Oe to 760 Oe. As explained before, dark particles are aligned with the external field, while light particles are antiparallel to the external field. In Fig. 4.27a, 62% of the particles are aligned with the field. In Fig. 4.27f, all particles are aligned with the field. Therefore, by

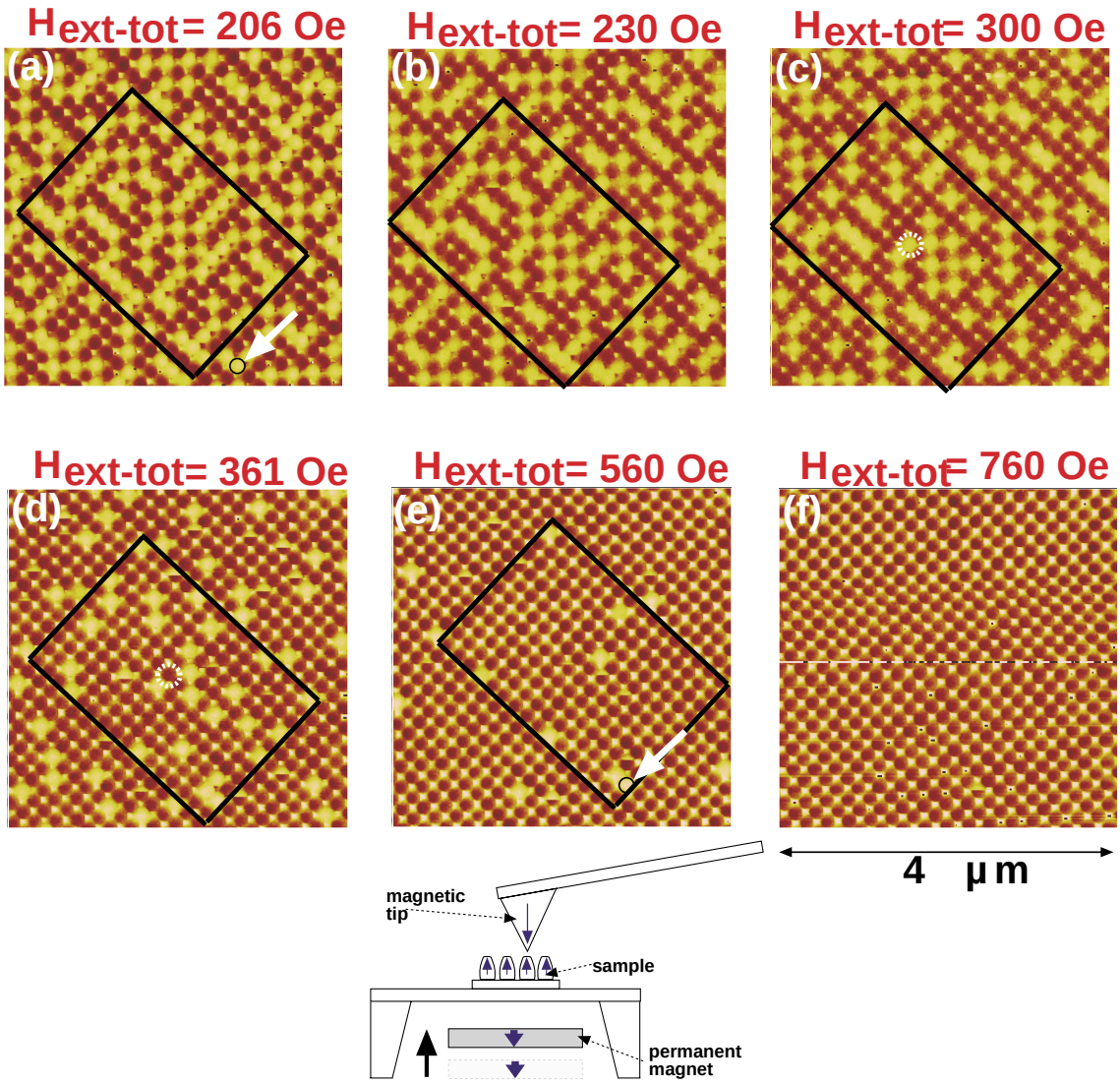

Figure 4.27 Magnetic force (phase) images of electroplated sample P3 acquired in an increasing external field. The sample progresses from a state where approximately 60% or the magnets are attracting (aligned with) the tip to a state where 100% of the nanomagnets are aligned with the tip. These scans were obtained without moving the sample's stage. The black rectangle borders those particles that appear in all the scans.

increasing the external field by 760-206=554 Oe, we are able to saturate the sample. We plot the number of particles whose magnetization has switched from repulsive (light) to attractive (dark) vs. the applied field in Fig. 4.28a and b. We observe that the largest amount of switching occurs as the external field increases from 300 Oe to 361 Oe.

In addition to H_{ext_tot}, a nanomagnet switches under the influence of the total field due to its neighbors. MFM scans allow us to estimate the field due to the neighbors since the condition of the neighbors (up or down) is being imaged. For example, consider the particle circled in Fig. 4.27c. This particle appears to have switched in the next scan (Fig. 4.27d). We estimate the field due to the neighbors of this particle to be ~ -163 Oe. Assuming the particle

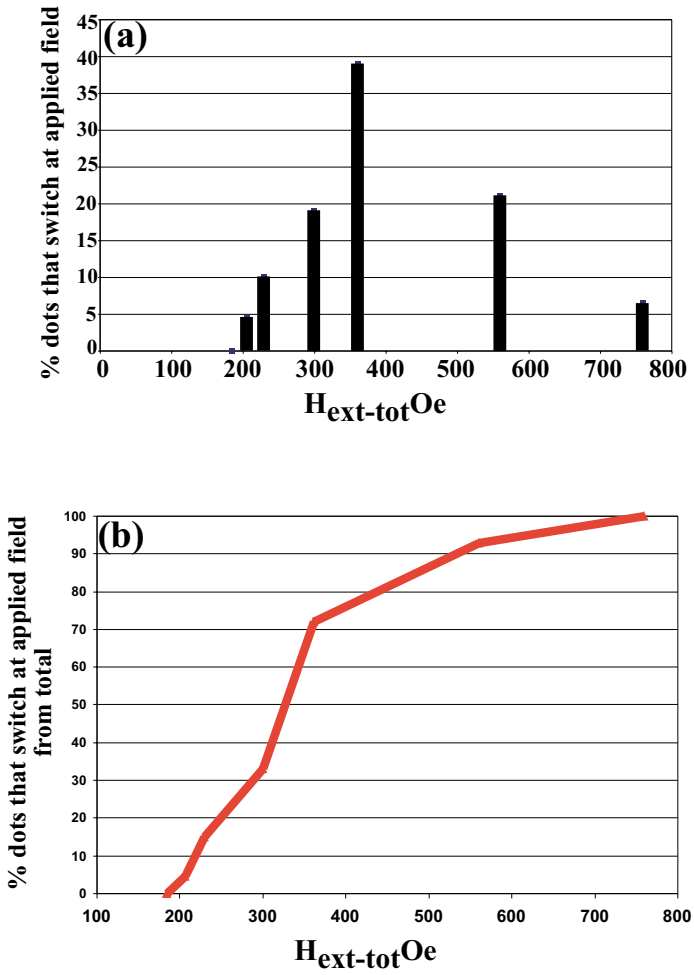

Figure 4.28 MFM data from the experiment depicted in Fig. 4.27. (a) a plot of the total number of particles that have switched due to the increase in applied field vs. applied field. (b) The same data as (a) plotted as a ratio of the total number of particles that switch throughout the duration of the experiment.

switched for an external field of 330 Oe, the switching field of the particle is then 330-163 = 167 Oe. In Fig. 4.27a, the average field due to the neighbors is 84 Oe; therefore, a particle which switches during this scan has a switching field equal to 206-84=122 Oe. In Fig. 4.27f, the average neighbor field is at a maximum value of 450 Oe. A particle that switches during scan f may have a switching field as large as 310 Oe. Therefore, the spread in switching fields for the particles that switched during this experiment ranges from 122 Oe to 310 Oe. Since the field is stepped in large increments between consequent scans, we are not able to calculate the switching fields of each particle exactly. However, we demonstrate that MFM is a powerful technique for measuring the switching field of single-domain-like, nanostructured magnets.

4.4.11 MFM Generated Hysteresis Loops

By varying the external field and counting the number of particles oriented up or down, it is possible to generate ‘MFM hysteresis loops'. MFM loops plot the net number of particles with magnetization up vs. applied field.

EVAPORATED CO SAMPLE

The following sections follow reference [30] very closely:

Figure 4.29 shows a set of MFM images of sample C-6, taken at different applied fields. Initially, the sample was saturated with magnetization opposite to the tip and permanent magnet. A magnetic field from a permanent magnet was gradually increased by moving the magnet closer to the sample. The magnetic images were obtained with a ‘regular moment’ tip. As seen in the previous section, the combined field from the tip and the magnet reverse the particles' magnetization. However, the field from the tip was strong enough to reverse many of the particles, even with no additional field applied. At one value of applied field, the image shows 50% of the particles magnetized up and 50% down. The total applied field at this point corresponds to the coercivity of the sample, which was 620 Oe from VSM. The field from the magnet was less than 30 Oe, implying that the probe tip produced a field of approximately 600 Oe.

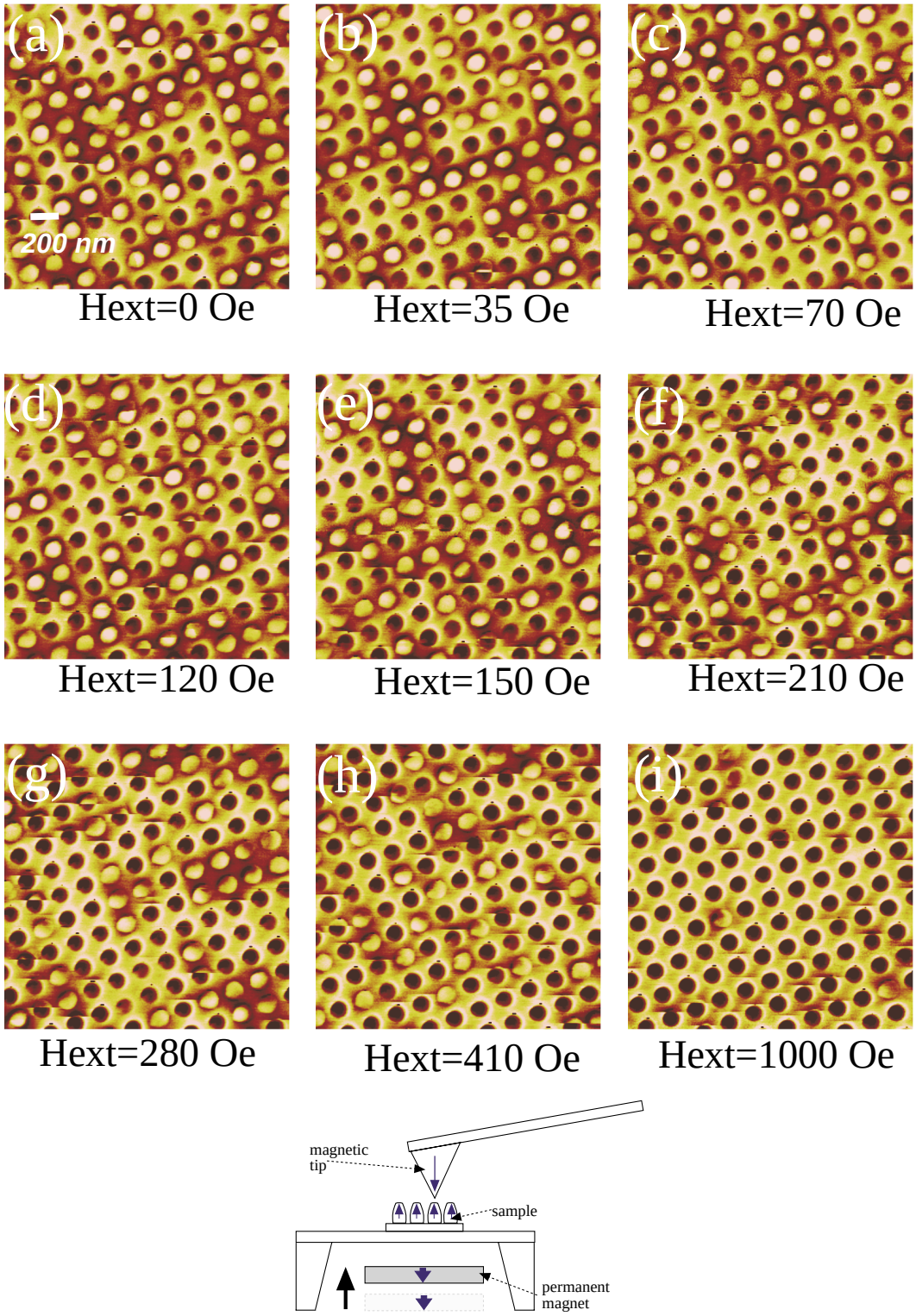

Figure 4.29 Magnetic force (phase) image of evaporated Co sample C-6 in a variety of external fields. The external field is increased from 0 Oe, where half the nanomagnets are magnetized like the tip and the other half oppose the tip, to 1000 Oe where all the particles are magnetized in the same direction as the tip. The apparatus illustrated at the bottom of the sample depicts the orientation of the permanent magnet and the magnetic tip.

Fig. 4.30 shows the net percentage of particles magnetized up vs. field, compared with the hysteresis loop measured by VSM, for sample C-6. It is seen that switching of the particles is accomplished within a much smaller field range than is indicated by the VSM saturation field. For instance, at an applied field of 1500 Oe the particles are 98% magnetized up, but VSM shows a magnetization of 0.75 M_s, and it requires more than 4000 Oe to fully saturate the sample. The difference is attributed to the fact that individual particles have non-square hysteresis loops with remanence less than 1. At small fields, the moments are not saturated parallel to the particle axis. If individual particles do not saturate until large fields, the VSM loop will show a slow approach to saturation even though all the particles have already reversed their magnetization, as seen in MFM.

EVAPORATED NI PARTICLES

Similar results were obtained for a nickel sample, N-7, and are shown in Fig. 4.31. In this experiment the sample was saturated up and the probe tip down. A large external field was applied upwards, and gradually decreased so that the particles began to reverse under the influence of the tip field. The Ni particles changed from 84% up to 50% up over a field interval of less than 100 Oe. At 50% up, the total applied field was equal to the coercivity. As in the

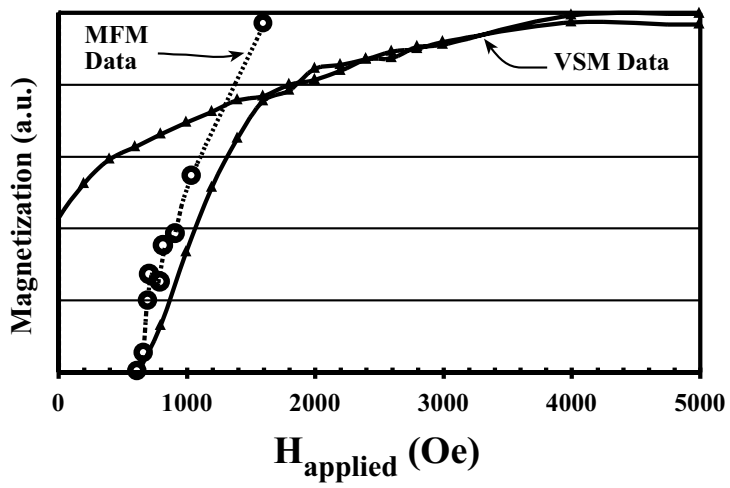

Figure 4.30 A plot of the data acquired in the experiment of Fig. 4.29 superposed on the first quadrant VSM hysteresis loop of sample C-6. The array of particles that was imaged in Fig. 4.29 saturates at a field that is several hundred Oe below the saturation field indicated in the VSM loop.

case of Co, the hysteresis loop measured by VSM shows a more gradual change in magnetization with applied field.

This sample was also used to measure the coercivity of the tip. The exact experimental procedure is found in Appendix I. We measure a tip coercivity of ~425 Oe for the tip used in this experiment.

4.4.12 Analysis of Switching Data from Evaporated Particles

To separate the effects of magnetostatic interactions from intrinsic variability between particles, we can compare the calculated interaction field to the measured field needed to saturate the sample. For C-6, MFM shows that the particles' magnetization direction changed from 50% attractive to 77% attractive over a field range of 410 Oe. This corresponds to a change from zero average interaction field to 199 Oe. Hence, some of the spread in apparent switching fields can be attributed to interactions, but about half of it represents a real variability in the particles' intrinsic switching fields. In contrast, for sample N-7, the particles changed from 50% to 83% up over a field range of 100 Oe. This corresponds to a change from zero average interaction field to 136 Oe. Hence, in this sample the change in interaction field is sufficient to account for the entire range observed in switching fields, and the intrinsic variability is small. We conclude that Co samples show more intrinsic variability than Ni. Note that the calculated interactions fields assume saturation of the particles, and are therefore maximum values.

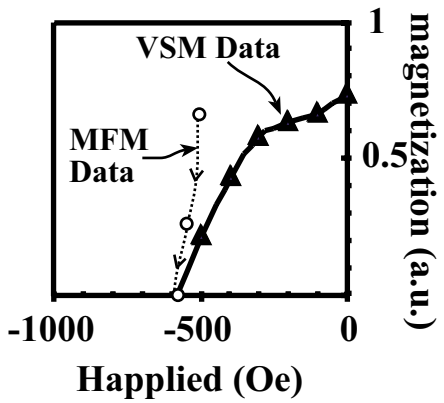

Figure 4.31 MFM data from evaporated Ni sample N-7 superposed on the second quadrant of the VSM hysteresis loop.

Intrinsic variability between particles originates from differences in microstructure, defects or surface condition which alter the switching field. We found previously [84] that an array of 30 nm-diameter evaporated Ni particles also reversed inhomogeneously. A spread in switching fields occurred because the microstructure of the particle dominated the reversal process. In another experiment on single-crystal Ni pillars [43], a standard deviation of σ = 105 Oe was determined for curling reversal of the particles, due to fluctuations in particle size and in the direction of the crystallographic axes within the particles. Several other studies on particle arrays have shown substantial ranges of switching fields [67,85], although the contributions from interactions have not been separated from intrinsic variability between particles.

If the microstructure dominates the reversal of the particles in the present study, then this provides an explanation for why Co should show higher switching field variability than Ni. Each particle consists of order 50 - 100 columnar grains, which in Co have a strong uniaxial anisotropy. A spread in the sizes and shapes of the grains will lead to a larger spread in switching field for Co because both the magnetocrystalline and shape anisotropy of the grains will vary. Other differences between particles, for instance small changes in particle shape, or antiferromagnetic coupling from the surrounding oxide, can also contribute. For Ni, variability is smaller because the material has weak cubic instead of strong uniaxial anisotropy.

4.4.13 Conclusion

This section is a demonstration of the several studies of nanostructured magnets that are possible with MFM. First, we were able to verify that individual nanomagnets in perpendicular samples indeed behave like dipoles. Second, as stated in chapter one, an understanding of the homogeneity of an array of single-domain particles is critical to the design of a read/write head. In this section, we have demonstrated that an MFM with an *in situ* magnetic field is a powerful technique for measuring the switching field of magnetic nanostructures. Furthermore, MFM can probe the nature of any variation in the switching field of an array of particles since it reveals the state of all neighbors at once. In this study, we saw that the spread in switching fields for electroplated Ni particles is due to the strong magnetostatic interaction field within the array. Evaporated Ni particles interact less, and are more homogeneous since the magnetocrystalline anisotropy is weak. Co particles have a larger intrinsic spread in their

switching field since crystal anisotropy is strong. Therefore, any slight changes in microstructure lead to variations in the switching field of the nanomagnets.

MFM and other scanning probe techniques are being developed for applications in data storage. Though these technique have potential for atomic level storage, the major technological obstacle is the need to move the tip at very high speed over non-smooth surfaces and control tip-surface separation at the angstrom level. To this end, several laboratories have reported impressive multiple-probe cantilever demonstrations [86]. Multiple probes relax the speed requirement on each individual cantilever, while still maintaining fast read/write times. The major challenges of multiple-probe cantilevers involve reliability and tolerance, as explained in [86].

CHAPTER 5: CONCLUSION

In this thesis, we seek to understand the magnetic behavior of nanostructured ferromagnetic particles based on experimental observation and a comparison to theory. In particular, we have fabricated 200 nm-period arrays of nanostructured Ni and Co by the techniques of evaporation and electroplating. We have characterized the bulk behavior of the arrays via vibrating sample magnetometry (VSM), and imaged the magnetic field of individuals particles using magnetic force microscopy (MFM). To identify the sources of magnetic anisotropy within the nanomagnets, we compare the measured remanence states of fabricated samples to micromagnetic simulations.

The arrays of nanomagnets we fabricated are vehicles for fundamental studies of magnetism. Also, they have potential technological applications in data storage and magnetic memories. In this thesis, we have focused on the attributes that render the arrays suitable for perpendicular data storage. Results from bulk characterization experiments of samples with perpendicular anisotropy indicate the samples are thermally stable since the out-of-plane coercivity is non-zero. Micromagnetic simulations show either a flower- or vortex-shaped magnetization configuration within each particle, depending on the size, aspect-ratio, shape and magnetic anisotropy of the particle. The conical shape of evaporated particles promotes an out-of-plane flower state even in the absence of other sources of anisotropy. Also, the columnar microstructure of the evaporated particles and the tendency of the crystallographic-easy-axis to be oriented perpendicular to the plane contribute to the out-of-plane anisotropy of the nanomagnets. MFM images of out-of-plane evaporated samples indicate that each particle is

like a dipole. Furthermore, MFM switching experiments allow us to measure the variability of switching fields of the nanomagnets in a sample. Magnetostatic interactions between the nanomagnets broaden the spread of switching fields of the particles in an array. Also, our MFM switching data shows greater variability in the switching fields of Co nanomagnets compared to Ni nanomagnets; this is not surprising since Ni has weaker crystal anisotropy.

In the case of the plated particles, crystal anisotropy is weak. However shape anisotropy is strong and stabilizes the out-of-plane state in each particle despite the magnetostatic coupling between the nanomagnets. Strong magnetostatic coupling is undesirable for data storage. Magnetostatic interactions are reduced by reducing particle volume or increasing interparticle spacing.

As a result of this work, we observe that the magnetic behavior of nanostructured magnets is a function of their size and geometry, and is also dictated by microstructure. Therefore, to produce reliable devices based on nanomagnets, we may need to control the lithography process as well as the grain structure precisely [30]. Our investigation of nanostructured magnetic particles is still a work in progress, and involves the efforts of several researchers within and outside MIT. In addition to examining other material systems such as amorphous alloys [61], a necessary objective is to pursue nanostructured, isolated, magnetic particles with yet smaller dimensions, yielding areal densities greater than 100 Gbits/in^2 (or arrays with 80 nm periodicity). A variant of interference lithography, known as achromatic interference lithography (AIL), based on a shorter wavelength laser has already been used to fabricate arrays of nanomagnets with a 100 nm period [52]. An emerging lithography, currently under development at the NanoStructures Laboratory which appears suitable for our application is x-ray-based, zone-plate-array lithography (ZPAL) [87]. X-ray ZPAL will possess the necessary resolution required for 100 Gbit/in^2 lithography since the source is the 4.5 nm wavelength of the carbon K-line. Also, since ZPAL can write patterns with arbitrary geometry [88], the nanomagnets may be written in concentric circles. A circularly-symmetric medium of discrete magnetic particles may perhaps be read and written with the conventional read/write head of a hard disk [10].

During the past decade, researchers and inventors have proposed a variety of applications that are based in nanomagnets such as magnetic random access memories (MRAMs).

Our group's effort in MRAMs aims to achieve the smallest MRAM arrays in the world. Recently, a group at the University of Cambridge, UK, proposed interesting nanomagnet-based devices for ultra-low power processing technologies [89]. In fact, they implemented logic gates by taking advantage of the anisotropy of and magnetostatic coupling between neighboring nanomagnets. The goal of our group is to establish an exhaustive portfolio of nanostructured magnets to facilitate the design of practical devices for various applications.

APPENDIX A

Relevant Publications

This is an up-to-date (10/09/2000) list of publications resulting from our effort on nanostructured magnetic particles and thin films.

[A1] Farhoud, M., M. Hwang, H.I. Smith, J.M. Bae, K. Youcef-Toumi and C.A. Ross, "Fabrication of large area nanostructured magnets by interferometric lithography", IEEE Trans. Magn. 34 1087-9 (1998)

[A2] Savas, T.A., M. Farhoud, M. Hwang, H.I. Smith and C.A. Ross, "Properties of large-area nanomagnet arrays with 100 nm period made by interferometric lithography", J. Appl. Physics 85 6160-2 (1999)

[A3] Twisselmann, D.J., M. Farhoud, H.I. Smith and C.A. Ross, "In-plane magnetic anisotropy in CoCrPt and CoCrTa films deposited onto patterned silicon substrates", J. Appl. Physics 85 4292-4 (1999)

[A4] Ross, C.A., T.A. Savas, H.I. Smith and R. Chantrell, "Modelling of hysteresis loops of arrays of 100 nm period nanomagnets", IEEE Trans. Magn. 35 3781-3 (1999)

[A5] Wang J.Q., L.M. Malkinski, Y. Hao, C.A. Ross, J.A. Wiemann and C. O'Connor, "Fabrication of pseudo-spin-valves and 100 nm sized periodic elements for magnetic memory application", Mater. Sci. Eng. B76 p1-5 (2000)

[A6] Farhoud, M., J. Ferrera, A.J. Lochtefeld, M.L. Schattenburg, C.A. Ross and H.I. Smith,

"Fabrication of 200nm period nanomagnet arrays using interferometric lithography and a negative resist", J. Vac. Sci. Technol. B17 3182-5 (1999)

[A7] Ross, C. A., H.I. Smith, T. Savas, M. Schattenburg, M. Farhoud, M. Hwang, M. Walsh, M. Abraham, R. Ram "Fabrication of Patterned Media for High Density Magnetic Storage", J. Vac. Sci. Technol. B17 3168-76 (1999)

[A8] Hwang, M. M.C. Abraham, T.A. Savas, H.I. Smith, R.J. Ram and C.A. Ross "Magnetic force microscopy study of interactions in 100 nm period nanomagnet arrays", J. Appl. Phys. 87 p5108-10 (2000)

[A9] Farhoud M., H.I. Smith, M. Hwang and C.A. Ross "The effect of aspect ratio on the magnetic anisotropy of particle arrays", J. Appl. Phys. 87 p5120-2 (2000)

[A10] Malkinski, L.M., J-Q. Wang, W.L. Zhou, J.M. MacLaren and C.A. Ross, "Improvement of giant magnetoresistance performance of a metal layered structure", J. Appl. Phys. 87 p6394-6 (2000)

[A11] Y. Hao, M. Walsh, C.A. Ross, H.I. Smith, J. Wang, L. Malkinski, "In-plane anisotropy in arrays of magnetic ellipses", *in press,* IEEE Trans. Magn. (2000)

[A12] M. Shima, A.C. Ford and C.A. Ross, , "Crystallographic and magnetic properties of Cr/CoCr(Ta,Pt) films produced by pulsed laser deposition", *in press,* IEEE Trans. Magn. (2000)

[A13] D. Twisselmann, Y.J. Shine, C.A. Ross, "Correlation of stress and magnetic anisotropy in Cr/CoCrPt films grown on textured substrates", *in press,* IEEE Trans. Magn. (2000)

[A14] C-C. Hsu, R.S. Indeck, A. Jander, M.W. Muller, C.A. Ross, D.J. Twisselmann, "MFM observation of magnetization reversal process in recording media with lithographically defined texture", *in press,* IEEE Trans. Magn. (2000)

[A15] M. Hwang, M. Farhoud, Y. Hao, M. Walsh, T.A. Savas, H.I. Smith, C.A. Ross, "Major hysteresis loop modelling of two-dimensional arrays of single-domain particles", *in press,* IEEE Trans. Magn. (2000)

[A16] M. Walsh, Y. Hao, C.A. Ross, H.I. Smith, "A bilayer resist process for nanostructuring magneto-resistive thin films", *in press,* J. Vac. Sci. Technol. B (2000)

[A17] C.A. Ross, R. Chantrell, M. Hwang, M. Farhoud, T.A. Savas, Y. Hao, H.I. Smith, F.M. Ross, M. Redjdal and F.B. Humphrey, "Incoherent magnetization reversal observed in 30-nm Ni particles", *in press,* Phys. Rev. B (2000)

[A18] Twisselmann, D.J, B.T. Adekor, M. Farhoud, H.I. Smith and C.A. Ross, "In-plane anisotropy in CoCrTaPt/Cr films deposited onto substrates with controlled topography", Proc.Materials Research Society 517 193-8 (1998)

[A19] Henry I. Smith, D.J.D. Carter, J. Ferrera, D. Gil, J. Goodberlet, J.T. Hastings, M.H. Lim, M. Meinhold, R. Menon, E.E. Moon, C.A. Ross, T. Savas, M. Walsh, F. Zhang, "Soft x-rays for deep sub-100 nm lithography, with and without masks" *in press*, Proc.Materials Research Society (2000)

[A20] Ross, C.A. and H.I. Smith, "Patterned media: 200 Gb/in^2 or bust", *Data Storage*, 41-48 (Sept. 1998)

[A21] Ross, C.A. "Patterned media", invited article for Encyclopedia of Materials: Science and Technology, ed. R.W. Chantrell, *in press,* (2000)

[A22] Ross, C.A., "Patterned magnetic media", Annual Review of Materials Science, submitted (2000)

[A23] J.Y. Cheng, C.A. Ross, V.Z.H. Chan, E.L. Thomas, R.G.H. Lamertink and G.J. Vancso, "Fabrication of nanopatterned thin films using self-assembled block copolymer lithography", *abstract submitted to Mater. Res. Soc. Fall Mtg. (2000)*

[A24] M. Shima, C.A. Ross, "Effect of ion bombardment on texture development in Cr films", *abstract submitted to Mater. Res. Soc. Fall Mtg. (2000)*

[A25] L. Spinu, H. Srikanth, S. Li, J. Fang, E.E. Carpenter, W.L. Zhou, M. Farhoud, C.A. Ross and C. O'Connor, "Transverse susceptibility and magnetic anisotropy in nanoparticle systems", *abstract submitted to Mater. Res. Soc. Fall Mtg. (2000)*

[A26] M. Shima, M. Hwang, M. Farhoud, T.A. Savas, H.I. Smith, C.A. Ross and W. Schwarzacher, "Fabrication of patterned media for high density magnetic storage", *abstract submitted to Electrochem. Soc. Fall Mtg. (2000)*

[A27] F. J. Castaño, Y. Hao, S. Haratani, C.A. Ross, B. Vögeli, M. Walsh and Henry I. Smith, "Magnetic Switching in Continuous and sub-100nm Patterned Pseudo Spin Valves", *abstract submitted to Joint MMM/Intermag Meeting (2001)*

[A28] M. Hwang, M. Redjdal, F. B. Humphrey, and C. A. Ross, "Remanent state studies of conical magnetic particles", *abstract submitted to Joint MMM/Intermag Meeting (2001)*

[A29] Abraham, M., M. Hwang, T.A. Savas, C.A. Ross and R. Ram, "The magnetic properties and interactions of single-domain nanomagnets in a periodic array", *submitted to Appl. Phys. Letts. (2000)*

[A30] C.A. Ross, M. Farhoud, M. Hwang, H.I. Smith, M. Redjdal and F.B. Humphrey, "Micromagnetic behavior of conical ferromagnetic particles", *submitted to J. Appl. Phys. (2000)*

[A31] Bae J., S. Kim, M. Mondol, M. Farhoud, M. Hwang, and K. Y. Toumi, “Experimental study of interactions in the nanostructured Ni pillar arrays”, J. Appl. Phys. 87 p5123-5 (2000).

APPENDIX B

Process Latitude Evaluation

The dose for a single IL exposure, if the power in the two interfering arms is matched, is given by:

$$I = A\sin^2\left(\frac{\pi}{P}x\right) \tag{B.1}$$

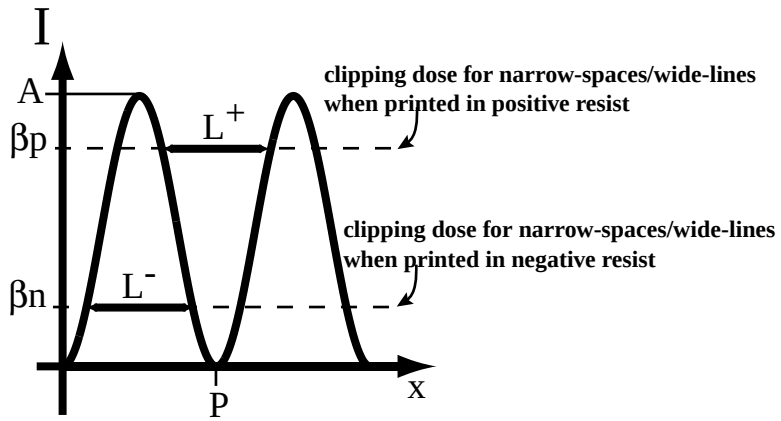

Figure B.1 Plot of equation A.1

We define L as the width of the lines of a grating. If the grating is printed in positive resist, the lines are formed at the dose minima. In this case, the linewidth is denoted by L^+. Conversely, if the grating is printed in negative resist, the lines are formed at the dose maxima. Here, the linewidth is denoted by L^-. The period of the grating is given by P. Assuming we use a resist with infinite contrast (i.e. a sharply defined clearing dose for a positive resist or a sharply defined cross-linking dose for a negative resist), we label the 'clipping dose' for printing lines in resist β_p in the case of a positive resist and β_n in the case of a negative resist.

Since we are interested in controlling grating duty cycle, we define the change in duty cycle corresponding to a change in dose, or

$$\frac{\left(\frac{\Delta L}{P}\right)}{\left(\frac{\Delta A}{A}\right)} \tag{B.2}$$

as the metric for gauging process latitude.

In the case of a negative resist:

$$A\sin^2\left[\frac{\pi}{P}\left(\frac{P}{2}-\frac{L^-}{2}\right)\right]=\beta_n \tag{B.3}$$

$$A\sin^2\left[\frac{\pi}{2}-\frac{\pi}{2}\frac{L^-}{P}\right]=\beta_n \tag{B.4}$$

$$A\cos^2\left(\frac{\pi}{2}\frac{L^-}{P}\right)=\beta_n \tag{B.5}$$

Differentiating this expression, we obtain:

$$dA\cos^2\left(\frac{\pi}{2}\frac{L^-}{P}\right)-\frac{2A\pi}{2P}\cos\left(\frac{\pi}{2}\frac{L^-}{P}\right)\sin\left(\frac{\pi}{2}\frac{L^-}{P}\right)dL^-=0 \tag{B.6}$$

$$dA\cos\left(\frac{\pi}{2}\frac{L^-}{P}\right)=\frac{A\pi}{P}\sin\left(\frac{\pi}{2}\frac{L^-}{P}\right)dL^- \tag{B.7}$$

$$\frac{dA}{A}=\frac{\pi}{P}\tan\left(\frac{\pi}{2}\frac{L^-}{P}\right)dL^- \tag{B.8}$$

Therefore, the change in duty cycle with respect to the change in dose for a negative resist is given by:

$$\frac{dL^-/P}{dA/A}=\frac{1}{\pi}\cot\left(\frac{\pi}{2}\frac{L^-}{P}\right) \tag{B.9}$$

In the case of a positive resist:

$$A\sin^2\left[\frac{\pi}{P}\left(P-\frac{L^+}{2}\right)\right]=\beta_p \tag{B.10}$$

$$A\sin^2\left(\pi-\frac{\pi}{2}\frac{L^+}{P}\right)=\beta_p \tag{B.11}$$

$$A\sin^2\left(\frac{\pi}{2}\frac{L^+}{P}\right)=\beta_p \tag{B.12}$$

Differentiating this expression yields:

$$dA\sin^2\left(\frac{\pi}{2}\frac{L^+}{P}\right)+\frac{2A\pi}{2P}\sin\left(\frac{\pi}{2}\frac{L^+}{P}\right)\cos\left(\frac{\pi}{2}\frac{L^+}{P}\right)dL^+=0 \tag{B.13}$$

$$dA\sin^2\left(\frac{\pi}{2}\frac{L^+}{P}\right)=-\frac{A\pi}{P}\sin\left(\frac{\pi}{2}\frac{L^+}{P}\right)\cos\left(\frac{\pi}{2}\frac{L^+}{P}\right)dL^+ \tag{B.14}$$

$$\frac{dA}{A}\sin\left(\frac{\pi}{2}\frac{L^+}{P}\right)=-\frac{dL^+\pi}{P}\cos\left(\frac{\pi}{2}\frac{L^+}{P}\right) \tag{B.15}$$

Therefore, the change in duty cycle with respect to the change in dose for a positive resist is given by:

$$\frac{dL^+/P}{dA/A}=\frac{1}{\pi}\tan\left(\frac{\pi}{2}\frac{L^+}{P}\right) \tag{B.16}$$

Figure 3.5 in Chapter 3 is a plot of equation A.9 and A.16.

APPENDIX C

Image Reversal of 200 nm-Period Gratings in AZ5214 Photoresist

The purpose of this appendix is to document an unsuccessful attempt at imaging 200 nm-period gratings with interference lithography using an image reversal technique. In this case, we attempt image reversal of AZ5214®, a positive working resist containing a special acid. According to reference [C1] of this appendix, post-exposure-baking this resist will diffuse the photo-generated acid and activate the acid-catalyzed cross-linking reaction. A flood exposure step is also necessary for dissolving the unexposed resist.

Using IL, we attempt to print 200 nm-period gratings in both the negative (Fig. C.2) and the positive tone (Fig. C.3). Finally, we attempt image reversal of large features (> 1μm) using UV contact photolithography (Fig. C.4). We believe the failure of the interference lithography is due to unsuitable resist resolution evidenced by the line-edge roughness of large features (Fig. C.3).

[E1] Spak M., D. Mammato, S. Jaln, and D. Durham, “Mechanism and Lithographic Evaluation of Image Reversal in AZ 5214 Photoresist”, as presented at the Seventh International

Technical Conference on Photopolymers, Ellenville, New York. Sponsored by the Mid-Hudson Section of the Society of Plastics Engineers, Inc. *(note: this reference was supplied to the author by the vendor of the photoresist, Clarion or formerly American Hoest Corporation)*.

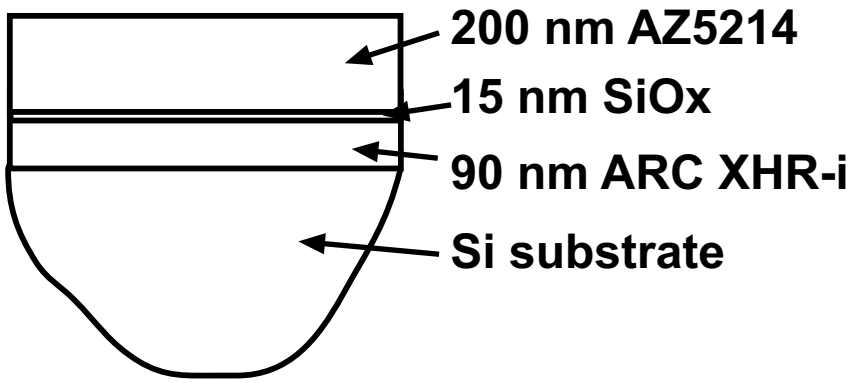

Figure C.1 The lithography stack used for testing the feasibility of printing a 200 nm-period grating in AZ5214 photoresist using interference lithography.

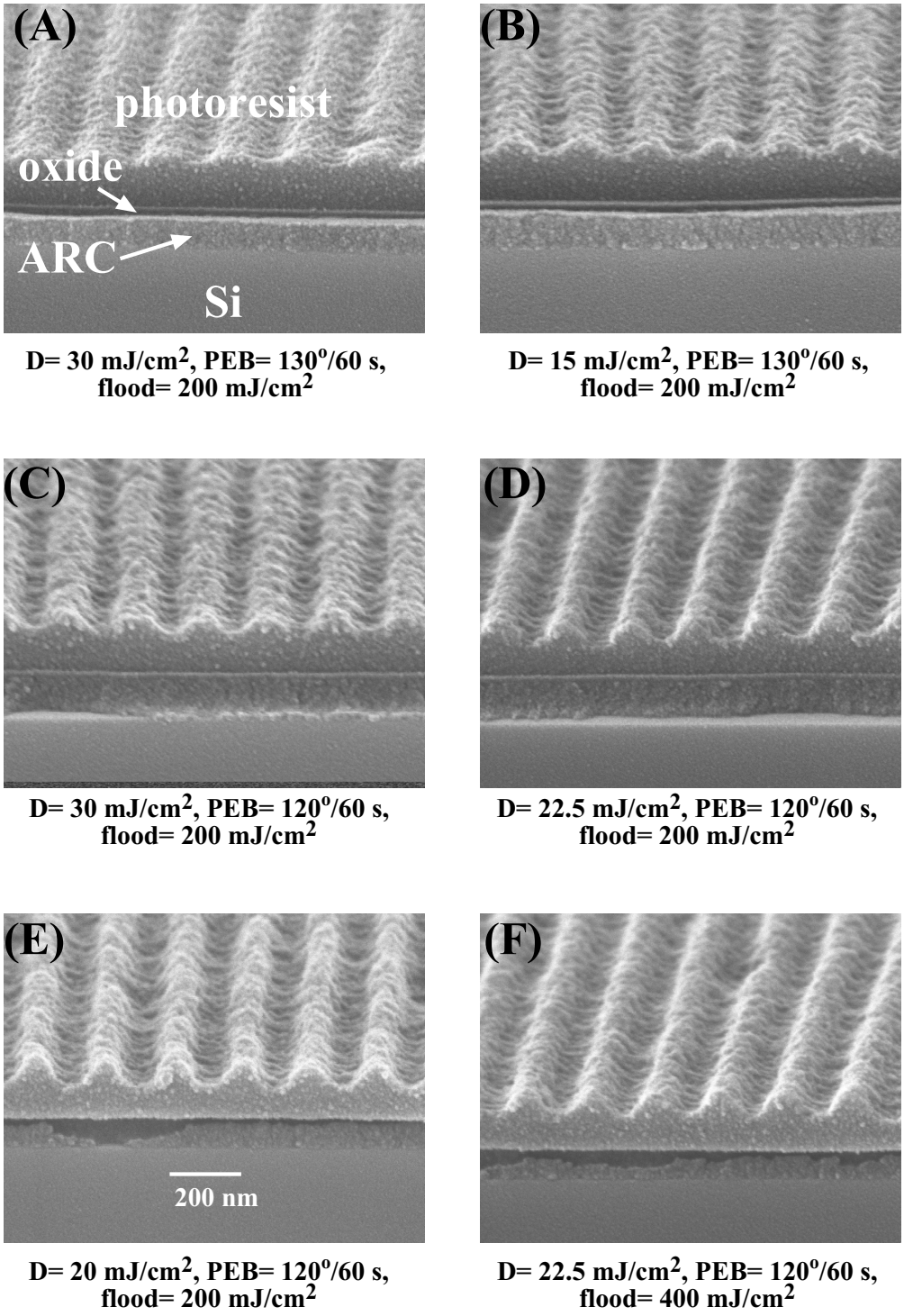

Figure C.2 Scanning electron micrographs of an attempt at printing a 200 nm-period grating in the negative tone using interference lithography and AZ5214 photoresist. The nominal processing conditions were recommended by the manufacturer [C1]. Legend: D=interference-lithography-exposure dose; PEB=post-exposure bake temperature and time, flood=dose of the flood exposure necessary to removed the resist that is not exposed to radiation during the interference lithography step. Subsequent to the flood exposure, the resist is developed in a 0.26 N Tetra-methyl ammonium hydroxide solution for 60 s.

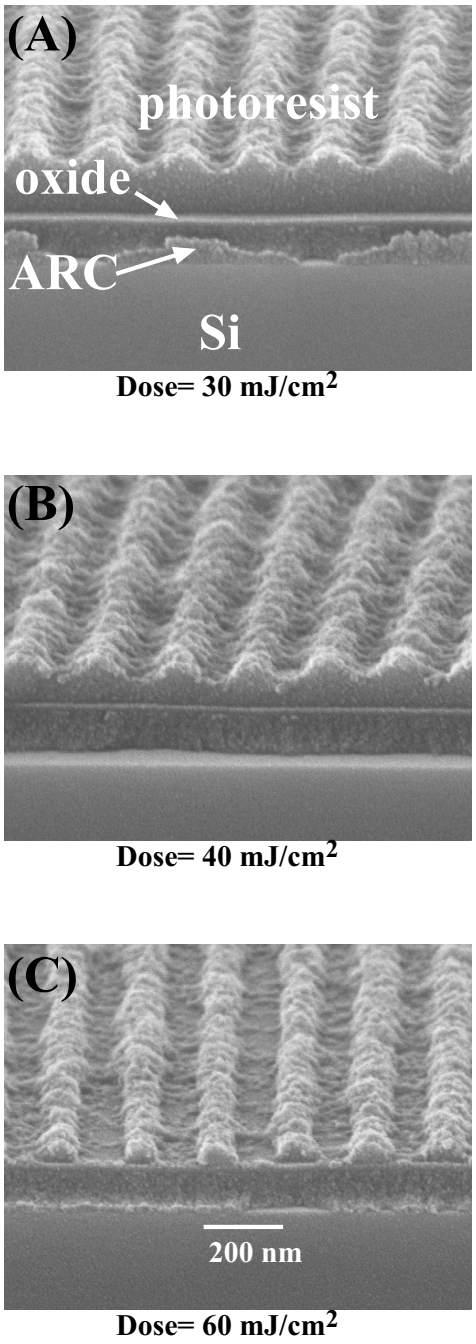

Figure C.3 Scanning electron micrographs of an attempt at printing a 200 nm-period grating in the positive tone using interference lithography and AZ5214 photoresist. The nominal processing conditions were recommended by the manufacturer. Legend: D=interference-lithography-exposure dose. After interference lithography, the resist is developed in a 0.26 N Tetra-methyl ammonium hydroxide solution for 60 s.

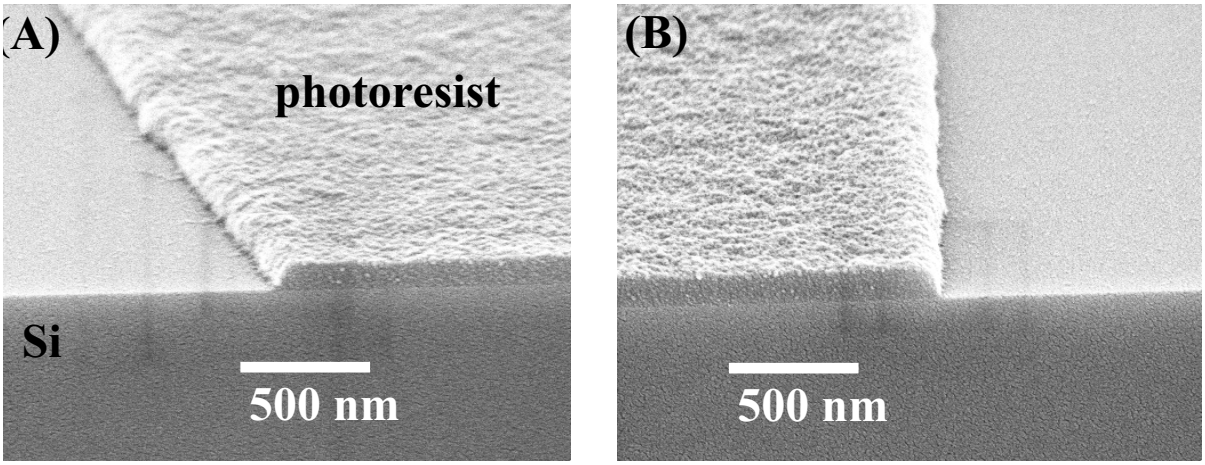

Figure C.4 Scanning electron micrographs of coarse features printed by UV contact photolithography in AZ5214 photoresist. The line-edge roughness is an indication of the low resolution of the photoresist.

APPENDIX D

Imaging Mechanism of Chemically-Amplified, Negative Photoresist

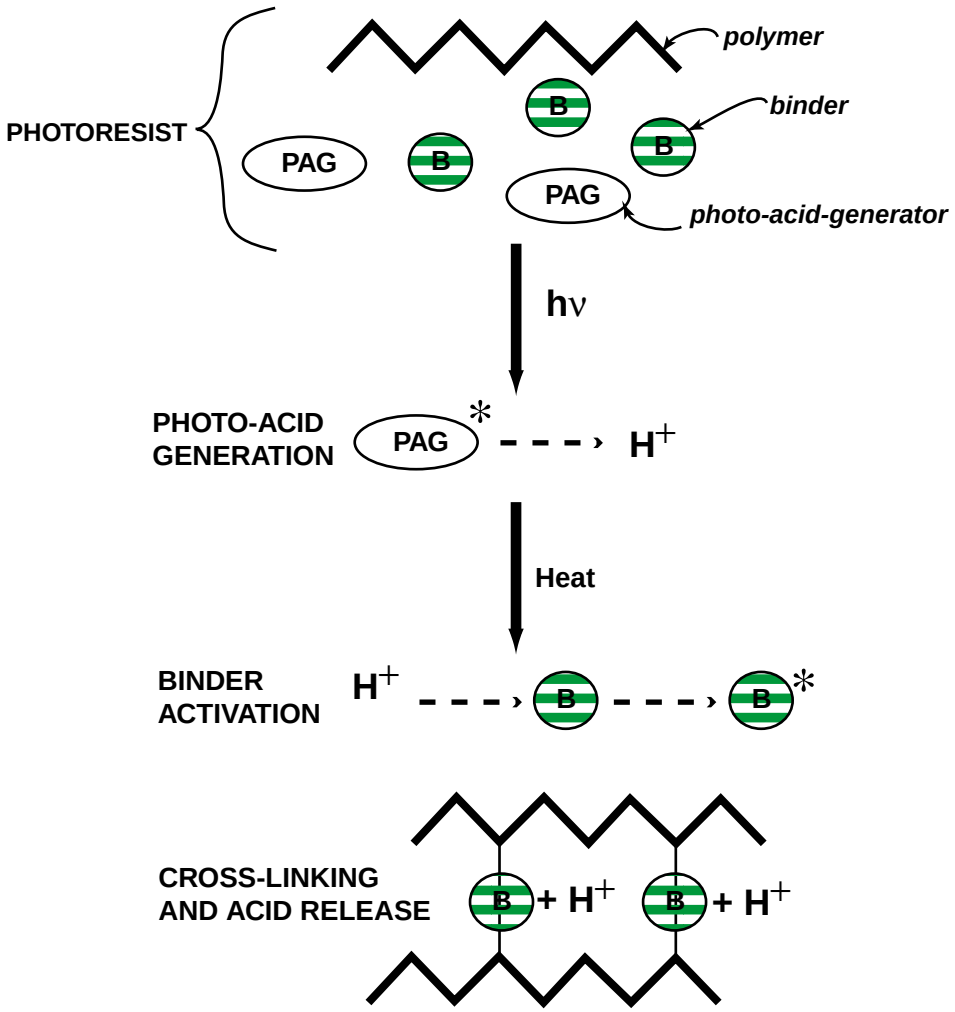

Figure D.1 Illustration of the imaging mechanism in THMR-iN PS1&4, chemically-amplified, negative photoresist from OHKA, a US subsidiary of TOK, Japan. This schematic was provided by the resist manufacturer.

APPENDIX E

Characterizing THMR-iN PS1 Photoresist

This appendix contains a step-by-step listing of the process that was used for characterizing the THMR-iN PS1 negative resist. The results of the experiment are shown in Fig. 3.7a and b in Chapter 3.

Lithography Stack Preparation:

(note: Since this resist is chemically amplified, extra care was taken to avoid subjecting the resist to 'contaminants' which could lead to resist malfunction.)

Following the thermal oxidation of <100>, p-type Si wafers, we:

(1) spin-coat ARC (Brewer XHRi 11) using the track coater in the Integrated Circuits Laboratory (ICL)_ ARC is dispensed with solvent-cleaned pipettes

Spin speed = 4400 rpm (30 s)

Hot plate bake at 175ºC for 60 s

(2) e-beam evaporate interlayer oxide

(an machine error resulted in the deposition of 70 nm of oxide instead of the original target thickness of 40 nm)

(3) ash the interlayer oxide for 8 s

(4) vapor-prime the surface of the interlayer oxide with HMDS, an adhesion promoter.

(5) spin-coat the photoresist (OHKA-THMR iN PS1) using the track coater

Spin speed = 5000 rpm (30 s)

Hot plate bake at 90ºC for 90 s

Lithography:

(1) Exposure:

IL dose from 14 mJ/cm^2 to 30 mJ/cm^2

(2) Post-exposure bake:

at 100ºC for 90 s on a hot plate that is part of an automated track

(3) Development: (using the track's developer spin bowl)

Developer is dispensed for 5 s

Puddle for 25 s

Dispense 5 s

Puddle 30 s

Total develop time is 65 s

Rinse with deionized water for 60 s

Spin dry 30 s

Results:

14 mJ/cm^2 is necessary for a 200 nm-period grating with 50% duty cycle lines and spaces.

Doses greater than 22 mJ/cm^2 will not produce cleared spaces between the lines. This dose is the equivalent of a clearing dose in the positive photoresist.

APPENDIX F

Patterning a Cu/Co-Multilayer

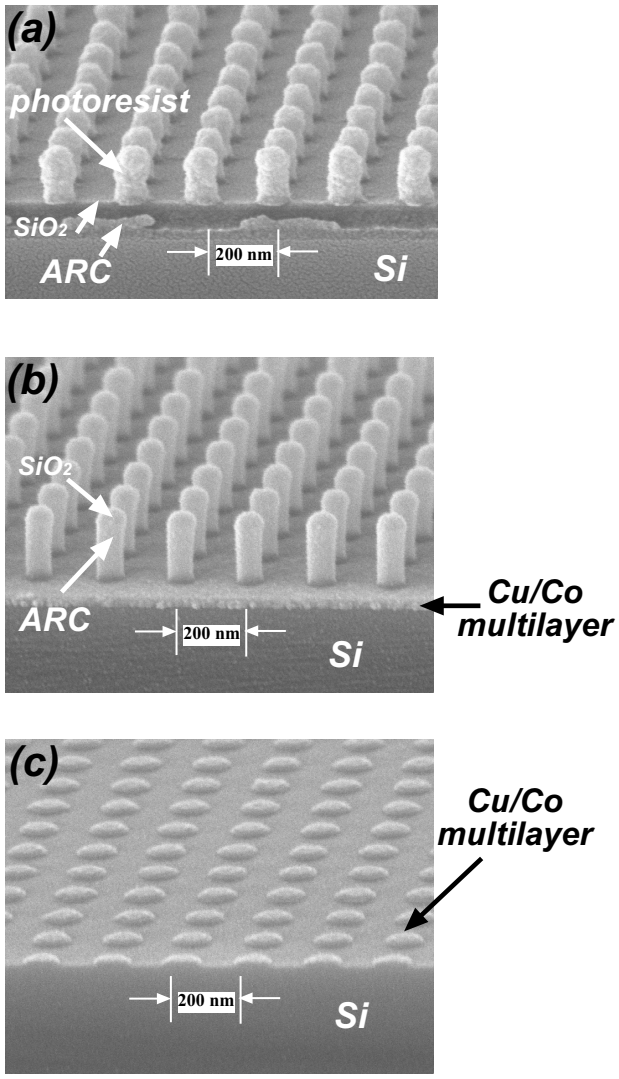

Figure F.1 (a) The first step patterns an array of posts in photoresist using interference lithography. (b) The holes in resist are transferred via reactive-ion-etching into the oxide and ARC layer. (c) Since the multilayer contains Cu which does not form a volatile by-product in a reactive plasma, the unprotected multilayer is removed with ion-beam etching, also known as ion-milling. If the Cu/Co multilayer is not very thick (16 nm in this case), the ARC posts serve as a good etch mask for the multilayer. Note that the multilayer dots in (c) have larger diameter than the etch mask in (d); this is due to the sidewall redeposition during the etch which continuously broadens the diameter of the mask. For a more detailed discussion of this problem as well as improved ion milling techniques, see ref. [7] of the thesis.

APPENDIX G

MFM-Tip Wear

We use the following technique to evaluate the effect of wear on the magnetization of the tip. We AC-demagnetize sample P3 (electroplated Ni posts) such that its total moment is equal to 0. With a strong magnetic tip, we scan the sample a number of times (in different locations) to determine the extent to which the tip's field can magnetize the sample. The assumption is that in any particular region half the particles in the AC-demagnetized sample point up (attractive to the tip) and the other half point down (repulsive to the tip). A strong tip will magnetize some of the dots such that the number of particles pointing up will increase. Figure G.1 shows a number of magnetic images of an AC-demagnetized sample P3. The tip's field is strong enough to magnetize some of the particles such that the total number of attractive (black) nanomagnets is approximately 57%. The percentage of attractive particles is roughly the same after 16, 4 μm x 4 μm scans, which correspond to 8 topography scans (not shown), and 8 magnetic scans in Fig. G.1.

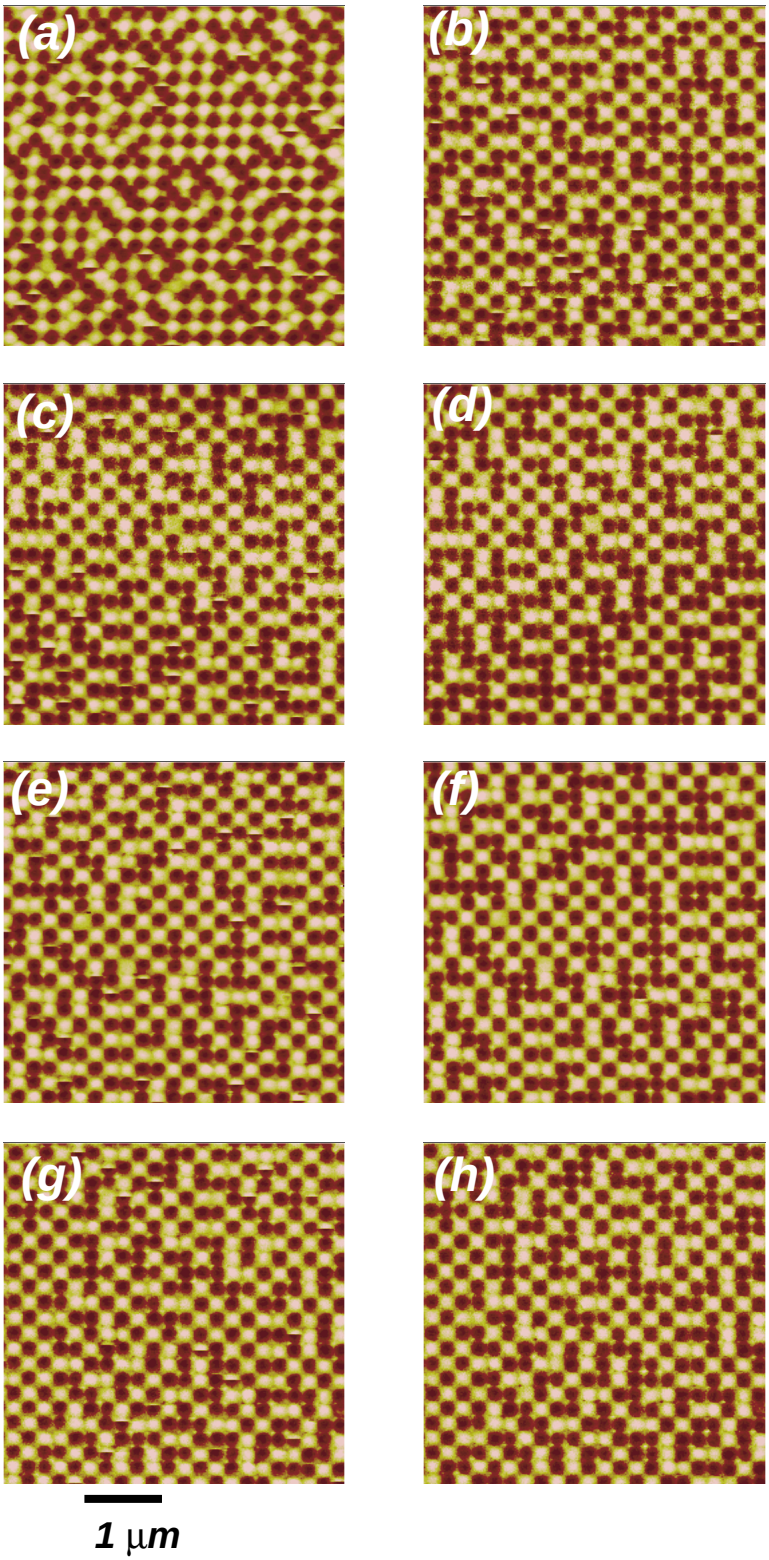

Figure G.1 Magnetic images acquired from electroplated-Ni-sample P3 after AC demagnetization. The number of dark (attractive) particles is roughly constant in all scans indicating that the tip's magnetic strength does not diminish throughout the duration of the experiment.

References

[1] Bruno, L. (2000). The age of petabytes. Red Herring**:** 266-267.

[2] http://www.storage.ibm.com/technolo/grochows/grocho01.htm.

[3] Chou, S. Y. (1997). "Patterned Magnetic Nanostructures and Quantized Magnetic Disks." Proceedings of the IEEE **85**(4): 652-671.

[4] White, R. L., R. M. H. New and R. F. W. Pease (1997). "Patterned Media: A Viable Route to 50 Gbit/in^2 and Up for Magnetic Recording?" IEEE Transactions on Magnetics **33**(1): 990-995.

[5] Cowburn, R. P. (2000). "Property variation with shape in magnetic nanoelements." J. Phys. D: Appl. Phys. **33**: R1-R16.

[6] Meier, G., M. Kleiber, D. Grundler, et. al. (1998). "Vertical polarization of quantum magnets in high density arrays of nickel dots with small height-to-diameter ratio." Applied Physics Letters **72**(17): 2168-70.

[7] Walsh, M. (2000). "Nanostructuring Magnetic Thin Films using Interference Lithography" SM Thesis. Massachusetts Institute of Technology. Cambridge, MA.

[8] Livingston, J. D. (1996). Driving Force: The Natural Magic of Magnets. Cambridge, MA, Harvard University Press.

[9] Charap, S. H. and P. L. Lu (1997). "Thermal Stability of Recorded Information at High Densities." IEEE Transactions on Magnetics **33**(1): 978-983.

[10] Ross, C. A., H. I. Smith, T. Savas, M. Schattenburg, M. Hwang, M. Walsh, M. C. Abraham and R. J. Ram (1999). "Fabrication of patterned media for high density magnetic storage." Journal of Vacuum Science & Technology B **17**(6): 3168-3176.

[11] New, R., R. Pease and R. White (1994). "Submicron patterning of thin cobalt films for magnetic storage." Journal of Vacuum Science & Technology B **12**(6): 3196-201.Sci

[12] Chou, S., M. Wei, P. Krauss and P. Fischer (1994). "Single-domain magnetic pillar array of 35 nm diameter and 65 Gbits/in. density for ultrahigh density quantum magnetic storage." Journal of Applied Physics **76**(10): 6673-5.

[13] Zhu, J. G., X. Lin, L. Guan and W. Messner (2000). "Recording, Noise and Servo Characteristics of Patterned Thin Film Media." IEEE Transactions on Magnetics **36**(1): 23-29.

[14] Cullity, B. D. (1972). Introduction to Magnetic Materials. Reading, MA, Addison-Wesley.

[15] Aharoni A. (1999). “Curling reversal in non-ellipsoidal ferromagnetic particles” Journal of Applied Physics **86**(2): 1041-1046.

[16] Fernandez, A., P. Bedrossian, S. Baker, S. Vernon and D. Kania (1996). “Magnetic force microscopy of single-domain cobalt dots patterned using interference lithography.” IEEE Transactions on Magnetics **32**(5): 4472-4.

[17] Smyth, J. F. and S. Schultz (1988). “Hysteresis of submicron permalloy particulate arrays.” Journal of Applied Physics **63**(8): 4237-4239.

[18] New, R., R. Pease and R. White (1995). “Physical and magnetic properties of submicron lithographically patterned magnetic islands.” Journal of Vacuum Science & Technology B **13**(3): 1089-94.

[19] Envoy, S., D. W. Carr, L. Sekaric, Y. Suzuki, J. M. Parpia and H. G. Craighead (2000). “Thickness dependent binary behavior of elongated single-domain cobalt nanostructures.” Journal of Applied Physics **87**(1): 404-409.

[20] Stoner, E. C., F. R. S. Wohlfarth and E. P. Wohlfarth (1948). “A mechanism of magnetic hysteresis in heterogeneous alloys.” Trans. R. Soc. London Ser. A **240**: 599.

[21] Schabes, M. (1991). “Micromagnetic theory of non-uniform magnetization processes in magnetic recording particles.” Journal of Magnetism & Magnetic Materials **95**(3): 249-88.

[22] Aharoni, A. (1998). “Curling nucleation eigenvalue in a prolate spheroid.” IEEE Transactions on Magnetics **34**(4): 2175-6.

[23] Aharoni, A. (1994). “Elongated superparamagnetic particles.” Journal of Applied Physics **75**(10): 5891-3.

[24] Aharoni A. (1996). “Field-induced magnetization structure in small isotropic spheres” IEEE Transactions on Magnetics **32**(5): 4463-8.

[25] Aharoni, A. (1988). “Elongated single-domain ferromagnetic particles.” Journal of Applied Physics **63**(12): 5879-82.

[26] Gadbois, J. and J. G. Zhu (1995). “Effect of edge roughness in nano-scale magnetic bar switching.” IEEE Transactions on Magnetics **31**(6): 3802-3804.

[27] Zheng, Y. and J. G. Zhu (1997). “Switching field variation in patterned submicron magnetic film elements.” Journal of Applied Physics **81**(8): 5471-5473

[28] Zhu, J. G. and H. N. Bertram (1988). “Micromagnetic studies of thin metallic films.” Journal of Applied Physics **63**(8): 3248-3253.

[29] Fredkin, D., T. Koehler, J. Smyth and S. Schultz (1991). “Magnetization reversal in Permalloy particles: micromagnetic computations.” Journal of Applied Physics **69**(8): 5276-8.

[30] Ross, C. A., M. Farhoud, M. Hwang, H. I. Smith, M. Redjdal and F. B. Humphrey (2000). “Micromagnetic behavior of conical ferromagnetic particles.” *submitted to Journal of Applied Physics.*

[31] Hao, Y., M. Walsh, et al. (2000). “In-plane anisotropy in arrays of magnetic ellipses.” IEEE Trans. Magn.*in press.*

[32] Kleiber, M., F. Kummerlen, M. Lohndorf, A. Wadas, D. Weiss and R. Wiesendanger(1998). “Magnetization switching of submicrometer Co dots induced by a magnetic force microscope tip” Phys. Rev. B. **58**(9): 5563-7.

[33] Proksch, R., S. Foss and E. Dahlberg (1994). “High resolution magnetic force microscopy of domain wall fine structures (invited).” IEEE Transactions on Magnetics **30**(6): 4467-72.

[34] Proksch, R., T. Schaffer, B. Moskowitz, E. Dahlberg, D. Bazylinski and R. Frankel (1995). “Magnetic force microscopy of the submicron magnetic assembly in a magnetotactic bacterium.” Applied Physics Letters **66**(19): 2582-4.

[35] Aharoni, A. (1996). Introduction to the Theory of Ferromagnetism. Oxford University Press.

[36] Bertotti, G. (1998). Hysteresis in Magnetism. Chestnut Hill, MA, Academic Press.

[37] Cowburn, R., D. Koltsov, A. Adeyeye, M. Welland and D. Tricker (1999). “Single-domain circular nanomagnets.” Physical Review Letters **83**(5): 1042-5.

[38] Ross, C., T. Savas, H. Smith, M. Hwang and R. Chantrell (1999). “Modelling of hysteresis loops of arrays of 100 nm period nanomagnets.” IEEE Transactions on Magnetics **35**(5): 3781-3.

[39] O'Handley, R. C. (2000). Modern Magnetic Materials: Principles and Applications. New York, Wiley.

[40] Samwel, E. (1995). Magnetic Characterization of Recording Materials: Design, Instrumentation and Experimental Methods. Twente. PhD Thesis, University of Twente.

[41] Wernsdorfer, W., E. Orozco, K. Hasselbach, A. Benoit, B. Barbara, N. Demoncy, A. Loiseau, H. Pascard and D. Mailly (1997). “Experimental evidence of the Neel-Brown model of magnetization reversal.” Physical Review Letters **78**(9): 1791-4.

[42] Schrefl, T., J. Fidler, K. Kirk and J. Chapman (1999). “Simulation of magnetization reversal in polycrystalline patterned Co elements.” Journal of Applied Physics **85**(8): 6169-71.

[43] Abraham, M., M. Hwang, T.A. Savas, C.A. Ross and R. Ram (2000). “The magnetic properties and interactions of single-domain nanomagnets in a periodic array.” *submitted to Appl. Phys. Letts.*

[44] Redjdal, M. (1998). A numerical investigation of the dynamics of non-periodic micromagnetic structures. PhD Thesis, Boston University, Boston, MA.

[45] Smith, H. I. (1994). Microlithography. Encyclopedia of Applied Physics. G. L. Trigg. Weinheim, Germany and New York, VCH Publishers. **Vol. 10:** 281-295.

Smith, H. I. (1994). Submicron- and Nanometer Structures Technology, Lecture Notes. Nano-Structures Press, Sudbury, MA .

[46] Castano, F. J., Y. Hao, S. Haratani, C. A. Ross, B. Vogeli, M. Walsh and H. I. Smith(2001). “Magnetic Switching in Continuous and sub-100nm Patterned Pseudo Spin Valves.” *abstract submitted to Joint MMM/Intermag Meeting.*

[47] Krauss, P. and S. Chou (1995). “Fabrication of planar quantum magnetic disk structure using electron beam lithography, reactive ion etching, and chemical mechanical polishing.” Journal of Vacuum Science & Technology B **13**(6): 2850-2.

[48] Cui, B., W. Wu, L. Kong, X. Sun and S. Chou (1999). “Perpendicular quantized magnetic disks with 45 Gbits on 4 x 4 cm^2 area.” Journal of Applied Physics **85**(8): 5534-5536.

[49] Chou, S., M. Wei, P. Krauss and P. Fischer (1994). “Single-domain magnetic pillar array of 35 nm diameter and 65 Gbits/in. density for ultrahigh density quantum magnetic storage.” Journal of Applied Physics **76**(10): 6673-5.

[50] New, R., R. Pease and R. White (1996). “Lithographically patterned single-domain cobalt islands for high-density magnetic recording.” Journal of Magnetism & Magnetic Materials **155**: 1-3.

[51] Farhoud, M., M. Hwang, H. Smith, M. Schattenburg, J. Bae, K. Youcef-Toumi and C. Ross (1998). “Fabrication of large area nanostructured magnets by interferometric lithography.” IEEE Transactions on Magnetics **34**(4): 1087-9.

[52] Savas, T., M. Farhoud, M. Hwang, H. Smith and C. Ross (1999). “Properties of large-area nanomagnet arrays with 100 nm period made by interferometric lithography.” Journal of Applied Physics **85**(8): 6160-2.

[53] Farhoud, M., J. Ferrera, A. Lochtefeld, T. Murphy, M. Schattenburg, J. Carter, C. Ross and H. Smith (1999). “Fabrication of 200 nm period nanomagnet arrays using interference lithography and a negative resist.” Journal of Vacuum Science & Technology B **17**(6): 3182-5

[54] Farhoud, M., H. Smith, M. Hwang and C. Ross (2000). “The effect of aspect ratio on the magnetic anisotropy of particle arrays.” Journal of Applied Physics **87**(9): 1-3.

[55] Thielen, M., S. Kirsch, H. Weinforth, A. Carl and E. Wassermann (1998). “Magnetization reversal in nanostructured Co/Pt multilayer dots and films.” IEEE Transactions on Magnetics **34**(4): 1009-11.

[56] Haast, M., J. Schuurhuis, L. Abelmann, J. Lodder and T. Popma (1998). “Reversal mechanism of submicron patterned CoNi/Pt multilayers.” IEEE Transactions on Magnetics **34**(4): 1006-8.

[57] Ferrera, J. (2000). Nanometer-Scale Placement in Electron-Beam Lithography. PhD Thesis, Massachusetts Institute of Technology, Cambridge, MA.

[58] Fernandez, A., J. Decker, S. Herman, D. Phillion, D. Sweeney and M. Perry (1997). “Methods for fabricating arrays of holes using interference lithography.” Journal of Vacuum Science & Technology B **15**(6): 2439-43.

[59] Conley, W., R. Allen and R. Kunz (1997). Deep-UV resist technology: past, present and future. Future Fab International. **1:** 145-149.

[60] Schattenburg, M., R. Aucoin and R. Fleming (1995). “Optically matched trilevel resist process for nanostructure fabrication.” Journal of Vacuum Science & Technology B **13**(6): 3007-11.

[61] Shima M., M. Hwang, M. Farhoud, et al. (2001). “Fabrication of patterned media for high density magnetic storage.” *abstract submitted to Electrochem. Soc. Fall Mtg*.

[62] Farhoud, M. S. (1997). Interferometric lithography and selected applications. SM thesis. Massachusetts Institute of Technology. Cambridge, MA.

[63] MacDermid Incorporated, Barrett sulfamate Ni plating. Waterbury, CT.

[64] Kirtley, J. (1996). Imaging magnetic fields. IEEE Spectrum**:** 40-48.

[65] Hwang, M., M. Farhoud, Y. Hao, M. Walsh, T. A. Savas, H. I. Smith and C. A. Ross (2000) “Major hysteresis loop modelling of two-dimensional arrays of single-domain particles.” IEEE Trans. Magn. *in press*.

[66] Griffiths, D. J. (1989). Introduction to Electrodynamics. Englewood Cliffs, N.J., Prentice Hall.

[67] Haginoya, C., S. Heike, et al. (1999). “Magnetic nanoparticle array with perpendicular crystal magnetic anisotropy.” Journal of Applied Physics **85**(12): 8327-31.

[68] Hug, H., B. Stiefel, P. Van Schendel, A. Moser, R. Hofer, S. Martin, H.-J. Guntherodt, S. Porthun, L. Abelmann, J. Lodder, G. Bochi and R. O'Handley (1998). “Quantitative magnetic force microscopy on perpendicularly magnetized samples.” Journal of Applied Physics **83**(11): 5609-20.

[69] Babcock, K., M. Dugas, S. Manalis and V. Elings (1995). “Magnetic Force Microscopy: recent advances and applications.” Evolution of Thin Film and Surface Structure and Morphology. Symposium. Mater. Res. Soc.

[70] Wiesendanger, R. (1994). Scanning Probe Microscopy and Spectroscopy : methods and applications. Cambridge [England], New York, Cambridge University Press.

[71] Hartmann, U. (1999). Magnetic Force Microscopy. Ann. Rev. Mater. Sci. 1999**:** 53-87.

[72] Zahn, M. (1979). Electromagnetic Field Theory: a problem solving approach. Florida, Krieger Publishing Company.

[73] Rugar, D., H. Mamin, P. Guethner, S. Lambert, J. Stern, I. McFadyen and T. Yogi (1990). “Magnetic force microscopy: general principles and application to longitudinal recording media.” Journal of Applied Physics **68**(3): 1169-83.

[74] Babcock, K., V. Elings, J. Shi, D. Awschalom and M. Dugas (1996). “Field-dependence of microscopic probes in magnetic force microscopy.” Applied Physics Letters **69**(5): 705-7.

[75] Babcock, K., V. Elings, M. Dugas and S. Loper (1994). “Optimization of thin-film tips for magnetic force microscopy.” IEEE Transactions on Magnetics **30**(6): 4503-5.

[76] Kong, L. and S. Chou (1997). “Study of magnetic properties of magnetic force microscopy probes using micronscale current rings.” Journal of Applied Physics **81**(8): 5026-8.

[77] http://www.park.com/spmguide/1-2-0.htm

[78] Matteucci, G., M. Muccini and U. Hartmann (1994). “Flux measurements on ferromagnetic microprobes by electron holography.” Physical Review B **50**(10): 6823-8.

[79] Manalis, S., K. Babcock, J. Massie, V. Elings and M. Dugas (1995). “Submicron studies of recording media using thin-film magnetic scanning probes.” Applied Physics Letters **66**(19): 2585-7.

[80] Proksch, R., G. Skidmore, E. Dahlberg, S. Foss, J. Schmidt, C. Merton, B. Walsh and M. Dugas (1996). “Quantitative magnetic field measurements with the magnetic force microscope.” Applied Physics Letters **69**(17): 2599-601.

[81] Skidmore, G. D. (1998). Imaging Nanofabricated Nickel Particles with the Magnetic Force Microscope, High Resolution Magnetic Force Microscopy Tips, and Magnetic Field Imaging with Magnetic Force Microscope. PhD Thesis. University of Minnesota.

[82] Hwang, M., M. Abraham, T. Savas, H. Smith, R. Ram and C. Ross (2000). “Magnetic force microscopy study of interactions in 100 nm period nanomagnet arrays.” Journal of Applied Physics **87**(9): 1-3.

[83] http://www.dextermag.com/

[84] Ross, C. A., R. Chantrell, M. Hwang, M. Farhoud, T. A. Savas, Y. Hao, H. I. Smith, F. M. Ross, M. Redjdal and F. B. Humphrey (2000). “Incoherent magnetization reversal observed in 30-nm Ni particles.” Phys. Rev. B. *in press*.

[85] Fernandez, A., M. Gibbons, M. Wall and C. Cerjan (1998). “Magnetic domain structure and magnetization reversal in submicron-scale Co dots.” Journal of Magnetism & Magnetic Materials **190**: 1-2.

[86] Mamin, H.J., R. P. Reid, B. D. Terris, D. Rugar (1999). “High-density data storage based on the atomic force microscope.” Proc. of the IEEE **87**(6): 1014-1027.

[87] Smith, H.I. (1996). “A proposal for maskless zone-plate-array nanolithography.” Journal of Vacuum Science & Technology B **14**(6): 4318-4322.

[88] Carter, D.J., D. Gil, R. Menon, M. K. Mondol, H. I. Smith and E. H. Anderson (1999). “Maskless parallel patterning with zone-plate-array lithography” Journal of Vacuum Science & Technology B **17**(6): 3449-3452.

[89] Cowburn, R.P. and M.E. Welland (2000). “Room temperature magnetic quantum cellular automata.” Science **28**(5457): 1466-1468.